Improvements of VLC (Visible Light Communication) Transmissions Under Illumination Constraints : Theoretical Studies and Experiments

Robin Le Priol

THESE DE DOCTORAT DE

L'UNIVERSITE DE SHERBROOKE
L'INSTITUT NATIONAL DES SCIENCES APPLIQUEES RENNES

ECOLE DOCTORALE N° 601
Mathématiques et Sciences et Technologies de l'Information et de la Communication
Spécialité : Télécommunications

Par
Robin LE PRIOL

Improvements of VLC (Visible Light Communication) Transmissions Under Illumination Constraints: Theoretical Studies and Experiments.

Thèse présentée et soutenue à Rennes le 14 juin 2022
Unité de recherche : Institut d'Electronique et des Technologies du numéRique (IETR), INSA Rennes
Département de génie électrique et de génie informatique, Université de Sherbrooke
Thèse N° : 22ISAR 15 / D22 - 15

Rapporteurs avant soutenance :

Mohammad-Ali KHALIGI	Maître de Conférences, HDR, École Centrale de Marseille
Christelle AUPETIT-BERTHELEMOT	Professeur des Universités, HDR, ENSIL-ENSCI

Composition du Jury :

Président :	Didier LE RUYET	Professeur des Universités, HDR, CNAM
Examinateurs :	Christelle AUPETIT-BERTHELEMOT	Professeur des Universités, HDR, ENSIL-ENSCI
	Mohammad-Ali KHALIGHI	Maître de Conférences, HDR, École Centrale de Marseille
	Steve HRANILOVIC	Professeur des Universités, McMaster University
	Éric PLOURDE	Professeur des Universités, Université de Sherbrooke
Dir. de thèse :	Maryline HÉLARD	Professeur des Universités, HDR, INSA Rennes
Co-dir. de thèse :	Sébastien ROY	Professeur des Universités, Université de Sherbrooke
Encadrant de thèse :	Sylvain HAESE	Maître de Conférences, INSA Rennes

RÉSUMÉ EN FRANÇAIS

Introduction

La demande d'accès à Internet à haut débit connaît de nos jours une croissance considérable. D'une part, ceci s'explique par le nombre croissant d'utilisateurs et l'essor des objet communicants, tels que les réseaux de capteurs ou encore plus récemment les voitures autonomes. D'autre part, nous assistons à une intégration à part entière des services en ligne dans nos vies quotidiennes, tels que des applications multimédias, des services financiers ou du magasinage en ligne pour n'en citer que quelques-uns. Pour l'instant, la réponse à ce besoin croissant de haut débit et de fiabilité de communication est apportée par des technologies de transmissions radiofréquences (RF) telles que la quatrième génération de réseaux cellulaires (4G), la technologie Wi-Fi pour les réseaux locaux, ou encore par la cinquième génération de réseaux cellulaires (5G), cette dernière étant depuis peu (2020) en cours de déploiement. La congestion et les coûts élevés du spectre radioélectrique ont néanmoins poussé les groupes de recherche à exploiter des fréquences toujours plus élevées pour les futures technologies de transmission sans fils. Ainsi, alors que le réseau 5G opère dans les bandes millimétriques, il est envisagé d'utiliser des fréquences de l'ordre du THz pour la sixième génération de réseaux cellulaires (6G).

Une autre piste de recherche prometteuse pour répondre aux besoins susmentionnés est l'utilisation de la partie visible du spectre électromagnétique. La technologie de transmission sans fils dans le spectre visible est dénommée "Visible Light Communication" (VLC), et offre de nombreux avantages par rapport aux technologies RF pour les environnements intérieurs. Ses atouts incluent une large bande non-régulée d'environ 375 THz, une robustesse face aux interférences électromagnétiques, une protection contre l'écoute illicite (la lumière ne traverse pas les murs d'une pièce) et un faible coût d'installation. En effet, concernant ce dernier point, les diodes électroluminescentes (LEDs) à bas coûts disponibles dans le commerce peuvent tout à fait servir pour à la fois éclairer et transmettre de l'information sans fils. Par ailleurs, nous assistons parallèlement à une évolution significative du marché de l'éclairage. En effet, les LEDs remplacent peu à peu les ampoules incandescentes en raison de leur bien meilleure efficacité énergétique. Selon, l'agence internationale de l'énergie, la part de vente des LEDs sur le marché de l'éclairage est passée de 4 % à 46 % entre 2013 et 2019, et est même amenée à atteindre 87 % d'ici 2030.

Parmi les types de LEDs existants, les LEDs blanches sont typiquement les plus utilisées du fait de leur faible coût. Ces LEDs, en revanche, présentent une bande de modulation limitée à quelques MHz, ce qui ralentit fortement la vitesse de transmission possible des signaux. De plus, les LEDs possèdent des propriétés non-linéaires pouvant fortement altérer la qualité du signal à transmettre.

De nombreuses expériences de laboratoire ont déjà démontré la faisabilité de transmission à des débits élevés, mais généralement sans prendre en compte l'efficacité de l'éclairage. En effet, cette fonction pourtant essentielle à l'implémentation des VLC dans les environ-

nements intérieurs est souvent perdue de vue au profit de la recherche de débits toujours plus élevés.

L'objectif global de cette thèse est d'optimiser le débit de transmission en VLC à travers des études numériques et des expérimentations en prenant en considération la qualité de l'éclairage à l'intérieur des bâtiments. A cet effet, des études portant sur les techniques de modulations à hautes efficacités spectrales sont menées, notamment sur la modulation d'impulsion d'amplitude (PAM), la modulation d'amplitude et de phase sans porteuse (CAP) et les techniques à entrées multiples sorties multiples (MIMO). Des méthodes de compensation des non-linéarités de la LED sont également explorées. Finalement, une approche plus théorique est amorcée dans le dernier chapitre de la thèse pour présenter une technique de décomposition polynomiale de matrice appliquées aux grands environnements intérieurs dans un contexte MIMO large bande.

Chapitre 2 : Fondamentaux des VLC

Dans ce chapitre, nous présentons les principes fondamentaux des VLC. D'abord, nous introduisons le concept de modulation d'intensité de détection direct (IM/DD) sur lequel est basé la majorité des systèmes utilisant des sources lumineuses incohérentes telles que des LEDs. Cette technique repose sur le fait que l'information est transmise en modulant le courant dans la LED, qui génère à son tour un flux lumineux dont les fluctuations sont imperceptibles par l'oeil humain. Au récepteur, une photodiode détecte ces fluctuations lumineuses et génèrent un courant électrique proportionel appelé photocourant. Un amplificateur transimpédance permet ensuite de convertir ce photocourant en tension mesurable.

Dans un second temps, les types de LEDs et les types de photodiodes existants sont présentés. En raison de leur caractéristiques favorables à la fonction d'éclairage, qui sont un flux lumineux élevé et un bas coût, les LEDs blanches sont sélectionnées dans cette thèse. Ces LEDs sont constituées d'une LED de couleur bleue recouverte d'une couche de phopshore qui émet des photons jaune lorsqu'elle est excitée par de la lumière bleue. Les photons émis par la source bleue se recombinent avec les photons jaunes pour générer de la lumière blanche. Le phopshore agit comme un filtre passe-bas et limite la bande de modulations (ou bande à 3-dB) à quelques MHz.

Nous introduisons ensuite le le concept de non-linéarité de la LED. En effet la caractéristiques de transfert reliant la puissance lumineuse de sortie et le courant d'entrée n'est pas linéaire. Ceci implique que les fluctuations lumineuses ne sont pas identiques à celle du courant d'entrée provoquant ainsi une dégradation du signal dans la chaîne d transmission.

Nous présentons par la suite les métriques d'éclairage à l'intérieur des bâtiments telle que l'éclairement lumineux horizontal exprimé en lux [lx], qui est une métrique utilisée dans les normes internationales d'éclairage pour déterminer le niveau d'éclairage au niveau du récepteur.

les caractéristiques du canal optique sans fil sont également présentées ainsi les techniques de modulations principales monoporteuses et multiporteuses. Parmi les techniques de modulations monoporteuses, il est préférable d'utiliser des modulations à haute efficacité spectrale telles que la PAM ou la CAP pour palier la faible de bande de modulation des

LEDs blanches. D'autre méthodes alternatives sont présentées, notamment les techniques MIMO, parmi lesquelles la modulation spatiale (SM) et la multiplexage spatiale (SMP) qui permettent d'augmenter l'efficacité spectrale en augmentant le nombre de LEDs à l'émission et le nombre de photodiodes en réception.

Enfin, les récents résultats expérimentaux de la littérature sont également présentés. Il est conclu que la plupart des études se focalisent sur l'utilisation de la DMT et sans toujours prendre en compte un niveau d'éclairage standardisé.

Chapitre 3 : Étude d'un lien VLC sous contrainte d'éclairage avec la modulation CAP

Ce chapitre présente des mesures sur un dispositif expérimental VLC réalisé à partir de composants à bas-coût avec la modulation CAP. Dans un premier temps, la modulation CAP est détaillée. De plus, le design du dispositif expérimental est présenté en considérant la contrainte d'éclairage garantissant un niveau d'éclairage de 500 lux préconisé pour des tâches couramment réalisées dans un bureau de travail (lecture et écriture). Les étapes de transmissions incluant les traitement hors ligne à l'émission et en réception ainsi que les mesures sur le banc de test sont détaillées.

L'optimisation du débit est réalisée comme suit : la bande de modulation du signal directement reliée au débit binaire du système est progressivement augmentée jusqu'à atteindre un taux d'erreur binaire (BER) égal à 10^{-3}. En réception, un égaliseur linéaire fractionné (FSE) permet d'éliminer l'interférence entre symboles provenant de la réponse de la LED car la bande de modulation du signal est bien supérieure à la bande de modulation de la LED sélectionnée égale à 1.47 MHz. Ainsi, des débits binaires de 142.4 Mbps et 184 Mbps sont démontrés avec la modulation d'ordre 16 (16-CAP) et 4 (4-CAP), et correspondant à des bandes de modulation de 85.44 MHz et 55.2 MHz, respectivement

Sur les constellations après égalisation, des distorsions peuvent être observées sur les bords. Ces distorsions sont typiquement l'expression de l'impact des non-linéarités de la LED.

Chapitre 4 : Modélisation de la non-linéarité de la LED et compensation

Dans ce chapitre, un modèle de simulation est développé permettant d'évaluer les performances de techniques de modulation avec le montage expérimental présenté dans le chapitre 2. Dans la première partie de ce chapitre, il n'est pas question des non-linéarités mais de l'évaluation de la distance entre simulation et pratique en termes de rapport signal sur bruit (SNR). Nous proposons pour modéliser le canal de transmission un modèle analytique correspondant à la réponse de la LED. Des mesures expérimentales montrent que la réponse en fréquence du modèle proposé est très similaire à celle mesurée sur la banc de test. Il est conclu que le SNR en réception déterminé avec le modèle de simulation est légèrement plus élevé (de 1 à 2 dB) ce qui implique que les performances en simulation seront légèrement supérieures à celles mesurées en pratique.

Dans une seconde partie, l'impact des non-linéarités de la LED sont étudiées. Pour des signaux large bande, l'effet mémoire des non-linéarités de la LED doit être pris en compte. Nous étudions donc deux modèles prenant en considération cet effet mémoire, à savoir le modèle de Hammerstein et le modèle des séries de Volterra. Tandis que le premier bénéfice d'une plus grande simplicité d'implémentation, le second (modèle de Volterra) permet de

mieux modéliser l'impact des non-linéarités de la LED visible sur les constellations après égalisation. Une technique de compensation adaptative des non-linéarités en réception basée sur les séries de Volterra est évaluée en simulation. Nous montrons ainsi l'efficacité cette méthode pour corriger ces effets non-linéaires et améliorer les performances du système.

Chapitre 5 : Comparaison des modulations PAM et CAP

Dans ce chapitre, les techniques de modulations PAM et CAP sont comparées en simulation en utilisant le modèle développé au chapitre 4 et expérimentalement en utilisant le banc de test associé. Pour les deux modulations, le débit est d'abord optimisé en simulation pour un éclairage standardisé de 500 lux sans prendre en compte les effets non-linéaires de la LED. De plus, le facteur de roll-off des filtres de mise en forme pour la PAM et la CAP sont optimisés. Il est montré que la modulation PAM présente de meilleures par rapport à la CAP. De plus, le roll-off optimal pour la PAM est 0.4 tandis qu'il est de 0.15 pour la CAP.

Il est également observé en simulation que pour un niveau d'éclairage conventionnel de 500 lux, le SNR est suffisamment élevé pour pouvoir employer des grands ordres de modulations comme la 8-PAM ou la 64-CAP. Des mesures expérimentales pour ces deux modulations susmentionnées sont réalisées à un débit de 210 Mbps. Il est observé que les performances de la 8-PAM sont fortement dégradées par rapport à celles de la 64-CAP lorsque les non-linéarités ne sont pas corrigées. En pratique, la présence d'effets non-linéaires dégradent fortement la qualité du signal. La postdistorsion adaptative basée sur la série de Volterra est donc appliquée afin de linéariser le système. En revanche, lorsque les non-linéarités sont correctement compensées, les performances de la 8-PAM sont meilleures que celle de la 64-CAP, ce qui coïncide avec les résultats de simulation.

Finalement, un point de comparaison est réalisé avec la modulation DMT. Lors d'une précédente étude menée par notre groupe de recherche, la modulation DMT avait été optimisée pour le même système et dans des conditions expérimentales identiques, et un débit maximal de 100 Mbps a été atteint. Nous déterminons ainsi que lorsque notre algorithme de postdistorsion est appliqué à la DMT, le débit atteint maximal est de 145 Mbps, ce qui est inférieur aux débits que nous avons montré que la PAM et la CAP.

Chapitre 6 : Techniques MIMO avec imageur

Dans les chapitres précédents, une configuration à une seule entrée une seul sortie (SISO) est employée. Une autre solution pour augmenter l'efficacité spectrale est l'utilisation des techniques MIMO telles que la modulation spatiale (SM) ou le multiplexage spatial (SMP). Les performances de ces techniques sont étudiées théoriquement et en simulation avec et sans récepteur imageant. De plus, la mobilité de l'utilisateur est étudiée en explorant l'impact du déplacement d'un récepteur imageant.

Tout d'abord, nous montrons l'intérêt du récepteur imageur. Ce dernier est un système optique qui consiste en une lentille permettant de séparer les faisceaux lumineux provenant des différentes LEDs émettrices et de les focaliser à des endroits distincts sur le plan d'un récepteur où se trouvent les photodiodes. De cette manière, l'interférence entre canal est éliminée et la matrice de canal MIMO est typiquement représentée par une matrice diagonale. En simulation nous observons un gain de SNR de $\sim$ 36 dB and $\sim$ 16 dB pour SMP and SM, respectivement, comparé au cas non-imageant.

De plus, un système expérimental MIMO 2×2 avec une distance réaliste de 2.25 m est présenté. Les gains DC sont mesurés pour différentes valeurs de désaxage par rapport aux LEDs à l'émission. En outre, un décalage des spots lumineux sur le plan du récepteur est observé lié à un changement de l'angle d'incidence des faisceaux lumineux sur la lentille imageante. Les photodiodes sont alors manuellement replacées à chaque mesure pour détecter le pic d'intensité lumineuse. En utilisant ces gains mesurés en pratique, les performances de SMP et SM combinées à la modulation PAM sont étudiées en simulation pour deux efficacités spectrales, à savoir 4 bit/s/Hz et 6 bit/s/Hz. il est alors conclu que SMP offre de meilleurs performances par rapport à SM pour les deux efficacités spectrales.

Dans la dernière partie de ce chapitre, une forme de bit loading est proposée pour adapter l'ordre de modulation en fonction de l'état du canal, permettant ainsi de maintenir la qualité du lien de communication malgré le déplacement du récepteur imageant. A même efficacité spectrale, les performances de SMP avec bit loading sont nettement supérieures à celles sans bit-loading.

Chapitre 7 : Décomposition polynomiale de matrice LU

Dans ce chapitre, nous mettons en oeuvre une méthode de décomposition LU (lower-upper) de matrice polynomiale dénomée "LU-PMD" pour les grands espaces intérieurs comme les halls d'aéroport, les centres de congrès ou les usines par exemple. La technique LU-PMD annule complètement l'interférence entre canal sans utilisation d'imageur, et réduit le canal MIMO en canaux de bruit additif SISO indépendants. De ce fait, l'interférence entre symboles issue des arrivées successives de signaux émis par différents émetteurs dans les grands espaces est atténué.

Le principe de la décomposition est d'abord décrit de manière générale et un exemple d'application pour un système MIMO 4×4 est présenté. Ensuite, la technique SMP est évaluée conjointement avec pré- et post-codage en utilisant respectivement les matrices de pré-filtrage et de post-filtrage obtenues après application de la méthode LU-PMD. Une transmission de 200 Mbaud avec un signal 2-PAM est simulée et il est démontré que trois sous-canaux à bruit additif peuvent être utilisés efficacement pour la transmission, produisant un débit binaire de 600 Mbps, tandis que le dernier sous-canal est inutilisable. L'inconvénient majeur de la technique LU-PMD réside dans le fait que les matrices de pré- et post-filtre ne sont pas para-unitaires. Par conséquence, après pré-codage le signal d'information est amplifié et la plage dynamique actuelle de chaque source lumineuse n'est pas pleinement exploitée. De plus, le bruit après post-codage est amplifié, dégradant ainsi les performances du système.

Chapitre 8 : Conclusion

Dans cette thèse nous avons étudié des techniques de modulation avec pour objectif principal l'optimisation des débits sous des contraintes d'éclairage. Les résultats de simulation et les mesures expérimentales démontrent l'intérêt des modulations monoporteuses combinées avec un égaliseur par rapport aux modulations de type multiporteuses telle que la DMT, cette dernière étant souvent considérée comme la modulation "par défaut".

Le problème concernant la non-linéarité de la LED a été adressé en proposant une technique de postdistortion adaptative efficace pour corriger les effets linéaires. Par conséquent, les débits sont significativement améliorés. De plus nous avons montré que des débits de

$\sim$ 210 Mbps sont possibles avec la PAM et la CAP en employant des grands ordres de modulations.

Les techniques MIMO, à savoir le multiplexage spatiale et la modulation spatiale, ont été étudiées en utilisant un imageur dans une configuration 2×2 et nous avons montré qu'un récepteur intelligent permettrait à l'utilisateur de se déplacer de manière flexible sous le luminaire VLC tout en conservant une fiabilité de communication.

Finalement, la technique de décomposition polynomiale LU-PMD est appliquée pour la première fois aux canaux MIMO VLC dans des grands environnements intérieurs. Un simple pré-codage et post-codage sont alors requis pour supprimer de manière effective l'interférence entre canal (ICI), ainsi que l'interférence entre symboles (ISI).

Mots-clés : communication en lumière visible, éclairage intérieur, modulation d'amplitude et de phase sans porteuse, non-linéarité de la LED, diode électroluminescente, MIMO, multiplexage spatial, modulation spatiale, décomposition de matrice polynomiale

ACKNOWLEDGEMENTS

This thesis could not have been completed without the support of many individuals. Although it is not possible to acknowledge everyone who helped me in one way or another throughout my PhD years, I would like to mention the following.

First and foremost, I wish to express my most profound gratitude to my supervisors, Prof. Sébastien Roy, Prof. Maryline Hélard and Dr. Sylvain Haese, for their valuable guidance, constant support, and confidence in my abilities throughout my whole doctoral studies. I fully understand the privilege I benefited from to have been able to work with them. They steered me in the right direction, while providing me freedom to explore other avenues. Thanks to their ongoing involvement, I was given the chance to undertake my PhD at two institutions, the University of Sherbrooke in Canada and INSA Rennes in France. This international collaboration has profoundly and positively impacted the research work presented in this thesis. Also, conducting research in a foreign university has been a unique experience in my life both academically and socially.

I owe a debt of gratitude to Dr. Ahmad Jabban, who I met at the early stage of my PhD studies, and who spent considerable time helping me shape my research work. His insightful comments were crucial for the formulation of the thesis. I have thoroughly enjoyed our work together and all the inspiring discussions we had, so thank you.

To Éric Bazin, thank you for your patience and your all-around knowledge. You taught me a great deal from a practical point of view and helped me perform measurements on the experimental platform in excellent conditions.

I offer special thanks to Dr. Moustapha Mbaye of Cheikh Anta Diop University, for the enlightening discussion on the LU-PMD technique and his input on the implementation.

I would like to thank my internal and external examiners at different stages of the PhD program: Dr. Mohammad-Ali Khalighi, Prof. Yves Louet, Dr. Pierre-Jean Bouvet, Prof. Réjean Fontaine, Prof. Steve Hranilovic, Prof. Didier Le Ruyet, Prof. Éric Plourde, and Prof. Christelle Aupetit-Berthelemot, for their constructive criticism and enthusiasm.

Further thanks to all the PhD and postdoctoral students I've met along the way in Rennes and in Sherbrooke. This work would have been much less enjoyable without them. Special thanks to Romain, for making my Canadian experience so pleasant.

To Pol, Francesco, and Daniel, thank you for being just who you are, and thank you for distracting me from work when I needed it the most.

I thank my family for their love and belief in me. Words cannot express how grateful I am to my parents, for providing me with unconditional support in this great endeavor, and for giving me the means to become the person I am today.

Finally, I would like to acknowledge all financial support received from INSA Rennes and the University of Sherbrooke, including a full university PhD scholarship and multiple grants for conference attendance, international mobility, and journal charges.

TABLE OF CONTENTS

LIST OF FIGURES

LIST OF TABLES

NOTATIONS

Nomenclature	**Definition**
a	Scalar.
$a(z)$	Polynomial.
$\mathbf{a}$	Scalar vector.
$\mathbf{A}$	Scalar matrix.
$\mathbf{A}(z)$	Polynomial matrix.

Operator	**Definition**
$*$	Convolution product.
$\|.\|$	Absolute value.
$\|\|.\|\|_{\mathrm{F}}$	Frobenius norm.
$[.]^T$	Transpose operator.
$d_{\mathrm{H}}(.,.)$	Hamming distance.
$\mathbb{E}[.]$	Expectation operator.
$\deg(.)$	Degree of a polynomial.
$\exp(.)$	Exponential function.
$\log_2(.)$	Binary logarithm function.
$\ln(.)$	Natural logarithm function .
$\min(.,.)$	Minimum operator.
$P_{opt}(.)$	LED non-linear transfer function.
$P_r(.)$	Probability operator.
$Q(.)$	Q-function.
$\mathrm{Re}(.)$	Real part operator.

Symbol	**Definition**
a_k	Discrete real part of the QAM transmitted symbol.
$\mathbf{a}$	Vector of Volterra kernel coefficients ($(M_1 + M_2^2) \times 1$).
A	PD active surface in square meter [m^2].
α	Roll-off factor.
α_M	Magnification factor.
β	System transfer DC gain.
B	Occupied bandwidth in Hertz [Hz].
B_{CAP}	Total occupied bandwidth by the CAP signal in Hertz [Hz].
B_{eq}	Noise-equivalent bandwidth in Hertz [Hz].
B_{PAM}	Total occupied bandwidth by the PAM signal in Hertz [Hz].
b_k	Discrete imaginary part of the QAM transmitted symbol.
c	Speed of light in meter per second [$\mathrm{m.s}^{-1}$].
c_k	Discrete complex QAM modulated symbol.

$\hat{c}_k$	Discrete complex QAM equalized symbol.
$\hat{\mathbf{c}}$	Vector of equalized symbols ($M_d \times 1$).
$\delta(t)$	Dirac delta function.
ΔB	Subcarrier bandwidth in Hertz [Hz].
Δd	Lateral offset in meter [m].
ΔI	LED current swing range in ampere [A].
d	Distance between the emitter and the receiver in meter [m].
$\mathbf{D}$	Diagonal matrix ($N_r \times N_t$).
D_b	Bit rate in bit per second [bit.s^{-1}].
d_k	Discrete PAM transmitted symbol.
d_r	Distance between the receive PDs in meter [m].
D_s	Symbol rate in baud.
d_t	Distance between the transmit LEDs in meter [m].
d_{ϵ_n}	Surface of element ϵ_n in square meter [m^2].
η_{CAP}	Spectral efficiency of CAP in bit per second per Hertz [bit.s^{-1}.Hz^{-1}].
η	Spectral efficiency in bit per second per Hertz [bit.s^{-1}.Hz^{-1}].
η_{PAM}	Spectral efficiency of PAM in bit per second per Hertz [bit.s^{-1}.Hz^{-1}].
$e(n)$	Adaptive algorithm error at the n-th iteration.
E_h	Horizontal illuminance in lux [lx].
E_h^{tot}	Total horizontal illuminance in lux [lx].
ϵ_n	Reflecting element n.
ϵ_n^t	Reflecting element n acting as a transmitter.
ϵ_n^r	Reflecting element n acting as a receiver.
f_0	LED 3-dB modulation bandwidth in Hertz [Hz].
f_{awg}	Sampling rate of the AWG in Hertz [Hz].
f_b	3-dB cut-off frequency of the blue light response in Hertz [Hz].
f_c	Center frequency of the CAP signal spectrum in Hertz [Hz].
f_l	Focal length in meter [m].
f_p	3-dB cut-off frequency of the phosphor layer response in Hertz [Hz].
$\mathbf{g}$	Vector of Kalman gain coefficients ($(M_1 + M_2^2) \times 1$).
G_b	Power gain of the blue light component.
G_p	Power gain of the yellow light component.
$g_{SRRC}(t)$	SRRC filter.
$\mathbf{H}$	Channel matrix ($N_r \times N_t$).
$\mathbf{H}_{\text{ImR}}$	Channel matrix in the imaging case ($N_r \times N_t$).
$\mathbf{H}_{\text{NImR}}$	Channel matrix in the non-imaging case ($N_r \times N_t$).
$h(t)$	Channel impulse response.
$h_b(t)$	Blue chip impulse response.
$h_{direct}(t)$	Direct propagation path impulse response.
$h_{diff}(t)$	Diffuse link impulse response.
$h_i(t)$	In-phase CAP transmit filter.
$h_k(m_1, \ldots, m_k)$	Kernel of Volterra series at order k and at time delay m_k.
$h_{LED}(t)$	LED time domain response.
$h_{n_r n_t}$	Transfer factor from a transmitter n_t to a receiver n_r.
$h_{n_r n_t}^l$	Impulse response sampled at the l-th delay between a transmitter n_t and

	a receiver n_r.
$h_p(t)$	Phosphor layer impulse response.
$h_q(t)$	Quadrature CAP transmit filter
$h_{VLC}(t)$	Impulse response of free space propagation.
$H_{LED}(f)$	LED frequency domain response.
I	LED input current in miliAmpere [mA].
I_{DC}	LED DC bias current in ampere [A].
$\mathbf{I}_p$	Identity matrix ($p \times p$).
K	Upsampling factor.
K'	Number of samples per symbol in a FSE.
k_r	Number of reflections of the light ray.
K_m	Maximum luminous efficacy in lumen per Watts [lm.W^{-1}].
λ	Wavelength in meter [m].
λ_e	Expected number of photons per interval.
λ_f	Forgetting factor.
L	Total number of samples in the channel impulse response.
μ	Step size parameter.
μ_{max}	Maximum step size value.
m	Lambertian emission order of the LED.
M	Signal constellation order.
m_{CAP}	Number of bits encoded in one CAP symbol.
M_d	Number of taps in the feedback filter.
M_f	Number of taps in the feedforward filter.
M_I	Modulation index of the LED.
M_j	Modulation index of the j-th transmit LD.
M_k	Memory length at order k of Volterra series.
m_k	Time delay at order k of Volterra series.
m_{PAM}	Number of bits encoded in one PAM symbol.
M_{samp}	Total number of samples in the least squares cost function.
$\mathbf{n}$	Vector of additive noise across the array of photodiodes ($N_r \times 1$).
$n(t)$	Instantaneous additive white Gaussian noise.
N	Number of subcarriers in the DMT system.
N_0	Unilateral power spectral density in Watt per Hertz [W.Hz^{-1}].
N_{LED}	Total number of LED chips in a luminaire.
N_a	Number of active LEDs during a symbol period.
N_{photon}	Number of counted photons.
N_t	Number of transmit LEDs.
N_r	Number of receive PDs.
N_s	Maximum number of resulting subchannels.
N_{symb}	Window size in NMSE calculation.
Ω	Number of reflecting elements on the room surface.
$\mathbf{P}$	Inverse correlation matrix ($M_1 + M_2^2 \times M_1 + M_2^2$).
$P(\lambda)$	Spectral power density function.
$p(n)$	Discrete-time output of Volterra series model.
P_{max}	Maximum optical power.

P_{noise}	Noise power in Watt [W].
P_r	Received mean optical power in Watt [W].
P_{signal}	Received signal electrical power in Watt [W].
$P_{opt,p}^{\mathrm{SM}}$	SM optical intensity.
$P_{opt,p}^{\mathrm{SMP}}$	SMP optical intensity.
P_{rms}	Received signal root mean square voltage in Volt [V].
P_t	Emitted mean optical power in Watt [W].
ϕ	Angle of emergence as defined in Fig. 2.4 in degree.
Φ_{lum}	Luminous flux in lumen [lm].
ψ	Field of view of photodiode in degree.
Q	Order of the Volterra series expansion.
$\mathbf{q}$	Vector of input signal samples ($M_f \times 1$).
R	PD responsivity in ampere per Watt [A/W].
R_{photo}	Receiving PD.
ρ_{ϵ_n}	Coefficient of reflectivity of the surface ϵ_n.
$s(t)$	Instantaneous modulated current.
$s(n)$	Discrete-time input modulated signal.
$\hat{s}(n)$	Discrete-time adaptive postdistorter output.
$\mathbf{s}$	Vector of input signal samples at the Volterra series model ($(M_1 + M_2^2) \times 1$).
$s_{CAP}(t)$	CAP modulated signal.
$s_{PAM}(t)$	PAM modulated signal.
$s_{QAM}(t)$	QAM modulated signal.
$S[k]$	Discrete DMT modulated signal.
σ^2	Noise variance.
σ_{shot}^2	Shot noise variance.
σ_q^2	Input signal variance.
$\sigma_{\hat{c}}^2$	Equalized signal variance.
σ_{shot}^2	Shot noise variance.
$\sigma_{thermal}^2$	Thermal noise variance.
t	Time in second [s].
T	Symbol period in second [s].
T_i	Emitting light source i.
θ	Angle of incidence as defined in Fig. 2.4 in degree.
$\theta_{\frac{1}{2}}$	LED semi-angle at half-luminance in degree.
u	Distance from the object to the lens in meter [m].
$u(t)$	Unit step function.
$u(n)$	Symbol before decision at the n-th iteration.
U_{post}	Post-filter matrix.
v	Distance from the lens to the image in meter [m].
$V(\lambda)$	Luminous efficiency function.
$\mathbf{v}$	Vector of feedback filter coefficients ($M_d \times 1$).
V_{pre}	Pre-filter matrix.
$\mathbf{w}$	Vector of feedforward filter coefficients ($M_f \times 1$).
$\mathbf{x}$	Vector of transmitted signals at the array of LEDs ($N_t \times 1$).
$\bar{\mathbf{x}}$	Vector of estimated signals ($N_t \times 1$).

$\hat{\mathbf{x}}$	Vector of pre-coded signals at the array of LEDs ($N_t \times 1$).
$x(t)$	Instantaneous emitted optical power.
$\mathbf{y}$	Vector of received signals at the array of PDs ($N_r \times 1$).
$y(t)$	Instantaneous received signal.
$y(n)$	Discrete-time received signal.
$\hat{\mathbf{x}}$	Vector of post-coded signals at the array of PDs ($N_r \times 1$).

LIST OF ACRONYMS

Acronym	Definition
5G	Fifth Generation of cellular network
6G	Sixth Generation of cellular network
ACO-OFDM	Asymetrically-Clipped Optical Orthogonal Frequency-Division Multiplexing
A/D	Analog-to-Digital
ADC	Analog-to-Digital Converters
APD	Avalanche Photodiode
AWG	Arbitrary Waveform Generator
AWGN	Additive White Gaussian Noise
BER	Bit Error Rate
CAP	Carrierless Amplitude and Phase
CIR	Channel Impulse Response
CP	Cycling Prefix
CSI	Channel State Information
CSK	Color Shift Keying
D/A	Digital-to-Analog
DAC	Digital-to-Analog Converter
DC	Direct Current
DFE	Decision Feedback Equalizer
DMT	Discrete Tulti-Tone
FEC	Forward Error Correction
FFE	FeedForward Equalizer
FFT	Fast Fourier Transform
FIR	Finite Impulse Response
FOV	Field-Of-View
FSE	Fractionnally-Spaced Equalizer
FSE-DFE	Fractionally-Spaced Decision Feedback Equalizer
GaN	Gallium Nitride
GLIM-OFDM	Generalized Light-Emitting Diode Index Modulation
GCD	Greatest Common Divisor
GSM	Generalized Spatial Modulation
GSPPM	Generalized Spatial Pulse Position Modulation
GSSK	Generalized Space Shift Keying
ICI	Inter-Channel Interference
IEEE	Institute of Electrical and Electronics Engineers
IFFT	Inverse Fast Fourier Transform
IM/DD	Intensity Modulation and Direct Detection
ISI	Inter-Symbol Interference
LD	Laser Diode
LED	Light-Emitting Diode
Li-Fi	Light-Fidelity

LIM	Light-Emitting Diode Index Modulation
LMS	Least Mean Squares
LOS	Line-Of-Sight
LU-PMD	Lower-Upper Polynomial Matrix Decomposition
MAC	Medium Access Control
MEMS	Microelectromechanical System
MFTP	Maximum Flickering Time Period
MIMO	Multiple-Input Multiple-Ouptput
MMSE	Minimum Mean Square Error
MPPC	Multiplepixel Photon Counter
MRC	Maximum Ratio Combiner
MS-SM	Multi-Stream Spatial Modulation
NDC-OFDM	Non-Direct-Current-Biased Orthogonal Frequency-Division Multiplexing
NLOS	Non-Line-Of-Sight
NMSE	Normalized Mean Square Error
OLED	Organic Light-Emitting Diode
OOK	On-Off Keying
OFDM	Orthogonal Frequency-Division Multiplexing
OSM	Optical Spatial Modulation
OSM-OFDM	Optical Spatial Modulation Orthogonal Frequency-Division Multiplexing
PAM	Pulse Amplitude Modulation
PAPR	Peak-to-Average Power Ratio
PD	Photodiode
PEP	Pairwise Error Probability
PHY	Physical
PIN	Positive–Intrinsic–Negative
PPM	Pulse Position Modulation
PN	Pseudo-Noise
P/S	Parallel-to-Serial
PSD	Power Spectral Density
PWM	Pulse Width Modulation
QAM	Quadrature Amplitude Modulation
RC	Repetition Coding
RGB	Red-Green-Blue
RF	Radio Frequency
RLS	Recursive Least Squares
S-CAP	Spatial Carrierless Amplitude and Phase
SiPM	Silicon Photo-Multiplier
SM	Spatial Modulation
SMP	Spatial Multiplexing
SNR	Signal-to-Noise Ratio
SPAD	Single-Photon Avalanche Detector
S/P	Serial-to-Parallel
SRRC	Square-Root Raised Cosine
SSK	Space Shift Keying

TIA	TransImpedance Amplifier
TD-SM	Time-Domain Spatial Modulation
U-OFDM	Unipolar Orthogonal Frequency-Division Multiplexing
VLC	Visible Light Communication
VOOK	Variable On-Off Keying
VPPM	Variable Pulse Position Modulation
WDM	Wavelength Division Multiplexing
ZF	Zero Forcing

CHAPTER 1

Introduction

1.1 Motivation

Wireless communications currently constitute a pervasive technology, promoted by the recent development of portable devices such as smartphones, laptops and other wearable devices, whose usage have been massively accepted and adopted by modern societies. According to the Cisco Annual Internet report [27], there will be 5.3 billion total internet users by 2023, up from 3.9 billion in 2018. In this context, the continuous growth of internet traffic entails a need for more bandwidth and higher data rates. Existing wireless communication technologies (e.g. Wi-Fi, Bluetooth, 4G etc...) are based on radio frequency (RF) systems and use the radio frequency range of the electromagnetic spectrum which is strictly regulated and overcrowded. This congestion leads the consortiums for the next generation of wireless communications standards to exploit ever higher frequencies in order to find more available bandwidth, e.g. in the GHz region, where the emerging fifth generation of cellular technology (5G) is operating. From early discussions on the sixth generation of cellular technology (6G), the use of THz bands is envisioned for high-speed wireless communications. However, the implementation of THz transmitter and receiver devices that are commercially-available, affordable and efficient is a major hurdle.

A promising alternative to overcome these restrictions is to transmit information via the optical bands of the electromagnetic spectrum, which remain largely unexploited to date. Visible light communication (VLC) is a form of optical wireless communication that modulates the visible portion of the electromagnetic spectrum (400 - 800 nm) to encode information [65, 60, 94, 48]. An interesting feature of VLC is that the downlink transmission can be leveraged for the dual functionalities of illumination and data communication. To this end, light fixtures made of high-power light-emitting diodes (LEDs) constitute a vehicle for the wide-scale implementation of VLC.

From 2010 onwards, LEDs are increasingly replacing conventional lighting methods such as incandescent or fluorescent light bulbs. Indeed, LEDs provide many advantages such as higher efficiency, longer lifetime, smaller size and lower heat. Moreover, LED lighting is gaining popularity in the domestic and industry sectors, in sync with a growing demand for clean energy, cost-efficient systems and high quality lighting. According to data from

the International Energy Agency [56], the world illumination market share of LED sales rose from 4 % to 46 % between 2013 and 2019 and is projected to take over the market with 87% by 2030. Furthermore, their low-cost and market availability makes them particularly attractive for VLC. Due to aforementioned advantages, it is foreseen that VLC could be integrated as a segment of the next generation of cellular networks to realize highly dense indoor communication networks.

VLC provides many advantages such as a very large and unlicensed spectrum (near 375 THz of available bandwidth), low-cost and commercially-available components, intrinsic robustness against eavesdropping, and immunity to electromagnetic interference. Initially developed in the early 2000's by a research group at the University of Keio in Japan [69], VLC has since drawn a lot of interest in the research community, as it is considered a viable candidate to complement Wi-Fi in indoor environments while relieving pressure on the radio spectrum. Furthermore, VLC is an attractive option with respect to electromagnetic wave-sensitive environments such as aircrafts, hospitals or nurseries. Due to aforementioned advantages, it is foreseen that VLC could be integrated as a segment of the next generation of cellular networks to realize highly dense indoor communication networks. Finally, VLC opens doors to new opportunities and new fields of application such as underwater, outdoor, vehicle-to-vehicle or satellite communications.

Many challenges still need to be addressed in VLC in order to enable a mass adoption of the technology in the near future. One of the main drawbacks of LED-based communications is the limited modulation bandwidth of high-power LEDs, which are designed for illumination functions and are therefore not well suited for communications. To that extent, new spectrally-efficient modulation techniques must be developed to overcome these limitations and increase the modulation bandwidth, hence the achievable throughput. In addition, the LED exhibits a nonlinear behavior which can degrade the system performance. Moreover, blockage issues can arise when obstacles, objects or people stand in the way of the light propagation path, thus reducing the intensity perceived by the user terminal.

1.2 Standardization of VLC

VLC is an emerging communication technology and the standardization process is still in its infancy. Moreover, the multiplicity of standards may be a source of confusion and could lead to compatibility issues. The following elements give an overview of the current progress in the standardization of VLC.

The Institute of Electrical and Electronics Engineers (IEEE) 802.15.7 standard completed in 2011, later revised in 2018 and named "Short-Range Optical Wireless Communications"

[109] defines the physical (PHY) and medium access control (MAC) layers for VLC and optical camera communications. Three different modes of point-to-point operation are proposed depending on the intended application scenario (indoor or outdoor) with variable data rates ranging from a few kbps up to tens of Mbps. The recommended modulation schemes are on-off keying (OOK), variable pulse position modulation (VPPM) and color-shift keying (CSK). In addition, eye safety regulations are met and illumination features such as dimming support and flicker mitigation techniques are provided.

Other established standards can be cited, such as the ITU-T G.9991 standard, completed in 2019 by the International Telecommunication Union, which also provides recommendations with respect to the PHY and MAC layers based on orthogonal frequency-division multiplexing (OFDM) for indoor VLC-based transceivers [58]. In addition, the ongoing IEEE 802.15.13 task group known as "Multi-Gigabit/s Optical Wireless Communications" is working on enabling data rates up to 10 Gbps at distances up to 200 meters, with a focus on industrial applications [108].

Finally, one of the most promising standardization process expected to push forward the implementation of VLC in a wide range of use cases is the IEEE 802.11.bb task group. Initiated in 2018, the latter is working on an amendment to the well-known IEEE 802.11 standard (Wi-Fi) where a new PHY layer will be specified, as well as a few adjustments to the already existing MAC layer [107]. The forecasted achievable minimum single-link throughput is 10 Mbps while the targeted maximum throughput lies in the Gbps range with OFDM-based modulation techniques.

Note, "Li-Fi (Light-Fidelity)" and "VLC" are two terminologies often employed to designate the same technology. However, they differ slightly in that VLC defines any system using the light medium to convey information, whereas Li-Fi is a term coined by Harald HAAS in 2011 aiming to designate a fully networked wireless protocol using visible light [47]. Nonetheless, the term "VLC" is commonly adopted in the standardization process and in the scientific literature.

1.3 Thesis objectives

As discussed previously, many challenges still need to be addressed in VLC. The use of optical front-end components such as the LEDs entails some impediments such as a limited modulation bandwidth (a few MHz), hence a limited throughput. The optical front-end components presently available on the market are primarily designed to fulfill the function of illumination and not that of communication. Furthermore, due to a smaller market, the optical components developed specifically for the function of communication are still

significantly more expensive than the ones designed for the mass market of the lighting industry. The design of VLC systems merging high-speed communication and standard-compliant illumination becomes a challenging task if we aim for a final system which is both low in cost and in hardware complexity. Competitive data rates with other wireless transmission technologies such as Wi-Fi, 4G or the emerging 5G must also be delivered in order to make VLC attractive for wide-scale deployment inside buildings.

This dissertation intends to propose improvements for the physical layer of downlink single-user VLC to achieve high throughput while taking into account the quality of lighting as well as implementation costs. Within this framework, theoretical and simulation investigations are conducted and some results are validated through experiments. The objectives of the thesis are the following:

1. The optimization of data rate on a low-cost point-to-point VLC system compliant with illumination standards in indoor environments (addressed in Chapter 3) .
2. The modeling and compensation of the LED nonlinearity for high modulation orders (addressed in Chapter 4).
3. The evaluation and comparison of state-of-the-art modulation schemes to answer the following question: which modulation scheme is best suited for VLC (addressed in Chapter 5)?
4. The investigation of multiple-input multiple-output (MIMO) techniques by leveraging the multiple light sources in a LED-based luminaire as means to improve the spectral efficiency (addressed in Chapter 6).
5. The theoretical investigation of lower-upper polynomial matrix decomposition (LU-PMD) to mitigate both the inter-channel interference (ICI) and the inter-symbol interference stemming from the difference in optical path lengths in large space scenarios (addressed in Chapter 7).

1.4 Thesis structure

This dissertation is organized in 8 chapters.

Chapter 2 intends to provide useful knowledge on VLC systems for the rest of the thesis. The existing components employed at the transmitter and at the receiver are reviewed along with their advantages and drawbacks. We also introduce the nonlinear characteristics of the LED. Furthermore, we present the indoor lighting metrics and the characteristics of the optical wireless channel both in line-of-sight (LOS) and non-line-of-

sight (NLOS) configurations. Finally, we discuss stat-of-the-art modulation schemes and MIMO techniques.

Chapter 3 describes a VLC transmission over a point-to-point experimental test bench employing carrierless amplitude and phase (CAP) modulation. We first exhaustively describe the CAP modulation format and we then specify the design considerations for indoor illumination in normal working conditions using a low-cost white LED. Lastly, we present the test bench and the throughput optimization approach.

The objective of **Chapter 4** is to develop a simulation model based on the analytical model of the impulse response of a white LED. In addition, to better comprehend the impact of LED nonlinearity, we incorporate two nonlinearity models with different accuracy and complexity, namely the Hammerstein and the Volterra series model. We evaluate the quality of the proposed simulation model by determining the distance between the numerical results and that of the experiment. Furthermore we investigate a postdistortion algorithm based on the Volterra series at the receiver to compensate the LED nonlinearity.

After these three chapters, we will start presenting the contributions of the thesis.

In **Chapter 5**, we compare two modulation schemes, namely pulse amplitude modulation (PAM) and CAP by simulation and by experiment and we investigate the maximum achievable throughput for each modulation while limiting the illumination level to that of a typical office room. The roll-off factor parameter, which is directly related to the signal bandwidth, is also optimized. Furthermore, we study for the first time the impact of LED nonlinearity on high-order PAM and CAP. Lastly, we compare the results with the performance of discrete multi-tone (DMT).

Chapter 6 studies the potential of two MIMO techniques, namely spatial multiplexing (SMP) and spatial modulation (SM) to further enhance the spectral efficiency of VLC systems. We start by presenting the principle of imaging receiver and we then evaluate the performance of the SMP and SM techniques analytically and by simulation. We also experimentally investigate the impact of imager misalignment in case of receiver mobility and propose a bit-loading technique to maintain a quality of communication.

In **Chapter 7**, we propose a novel technique for MIMO VLC, namely the LU-PMD. Initially developed for wideband RF systems, we apply this technique for the first time in VLC for large space indoor environments, where differences in optical path lengths can have a significant impact on the system performance. We demonstrate that the technique can completely cancel the ICI and reduces the MIMO channel into independent single-input single-output (SISO) additive noise channels.

Finally, **Chapter 8** concludes the thesis and propose future research perspectives.

CHAPTER 2

Fundamentals of VLC

2.1 Introduction

In this chapter, we introduce the basic concepts of VLC. The intensity modulation and direct detection (IM/DD) transmission scheme, which is often implemented in practice to perform low-cost and simple modulation and demodulation, is first introduced in Section 2.2. Then, in Section 2.3, the different types of optical front-end components used in VLC are presented. The nonlinear characteristics of the LED are also discussed. In Section 2.4, the illumination metrics for LED lighting are presented along with the health impact of VLC. The characteristics of the optical wireless channel are presented in Section 2.5. Finally the baseband modulation digital modulation schemes employed in VLC are described in Section 2.6.

2.2 IM/DD model

LEDs are incoherent light sources, i.e. the amplitude, frequency and phase of the emitted photons vary randomly in space and time. VLC systems are therefore usually implemented with IM/DD [63]. As shown in Fig. 2.1, the LED driving current $s(t)$ is first modulated by the desired waveform. Then, electrical-to-optical conversion is performed by the LED and the signal $x(t)$ corresponding to the instantaneous emitted optical power is sent through the VLC channel. Note that the LED driving current $s(t)$ must be positive and real, which imposes constraints with respect to the signaling design. The unipolarity (positive) can either be achieved by the addition of a direct current (DC) bias or by employing power switched modulation schemes which are inherently unipolar and positive. Note, the DC bias is added to ensure full swing of the modulated signal in the dynamic range of the LED and also to provide the desired level of illumination.

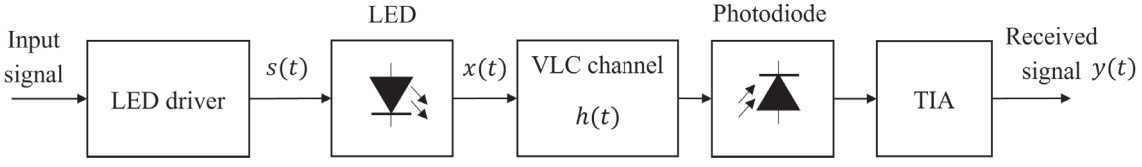

Figure 2.1 Optical wireless transmission with IM/DD.

At the receiver side, a lens focuses the light onto the PD active surface, and the latter performs optical-to-electrical conversion by producing a photocurrent $y(t)$ proportional to the instantaneous received optical power. The photocurrent is then usually converted into a voltage signal using a transimpedance amplifier (TIA). A VLC system can be modeled as a baseband linear system with a finite-length channel impulse response (CIR) $h(t)$, and the received signal can be expressed as

$$y(t) = Rx(t) * h(t) + n(t), \tag{2.1}$$

where R is the PD responsivity, $*$ denotes the convolution product, and $n(t)$ is the noise.

2.3 Optical front-end devices

2.3.1 Types of LEDs

There are different types of LEDs that are possible candidates for VLC.

- **White LED:** The most common type of LED employed for general illumination is the white LED, which consists of a blue LED chip coated with a yellow phosphor that absorbs some of the blue photons and re-emits yellow photons, as described in Fig. 2.2. The yellow photons combine with the blue photons that are emitted directly to produce white light. However, because of the slow relaxation time of the phosphor, the modulation bandwidth is limited to a few MHz.

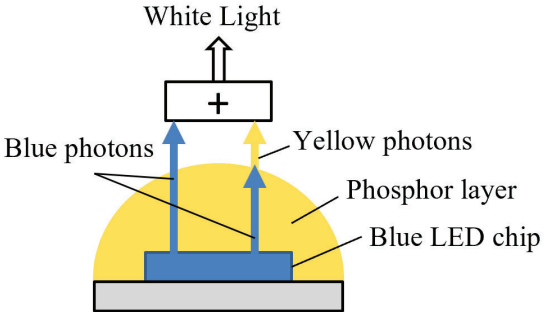

Figure 2.2 Illustration of the principle of a white LED.

- **Red-green-blue LED (RGB LED):** Another type of LED used in indoor illumination is the RGB LED, which is made of three LED dies, allowing more flexibility for color tuning. In recent years, RGB LEDs have drawn a lot of attention in the field of VLC: due to the absence of a phosphor coat, these LEDs generally provide a modulation bandwidth of a dozen MHz. Furthermore, high speed VLC links have been experimentally established by means of the wavelength division multiplexing

(WDM) technique, which consists in modulating the three LED sources independently to increase the throughput [81, 70, 28, 29].

- **Micro-LED:** More recently, the use of gallium nitride (GaN) based micro-LEDs has been investigated as a promising solution to significantly enhance the modulation bandwidth to hundreds of MHz and therefore achieve throughputs on the order of the Gbps [26, 38]. Unfortunately, the manufacturing process is complex and costly. Moreover, their small size, hence limited output optical power, makes them less suitable for indoor illumination. A large quantity of micro-LEDs would be required to provide an adequate lighting level in an indoor environment. It can however be pointed out that their price could drop as production rises in conjunction with higher demand.
- **Organic LED (OLED):** Recent research works have also investigated the potential of OLEDs for VLC. This type of LED is made of organic materials and was originally designed for display technologies, where they emit white light in a fashion similar to that of RGB LEDs. The advantage of OLEDs is the capability of implementation under the form of a large area unit, i.e. a large panel, at extremely low-cost. Thus, luminaires based on OLEDs can provide a high power efficiency, hence sufficient illumination to meet the indoor lighting requirements. On the other hand, OLEDs exhibit a low modulation bandwidth, on the order of several kHz, due to their inherent high plate capacitance [21, 49, 25]. Therefore, the achieved data rates reported in the literature do not exceed a few Mbps [20, 51, 117, 50].
- **Laser diode (LD):** LDs have drawn a lot of interest recently for their potential application in VLC as they exhibit a higher modulation bandwidth, in the GHz range, compared to LEDs. Moreover, white light can be produced in a similar manner as with the LEDs, i.e. by either placing a yellow phosphor film in front of a blue light LD or by combining red, green and blue light beams produced by three distinct LDs. Although extremely high data rates of several tens of Gbps have been reported in the literature [75, 24], LDs are not yet extensively used in VLC because of their drawbacks with respect to the concurrent function of illumination. An LD emits a very intense narrow light beam, which raises concern about on eye safety and homogeneous illumination. As a result, a phosphor-coated diffuser must be added to broaden the spectrum and spatially diverge a blue laser light, at the cost of a drastic throughput reduction [130, 22]. The use of a diffuser allows the launch power constraint at the transmitter imposed by eye safety regulations to be relaxed, but it nonetheless remains lower that of the LEDs [137]. It follows that the latter are better suited for indoor illumination. Finally, the 3-dB bandwidth of LDs can

fully be exploited only if wide bandwidth electronic components, namely amplifiers and photodetectors, are employed which increases the cost of the system and could compromise the viability of an industrial product.

The different types of front-end transmitters in VLC and their characteristics are summed up in Table 2.1.

Table 2.1 Comparison of different transmitters for VLC.

	RGB LED	**White LED**	**Micro-LED**	**OLED**	**LD**
Output optical power	High	High	Low	Moderate	High
3-dB bandwidth	$\sim$ 10 MHz	$\sim$ 1 MHz	$\sim$ 100 MHz	$\sim$ 100 KHz	Very high
Price	Moderate	Low	High	Low	High

2.3.2 Types of PDs

In this section, the two different types of PDs available on the market that can be used for indoor VLC are presented, namely the positive-intrinsic-negative (PIN) PD and the avalanche photodiode (APD).

The most common type is the PIN PD which consists of an intrinsic undoped region, interposed between a n-type and a p-type region, that are heavily doped. To operate as a photodetector, the PIN PD must be reverse-biased to increase the width of the depletion region. When photons with sufficient energy strike the depletion region, electron-hole pairs are generated and current can flow. The more light falls onto the PD active surface, the more photocurrent is generated.

An APD relies on the principle of impact-ionization to create an internal gain and therefore increase the level of sensitivity. In contrast to PIN PDs, APDs are reverse-biased at higher voltages, without exceeding the breakdown voltage. The high bias voltage creates an intense electric field in the avalanche region so that the carriers generated by the incident light collide with the lattice atoms, generating new electron-hole pairs, and the impact-ionization process repeats. This mechanism leads to a significantly improved SNR compared to PIN PDs. On the other hand, the multiplication process generates an excess of shot noise. Therefore, APDs are more suited for low light scenarios with weak incident optical power.

The excess noise in APDs can be avoided by operating the APD in the Geiger mode, i.e. when the device is operated at a voltage above breakdown. Consequently, a single photon can trigger an avalanche by creating an electron-hole pair. Detection devices to function in this regime represent a relatively new technology designated single-photon avalanche detector (SPAD). They consist of an APD in series with a quenching device, a resistor for

instance, that lowers the bias voltage down to the breakdown voltage and quenches the avalanche [23]. The carriers are no longer able to accelerate and collide with the lattice atoms. The downside of SPADs is that once a photon is detected, there is a short recuperation interval, known as the dead time, during which detection is impossible. In addition, the output signal is not proportional to the light intensity. To overcome this limitation, SPADs can be placed in arrays to form a device known as silicon photo-multiplier (SiPM) or multiplepixel photon counter (MPPC) [141]. It is reported in [140] that commercial off-the-shelf arrays of SPADs can provide more sensitivity in weak illuminance conditions as APDs, but are not yet as effective in the presence of strong background light because they are shot-noise limited.

Although existing SiPMs are still expensive components, they are expected to become more sensitive than any other type of PDs [1]. The PIN PDs remain currently the most affordable and effective solution for the design of low-cost and simple VLC receivers. The typical characteristics of APD and PIN PDs are presented in Table 2.2.

Table 2.2 Comparison of characteristics of APD and PIN PDs when applied to VLC.

	PIN PDs	**APD**
Sensitivity	Low	High
Noise level	Low	High
3-dB bandwidth	10 MHz to 10 GHz	100 MHz to 10 GHz
Linearity	High	Low
Price	Low	High

2.3.3 LED nonlinearity

VLC systems include components with nonlinear characteristics such as LEDs, PDs, digital-to-analog converters (DACs) and analog-to-digital converters (ADCs) which cause signal distortions and degrade the system performance. The most severe impairments stem from the LED nonlinearity which drastically limits the transmission rate [80, 143, 32, 33].

The LED electro-optical transfer characteristic relating the forward current and the output optical power denoted P_{opt}. is a nonlinear function as described in Fig 2.3. When full swing of the modulated input current is enforced, the variations of radiated optical power with respect to the driving signal cause signal distortions which degrade the overall performance of the system. In Fig 2.3, the output optical signal $x(t) = P_{opt}(s(t))$ is a distorted replica of the input modulated current $s(t)$. Considering the LED nonlinearity, the system model described by (2.1) can thus further be written as

$$y(t) = RP_{opt}\left(s(t)\right) * h(t) + n(t). \tag{2.2}$$

The LED is operated within a fixed dynamic range: the input current should be positive and the higher peak of the signal should not exceed the maximum permissible current value recommended by the LED manufacturer to prevent overheating and damaging of the device.

Moreover, the carrier-density response of the LED is frequency-dependent and therefore the LED nonlinearity has a memory effect: the present output does not only depend on the present input but also on past values. As a matter of fact, this memory effect grows with the signal bandwidth, and thus the nonlinear behavior of the LED cannot be ignored at high transmission rates [135, 64]. Furthermore, The LED nonlinear characteristics may vary over time due to thermal effects and aging of the component [103].

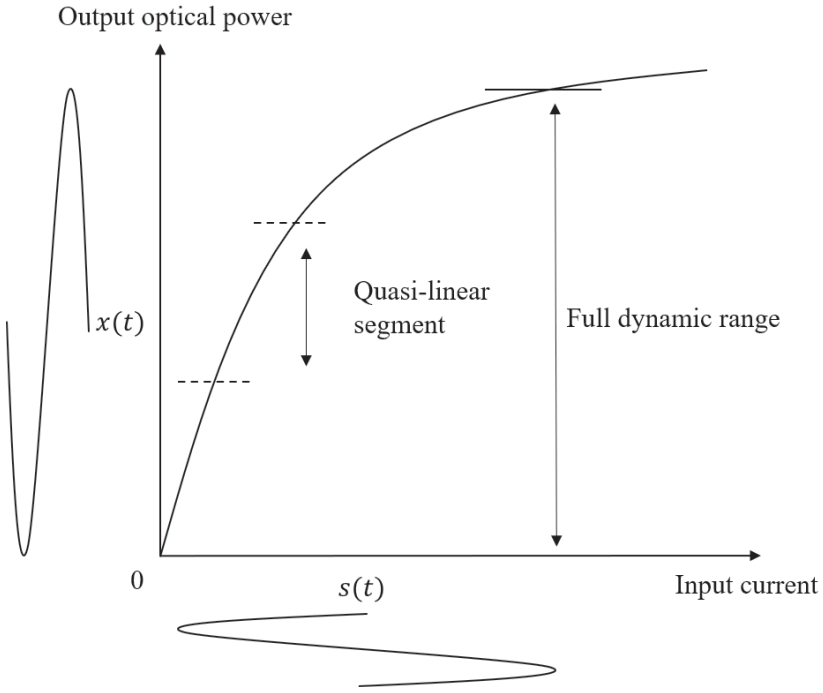

Figure 2.3 Nonlinear transfer characteristic of an LED.

In order to cope with the nonlinearity effects, the LED can be operated over a smaller segment of the transfer characteristic that is quasi-linear. However, this method drastically reduces the signal power. Advanced LED nonlinearty compensation techniques are discussed in detail in Chapter 4.

The peak-to-average power ratio (PAPR) of the modulated signal $s(t)$ is an important metric with regard to the impairments caused by the LED nonlinearity. The PAPR is defined as the ratio between the instantaneous electrical power $s(t)^2$ and the average electrical power $\mathbb{E}[s(t)^2]$, i.e.

$$\text{PAPR} = 10\log_{10}\left(\frac{s(t)^2}{\mathbb{E}[s(t)^2]}\right). \tag{2.3}$$

It can be assumed that modulations with higher PAPR will suffer more degradation due to the LED nonlinearity. In that sense, single-carrier modulation schemes such as PAM or CAP are expected to be less affected by the LED nonlinearity compared to multi-carrier techniques such as DMT since the former schemes exhibit lower PAPR [67]. In order to reduce the PAPR of DMT, bilateral amplitude clipping is usually be applied to fit the DMT-modulated signal to the desired dynamic range. The drawback of this technique is the clipping noise, that can significantly degrade the system performance [31].

2.4 Illumination analysis for indoor VLC systems

2.4.1 Lighting properties of LEDs

There are two important metrics with regard to LED-lighting. The first one is the luminous flux Φ_{lum} in lumen (lm) which quantifies the radiant power from the LED as perceived by the human eye. It can be expressed as follows [41]:

$$\Phi_{lum} = K_m \int_{380}^{780} P(\lambda)V(\lambda)d\lambda, \tag{2.4}$$

where λ is the wavelength, K_m with value 683 lm/W is the maximum luminous efficacy (ratio of luminous flux to radiant power), $P(\lambda)$ is the spectral power density function which represents the amount of power per wavelength, and $V(\lambda)$ is the luminous efficiency function which describes the spectral sensitivity of the human eye for each wavelength.

The second important metric when it comes to evaluating the illumination distribution in space is the horizontal illuminance E_h which is defined as the luminous flux per unit area [lm/m^2] and is measured in lux (lx). The horizontal illuminance is given by the following expression [118]:

$$E_h = (m+1)\frac{\cos^m(\phi)\cos(\theta)}{2\pi d^2}\Phi_{lum}, \tag{2.5}$$

where ϕ is the angle of emergence with respect to the transmitter normal axis, θ is the angle of incidence with respect to the receiver normal axis, d is the distance between the emitter and the receiver as shown in Fig. 2.4, m is the order of Lambertian emission defined as $m = \frac{-\ln(2)}{\ln(\cos(\theta_{\frac{1}{2}}))}$ and $\theta_{\frac{1}{2}}$ corresponds to the semi-angle at half-luminance of the LED.

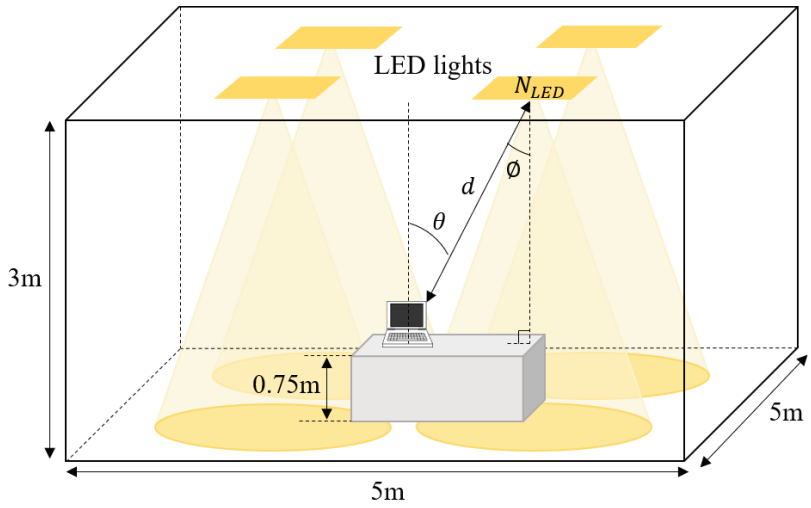

Figure 2.4 VLC transmission in an office room.

To provide a sufficient illumination level in a room, the luminaires are commonly made of arrays of LEDs [45]. The total horizontal illuminance E_h^{tot} is defined as the sum of the contribution of each LED and can be expressed as

$$E_h^{tot} = N_{LED} E_h, \tag{2.6}$$

N_{LED} being the number of LED chips in the luminaire.

2.4.2 Lighting requirements

The illumination standards provide recommendations for lighting applications based on factors such as visual ergonomics, performance needs, safety or economy. To this extent, the European norm EN 12464-1 defines a framework for lighting of various interior areas, tasks and activities [17]. Considering normal working conditions, the latter gives recommendations for lighting parameters including illuminance levels, luminance distribution, directionality and variability of light, colour rendering, flicker and glare. Due to the LEDs radiation pattern, the task area usually located right below the light source has the highest illuminance level and it decreases in the immediate surrounding areas. Some examples of illuminance levels extracted from the EN 12464-1 standard according to the area or the

type of activity are given in Table 2.3. These requirements can be taken into account for the design of VLC-based transceivers in indoor environments to determine the number of LED chips and the required amount of power.

Table 2.3 Indoor illuminance level recommendations (EN 12464-1 Std.).

Work area / Activity	Illuminance
Circulation areas, corridors, restrooms, stairs, elevators	50 - 100 lx
Entrance halls, cloakrooms, lounges	100 - 200 lx
Store rooms (packing, handling, etc.)	100 - 300 lx
Auditorium, lecture halls, offices, conference rooms, meeting rooms (reading, writing, data processing, etc.)	500 lx
Fine precision tasks (painting, technical drawing, sewing, etc.)	500 - 1000 lx
High precision tasks (precision mechanics, quality control, color inspection, metal engraving etc.)	1000 - 2000 lx

2.4.3 Eye safety requirements

The emissions from a VLC transmitter are tightly controlled due to safety requirements. An overview of the health impacts of VLC are presented here.

Firstly, the eye's ability to focus the light onto the retina can cause biological effects that strongly depend on the wavelength, the light intensity and the duration of exposure. There are two categories of hazards: thermal and photochemical. Thermal hazards are related to overheating of the retinal tissue whilst photochemical hazards correspond to the decomposition of pigments in the photoreceptor cells caused by strong incident blue light. In this respect, LEDs are safer than laser diodes because the emitted light is more diffuse and less intense. In fact, LEDs designed for illumination purposes exhibit a wide angle of emission, thus limiting the amount of power falling onto the eye retina. However, white LEDs or RGB LEDs have a pronounced peak in the blue range around 450 nm and the photochemical (or blue-light) hazard is the dominant source of hazard for exposure times greater than 10 s according to the european norm EN 62471 for "*photobiological safety of lamps and lamp systems*" [35]. The standard also specifies maximum irradiance levels

measured in $W.m^2.sr^{-1}$ and classifies the LED devices into risk groups. The non-coherent diffuse continuous-wave LEDs are considered completely eye-safe if the radiance measured at a distance of 200 mm in the direction of maximal directivity within 10 000 s is less than 100 $W.m^2.sr^{-1}$. The average optical power of the signal should therefore be adjusted at the transmitter side to guarantee that this level is respected.

Secondly, the VLC emissions must be flicker-free to avoid harmful effects on human health such as photosensitive epilepsy or headaches. A useful metric is the maximum flickering time period (MFTP), which is defined as the period over which the human eye cannot detect any brightness variation. The MFTP must be less than 5 ms to be considered safe [119]. Equivalently, the modulation speed must be higher than 200 Hz. This is generally not an issue at high data rate since LEDs can be modulated at speeds far faster than the human eye can perceive. However, at lower throughput, flicker can arise from long series of zeros and ones. To prevent this issue, run-length limited codes can be employed, e.g. Manchester coding.

2.5 Optical wireless channel

In this part, we first present the different topologies employed for the dual-purpose of communication and illumination. Then, an analytical description of a typical indoor VLC channel is presented. We also derive an expression for the CIR and highlight the frequency selectivity in VLC mainly due to the optical front-end response.

2.5.1 Topologies

Several topologies are possible to establish a VLC communication link between a transmitter and a receiver. If we consider indoor illumination as a key feature of the VLC system, two configurations are commonly employed in indoor environments and extensively studied in VLC, namely LOS and NLOS. They differ in whether a direct path (also called "LOS component") exists between the transmitter and the receiver or not. In a LOS configuration, the light propagates directly to the receiver, and via multiple reflections on the walls and on the objects within the room. These reflected paths are collectively referred to as "diffuse link". In a NLOS configuration, there is no direct path and the receiver collects light solely from the diffuse link. The two configurations are presented in Fig. 2.5. The direct path is represented by a solid line, while the diffuse reflections are represented by dashed lines.

2.5.2 VLC channel model

The CIR of the static VLC channel $h(t)$ is defined as the received signal when the emitted signal is the Dirac delta function $\delta(t)$ and can be written as

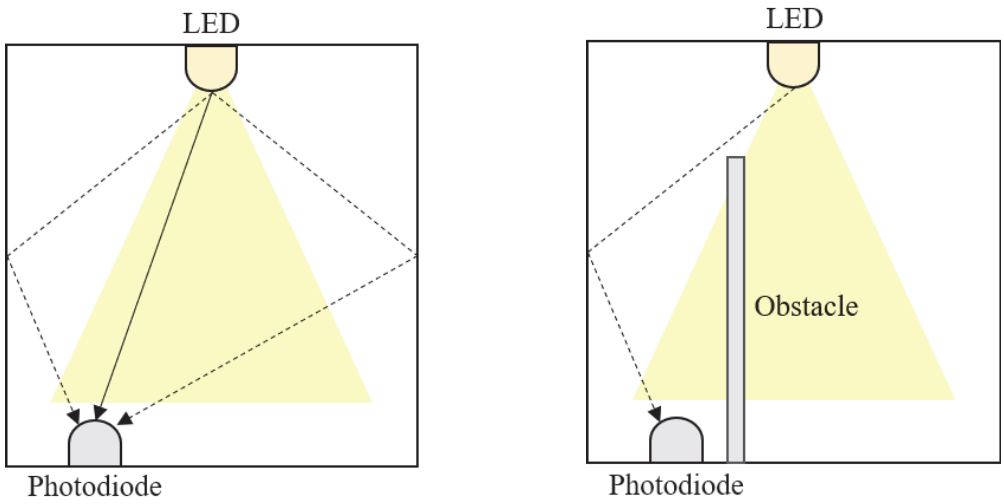

(a) LOS configuration. (b) NLOS configuration.

Figure 2.5 Possible topologies for indoor VLC.

$$h(t) = h_{LED}(t) * h_{VLC}(t), \tag{2.7}$$

where $h_{LED}(t)$ is the LED response, and $h_{VLC}(t)$ is the impulse response with respect to the free space propagation of the light rays. The LED response can be modelled as a simple first-order low-pass filter such that [138]

$$h_{LED}(t) = e^{-2\pi f_0 t}, \tag{2.8}$$

where f_0 denotes the 3-dB modulation bandwidth of the LED. The impulse response $h_{VLC}(t)$ is the sum of the contribution from the direct propagation path $h_{direct}(t)$ and the diffuse link $h_{diff}(t)$ [104], i.e.

$$h_{VLC}(t) = h_{direct}(t) + h_{diff}(t). \tag{2.9}$$

Assuming the emitter has a generalized Lambertian pattern, the impulse response of the direct path $h_{direct}(t)$ is defined by the following mathematical expression [41]:

$$h_{direct}(t) = \begin{cases} \frac{(m+1)A}{2\pi d^2} \cos^m(\phi) \cos(\theta) \delta(t - \frac{d}{c}) & 0 \leq \theta \leq \psi, \\ 0 & \theta > \psi, \end{cases} \tag{2.10}$$

where A is the PD active surface, c is the speed of light and ψ is the field-of-view (FOV) of the PD. On the other hand, the diffuse component impulse response $h_{diff}(t)$ can be decomposed into an infinite number of bounces on room surfaces which arrive successively at the receiver. Considering N_{LED} sources on the ceiling, the contribution of the diffuse $h_{diff}(t)$ from the sources T_i to a receiving PD R_{photo} can be calculated based on an iterative algorithm [41] such as

$$h_{diff}(t) = \sum_{i=1}^{N_{LED}} \sum_{k=0}^{+\infty} h_{diff}^{(k_r)}(t, T_i, R_{photo}), \tag{2.11}$$

After k_r reflections ($k_r \geq 1$) the diffuse impulse response can be approximated by [41]

$$h_{diff}^{(k_r)}(t, T_i, R_{photo}) = \sum_{n=1}^{\Omega} \rho_{\epsilon_n} d\epsilon_n h_{diff}^{(k_r-1)}(t, T_i, \epsilon_n^r) * h_{diff}^{(0)}(t, \epsilon_n^t, R_{photo}). \tag{2.12}$$

All room surfaces are divided into Ω small reflecting elements ϵ_n with a Lambertian radiation pattern, a coefficient of reflectively ρ_{ϵ_n}, and a surface $d\epsilon_n$. When ϵ_n acts as a transmitter with respect to the receiver PD R_{photo}, it is denoted ϵ_n^t and when it acts as a receiver with respect to the transmit light source T_i, it is denoted ϵ_n^r. Note that $h_{diff}^{(0)}(t, \epsilon_n^t, R_{photo})$ represents the LOS component impulse response between the surface element ϵ_n and the PD R_{photo}.

Because of the slow motion of people and objects within the room, the channel variations in time are very slow and the VLC channel can therefore be considered as quasi-static. An important metric of the VLC channel is the channel DC gain H_{DC} which relates the emitted mean optical power P_t and the received mean optical power P_r, i.e.

$$P_r = H_{DC} P_t. \tag{2.13}$$

The channel DC gain is the DC component of the Fourier Transform of the total CIR defined in (2.9) and can be expressed as [41]

$$H_{DC} = \int_{-\infty}^{\infty} h_{VLC}(t) dt. \tag{2.14}$$

The total DC gain includes the DC gains from the direct path and the multiple reflections. Investigations on the indoor VLC channel have shown that the direct path is significantly stronger compared to the diffuse link [16]. In other words, the diffuse reflections within a typical room represent a negligible fraction of the total received optical power. Therefore, it is often assumed that only the direct path exists with respect to the link budget analysis. This assumption is verified later in simulation in 2.5.5. Based on this, the diffuse link contribution is negligible compared to the direct path and using (2.10), the channel DC gain H_{DC} can be expressed as

$$\begin{aligned} H_{DC} &= \int_{-\infty}^{\infty} h_{direct}(t)dt \\ &= \begin{cases} \frac{(m+1)A}{2\pi d^2}\cos^m(\phi)\cos(\theta) & 0 \leq \theta \leq \psi, \\ 0 & \theta > \psi. \end{cases} \end{aligned} \tag{2.15}$$

2.5.3 Noise sources in VLC

There are two dominant types of noise that impair the communication quality in a VLC link, namely shot noise and thermal noise.

Shot noise: Shot noise comes from the randomness of the photon arrivals on the photodetector area. Due to the quantum nature of light, the arrivals of photons on the photodetector active area are not homogeneously distributed in time. For a low received optical power, i.e. few incident photons, the detection of optical signals can be described by a photon-counting model: the number of photons N_{photon} counted within a known time window t follows a stochastic process, that can mathematically be described by a Poisson probability distribution defined as

$$P(N_{photon} = k) = \frac{\exp(-\lambda_e t)(\lambda_e t)^k}{k!}, \qquad k \in \mathbb{R}^+, \tag{2.16}$$

where λ_e is the expected number of photons per interval. Moreover, each photon incident on the detection area of the photodetector generates an electron-hole pair with a probability known as the quantum efficiency. As a result, the fluctuations are passed on to the produced photocurrent which also has a Poisson distribution. These fluctuations are referred to as shot noise, to which both the ambient light and the data-carrying LED contribute. The ambient light comes from natural (sunlight) and artificial lighting sources (fluorescent lamps, incandescent lamps and other LED-based lighting fixtures).

For a large λ_e, a Poisson random variable can be approximated by a Gaussian distribution with same variance by virtue of the central limit theorem. In other words, under the assumption of a high received optical power, shot noise can be modeled as additive white signal-dependent Gaussian noise. It is noteworthy that in a daylight configuration, the ambient light contribution is typically more significant compared to that of the information signal. In this case, it is assumed that shot noise is independent of the transmitted optical signal.

Thermal noise: is induced by the random motion of electrons in the TIA of the receiver circuit and can be modeled as additive white Gaussian noise (AWGN). Thermal noise tends to be the dominant source of noise in absence of strong background illumination [63]. In addition, thermal noise is generated independently of the information signal.

Therefore, since the two major sources of noise (shot noise and thermal noise) can be modeled as two uncorrelated AWGN sources, the overall noise in an IM/DD-based VLC link is modeled as zero-mean real-valued AWGN of unilateral power spectral density N_0 [41, 63, 30]. The noise variance denoted σ^2 is the sum of the shot noise variance σ^2_{shot} and the thermal noise variance $\sigma^2_{thermal}$ [69, 128]. Therefore, the noise variance σ^2 can be expressed as

$$\sigma^2 = N_0 B, \tag{2.17}$$

and

$$\sigma^2 = \sigma^2_{shot} + \sigma^2_{thermal}, \tag{2.18}$$

where B is the overall system bandwidth over the positive frequency range.

2.5.4 SNR in VLC

In VLC, the received electrical signal-to-noise ratio (SNR) is an important metric to evaluate the quality of transmission over a given channel and is defined as the ratio between the mean electrical power of the received signal and the noise power. The electrical SNR can be written as [41]

$$\text{SNR} = \frac{R^2 {P_r}^2}{\sigma^2} = \frac{R^2 H^2_{DC} {P_t}^2}{\sigma^2}. \tag{2.19}$$

Note that the received electrical SNR is proportional to the square of the received optical power.

2.5.5 Evaluation of received power in LOS and NLOS configuration

A numerical analysis is presented here to assess the received SNR in a LOS and a NLOS configuration. The environment considered is a typical office room of size 5 m × 5 m × 3 m with the parameters given in Table 2.4. As depicted in Fig. 2.6, the light fixtures are arranged symmetrically on the ceiling to insure a wide area illumination coverage. Here, only the first bounce is considered for the sake of simplicity ($k_r = 1$). Moreover it was shown that higher-order reflections have a negligible contribution [41]. Fig. 2.7 (a) and (b) show the optical power distribution in a LOS scenario (direct path and diffuse link) and in a NLOS scenario (diffuse link only), respectively. When the receiver is placed in the middle of the room on a desk at 0.75 m above the floor, the collected light coming from the multiple bounces on the four walls represents only ~ 8 % of the total received optical power. In a NLOS configuration when the direct path is blocked, the receiver perceives some light intensity, but since the SNR depends on the amount of received optical power, the performance is significantly degraded compared to the LOS case. However, data communication in a NLOS situation can still be maintained as reported in [34]. It is noteworthy that in VLC, the SNR is usually high, which is a consequence of the brightness levels recommendations for indoor facilities [45]. Indeed, based on simulations for the LOS scenario, the horizontal luminance is calculated to be 468 lx with (2.5) when the receiver is located in the center of the room, and the received SNR is determined to be 65.6 dB.

The channel model at this point in the document is characterized only by the power loss between the emitter and the receiver due to transmission through the optical wireless channel. In the next section, we will discuss the frequency selectivity of the VLC channel which arises from other data-carrying luminaires and the LED response.

2.5.6 Inter-symbol interference in VLC

Frequency-selective channels, or equivalently time-dispersive channels, can cause inter-symbol interference (ISI) when the previously transmitted symbols interfere with the actual received symbol. ISI induces severe distortions on the transmitted signal, thus degrading the reliability and the quality of the communication link.

As demonstrated in 2.5.2, the diffuse component power contribution is negligible with respect to that of the LOS component, and thus the reflections on walls, obstacles or humans have little influence on the frequency selectivity of the channel [16].

Table 2.4 Parameters used for simulations.

Parameter	Value
LED optical output power	171 mW
LED semi-angle at half-luminance $\theta_{\frac{1}{2}}$	55°
Surface d_{ϵ_n}	0.04 m^2
Number of LEDs in a luminaire N_{LED}	80
PD active area A	1 cm^2
Wall reflectivity ρ_{ϵ_n}	0.8
Receiver FOV ψ	70°
Modulation bandwidth B	1 MHz
Noise PSD N_0	10^{-21} W/Hz [67]

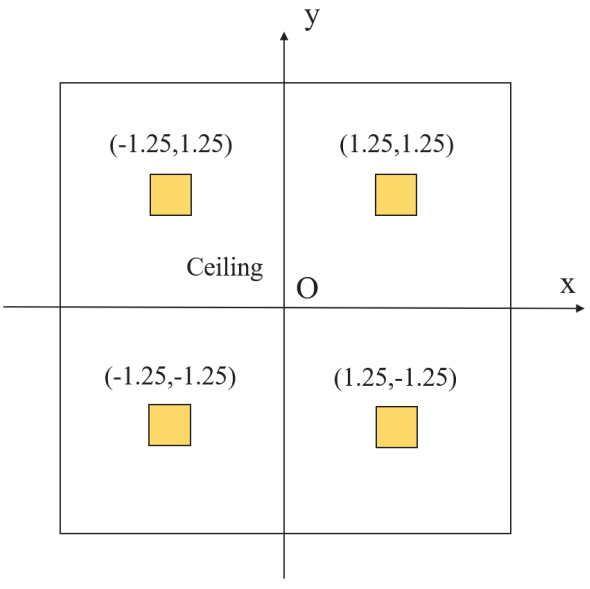

Figure 2.6 LED coordinates on the ceiling (all LEDs in a luminaire are assumed to be located at the same point).

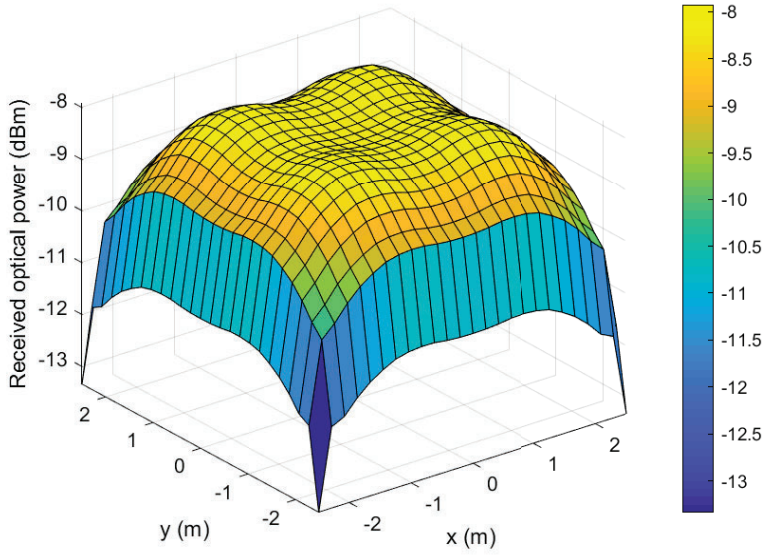

(a)

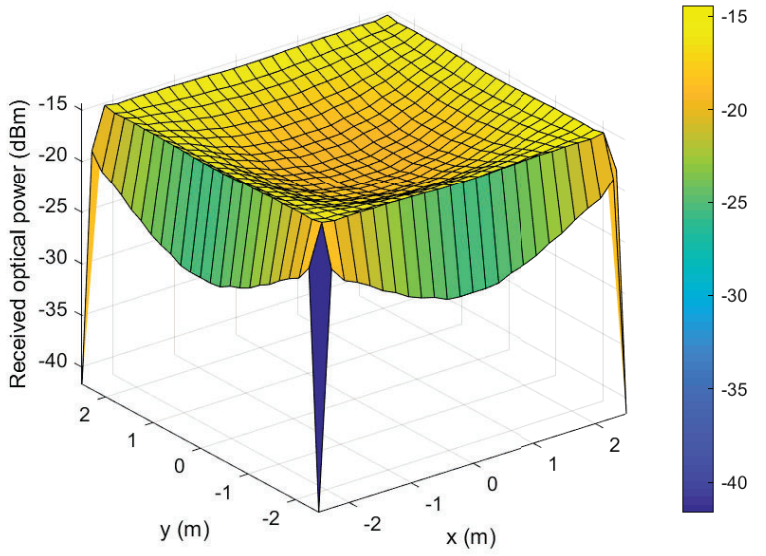

(b)

Figure 2.7 Received optical power distribution on the receiver plane in (a) LOS configuration (direct path + reflections) and (b) NLOS configuration (reflections only).

ISI can arise from the propagation delays of the LOS components between the LEDs and depends on the configuration of the room and the distribution of the LEDs on the ceiling [45]. The receiver receives multiple signals coming from the the numerous data-carrying light fixtures on the ceiling. If the largest difference in the length of the optical paths is significant with respect to the symbol period, the signal will be subject to ISI which limits the transmission rate of the system. Considering a typical office room and the LED distribution in Fig. 2.6, the maximum propagation delay between the direct components is of only 9.7 ns, which occurs when the receiver is located in the corner of a room at 0.75 m above the floor (worst scenario). In the center of the room, there is no delay of propagation between the LOS components assuming synchronously driven transmit LEDs. Therefore, ISI stemming from delays of propagation between the different transmitters is a problem that can arise only in very specific cases, i.e. when operating at very high data rates where the system baud rate is on the order of hundreds of Mbaud and / or the VLC system is implemented in a large indoor environments with high ceilings such as convention centers, shopping malls, factories, lecture halls or airports.

Typically, the frequency selectivity of the VLC channel is essentially introduced by the front-end components and more specifically the LED response, the latter acting as a low-pass filter. The PD 3-dB bandwidth is in fact usually much larger than the LED 3-dB bandwidth, therefore ISI occurs essentially when the LED is operated beyond its 3-dB bandwidth. In the context of high speed communication, the signal bandwidth is usually larger than the 3-dB bandwidth, which is limited to a few MHz in the case of white LEDs.

2.5.7 Emitter 3-dB bandwidth enhancement

Given that the VLC channel has a low-pass behavior due to the LED frequency response, several hardware solutions can be deployed to increase the 3-dB bandwidth of the emitter and therefore employ a larger signal modulation bandwidth.

A first approach consists in adding a simple first-order RC pre-equalizer circuit at the transmitter [123, 52] or at the receiver [72] to compensate the low-pass response of the LED and increase the usable modulation bandwidth from a few MHz to several tens of MHz. More complex equalizer circuits can be used to further enhance the 3 dB bandwidth of the emitter employing white LEDs. For instance, modulation bandwidths of 520 MHz and 151 MHz have been reported in [139] and [77], respectively. However, the drawback of this technique is the additional hardware complexity.

Another simple approach consists in placing a bandpass blue filter in front of the PD to collect solely the blue photons and therefore mitigate the slow response of the phosphor

layer of the white LED. The blue filter has also the virtue of reducing the shot noise at the receiver caused by sunlight [57]. However, several studies have demonstrated that the blue filter has negligible impact on the overall performance of the VLC system, due to the drastic drop of SNR at the receiver [115, 113]. Therefore, the use of a blue filter is based on a trade-off between the LED modulation bandwidth enhancement and the received power.

2.6 Digital modulation schemes

In this section, we present the main digital modulation schemes that can be used in VLC. Since IM/DD is employed, the modulated signal driving the LED must be real-valued and unipolar non-negative. Modulation schemes can be divided into two groups, namely the single-carrier and the multi-carrier modulation schemes. The difference is that in multi-carrier modulation systems the signal bandwidth is divided into smaller sub-bands (also referred to as subcarriers) of width ΔB, which transmit independent data symbols, whereas single-carrier modulation schemes exploit the whole bandwidth to transmit symbols, as shown in Fig. 2.8. It should be noted that, for both modulation groups, the modulated signal remains in the baseband domain in VLC, i.e. the lower side band extends all the way to $f = 0$. As a result, the transmitted signal spectrum has a low-pass characteristic.

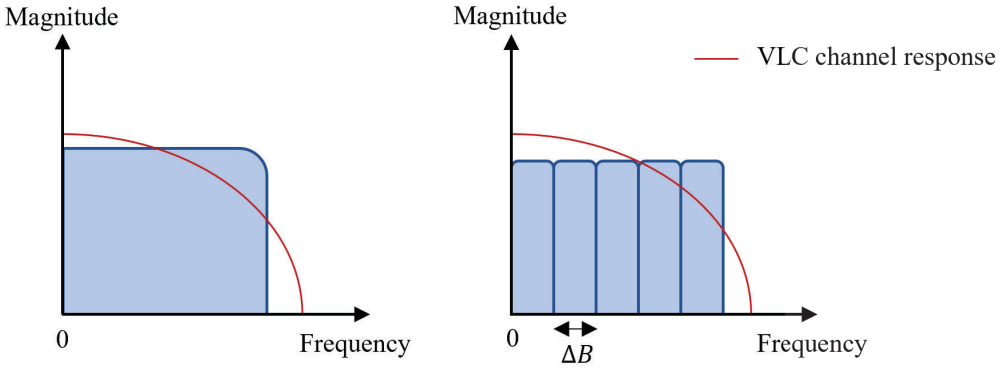

Figure 2.8 Schematic representation of the spectrum in the frequency domain over the positive frequencies for single-carrier modulation schemes (left) and multi-carrier modulation schemes (right) with the VLC channel response.

2.6.1 Single-carrier modulation schemes

There are several ways to encode information in the transmitted signal. Below are listed the most popular single-carrier modulation techniques for VLC.

- **OOK:** OOK modulation is the most straightforward method to encode data and consists in simply switching the LED on and off for bit 1 and 0 respectively. The duty cycle of the pulse can be adjusted, resulting in a variable OOK (VOOK) which supports dimming control [76].
- **Pulse width modulation (PWM):** PWM is a pulse-based modulation scheme where the information is encoded in the width of the transmit pulse. By assigning different duty cycles depending on the incoming data, the average optical power fluctuates, thus compromising stable illumination. Therefore, PWM is not suitable for joint data transmission and indoor illumination.
- **Pulse position modulation (PPM):** In PPM, the data is encoded in the position of the pulse. The symbol period in a M-ary PPM is divided into M-slots, to which the transmitted bits are assigned. PPM and PWM can also be combined to adjust the mean emitted optical power by varying the pulse width, i.e. the duty cycle, the latter being kept constant over a symbol period to guarantee stable illumination.
- **PAM:** PAM is a modulation scheme where the information is encoded in the amplitude of the transmitted pulse. PAM requires a higher SNR than PPM to operate at the same bit error rate (BER). However, PPM requires more bandwidth [136, 39]. PAM is nowadays usually preferred over PPM and OOK for indoor application to achieve high transmission speeds, as the SNR available at the receiver is sufficiently high [45, 78]. On the other hand, due to the multiple amplitude levels, PAM is less robust against the LED nonlinear distortions than the constant pulse amplitude techniques such as PPM or OOK.
- **CAP modulation:** CAP is a variant of quadrature amplitude modulation (QAM) where instead of a sinusoidal oscillator, a pair of finite impulse response (FIR) filters is employed to transmit in-phase and quadrature components through orthogonal channels. The orthogonality is maintained due to the property of the filters which form a Hilbert transform pair i.e., they are 90° out of phase.

2.6.2 Multi-carrier modulation schemes

As described in Fig. 2.8, multi-carrier techniques can have better tolerance against the low-pass effect of VLC channels since by lowering the bandwidth requirement for each sub-band, the attenuation over the signal frequencies is reduced. However, the number of sub-bands must be sufficiently high, leading to large PAPR issues. The main multi-carrier modulation techniques are listed below.

- **DMT:** DMT is a modulation technique similar to OFDM [70, 121, 9, 11] which was originally developed to overcome severe channel frequency selectivity based on the

following premise: the modulated signal spectrum is divided into smaller frequency bands named "subcarriers" which individually experience a flat-fading channel. As a result, DMT is very robust against ISI and equalization requires only one coefficient per subcarrier. The difference with conventional OFDM employed in RF systems is that in DMT, bit loading is usually applied based on the SNR of each subcarrier, that is, more bits are allocated to subcarriers with high SNR. This operation requires a feedback on the quality of the channel, and thus DMT is implemented with slowly varying channels such as cabled channels (e.g. asymmetric digital subscriber line (ADSL)). In addition, DMT modulation is modified to meet the requirements of VLC systems and generate a real signal. Hermitian symmetry must be applied prior to the inverse fast Fourier transform IFFT operation in order to obtain real-valued signal. However, the Hermitian symmetry entails a loss of spectral efficiency by factor 2, since Hermitian symmetry adds redundant conjugate symbols prior to the IFFT operation. Note, DMT is also referred to as DCO-OFDM in the literature because a DC bias is added to the OFDM-generated signal to transmit unipolar and positive values.

- **Asymetrically-clipped optical OFDM (ACO-OFDM)**: ACO-OFDM was proposed to avoid a DC bias addition and to directly generate a unipolar signal [8]. In ACO-OFDM, only the odd subcarriers are modulated and the even subcarriers are assigned to zero. Another difference in the signal generation between DCO-OFDM and ACO-OFDM is the clipping operation block. In DCO-OFDM, bilateral clipping is performed, whereas in ACO-OFDM; the signal is clipped at zero and only the positive part of the waveform is transmitted. The advantage of this technique is that the clipping noise in ACO-OFDM falls on the even subcarriers and not on the data-carrying subcarriers. Investigations in [10] have shown that ACO-OFDM is more power efficient than DCO-OFDM. However, the spectral efficiency in ACO-OFDM is divided by a factor of 2 compared to DCO-OFDM.
- **Flip-OFDM or unipolar OFDM (U-OFDM)**: Flip-OFDM was proposed in [37] as an alternative technique to ACO-OFDM and DCO-OFDM. In Flip-OFDM, the transmitted signal is generated in a similar way as in DCO-OFDM. However the positive and negative samples are separated into two frames that are transmitted successively. The absolute value of the negative samples is taken for the negative frame so that the frame is unipolar and positive. As in ACO-OFDM, there is no need for DC bias addition since the generated waveform is unipolar and the BER performance is identical. The advantage of Flip-OFDM over ACO-OFDM consists in a reduction by half of the hardware computational complexity [37].

- **Multi-band CAP**: CAP modulation can be extended to a multi-band modulation format, namely multi-band CAP, where the signal bandwidth is divided into sub-bands. Analogously to DMT, by virtue of lowering the bandwidth requirement for each sub-band, the attenuation over the signal frequencies due to the low-pass channel is reduced. Furthermore, adaptive bit-loading can be applied to optimize the constellation size in each sub-band depending on the channel attenuation, and thus improve spectral efficiency. Nevertheless, it was shown in [3] that the PAPR and implementation complexity constitute impediments in multi-band CAP, which both grow with the number of sub-bands. Considering the limited LED dynamic range, a power penalty is induced at the transmitter.

2.6.3 Digital equalization techniques

Digital equalization techniques are widely used in practice to mitigate the ISI from the LED frequency-selective response and to help the VLC system operate beyond the 3-dB bandwidth of the LED. Digital equalization allows hardware alleviation at the expense of computational complexity. For single-carrier modulation schemes (e.g. PAM or CAP), various types of time-domain equalizers can be employed at the receiver. A linear feed-forward equalizer (FFE) can be used with either zero-fording (ZF) or minimum mean square error (MMSE) criteria: the former completely eliminates the ISI to the detriment of noise amplification, while the latter performs a trade-off between channel inversion and noise enhancement. Alternatively, nonlinear decision feedback equalizers (DFEs) limit the noise amplification by adding a feedback path to a FFE structure into which previous estimated symbols are fed. As opposed to single-carrier signals with time-domain equalizers, multi-carrier modulation schemes such as DMT benefit from simpler equalization, as each subcarrier experiences a flat fading channel and therefore requires a single-tap equalizer. Furthermore, inspired by the equalization process of DMT, frequency-domain equalization techniques have also been studied for single-carrier modulation schemes to reduce the computational complexity [125, 44, 92, 67].

2.7 MIMO techniques

MIMO techniques are widely employed in wireless communications to improve link reliability and/or increase the data rate. It is natural to extend MIMO to VLC as light fixtures are typically made of multiple LEDs to provide sufficient illumination in the room. Furthermore, several PDs can easily be implemented at the receiver side in a compact portable device thanks to their small size. We will firstly describe the MIMO system model in VLC. Then, we will detail three common MIMO techniques in VLC, namely repetition

coding (RC), SMP and SM. Finally, we will outline the merits and flaws of these MIMO techniques.

2.7.1 Principle of RC

RC is a straightforward implementation of MIMO where all LEDs are active concurrently and transmit the same signal simultaneously. The spectral efficiency is not further enhanced compared to a SISO configuration and is equal to $\log_2(M)$, where M is the constellation order of the transmitted signal. However, RC benefits from spatial diversity, and thus improves the robustness of the communication link. The intensities add up constructively at the receiver. Each PD receives a copy of the transmitted signal with a variable strength depending on the location of the receiver. Thus, the received signals are combined with a maximum ratio combiner (MRC) to exploit spatial diversity. In MRC, each received signal is weighted accordingly to the received SNR. As a result, the MRC output SNR is maximized and is equal to the sum of SNRs on each receiver branch. The mechanism of RC at the transmitter and receiver side is presented in Fig. 2.9.

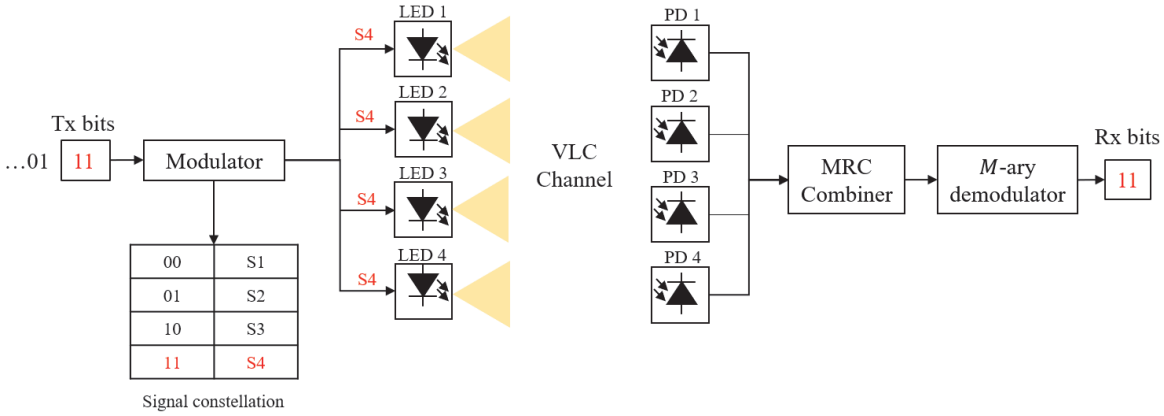

Figure 2.9 Principle of RC in a 4x4 MIMO system with a signal constellation of modulation order 4.

2.7.2 Principle of SMP

In SMP, all LEDs are active during a symbol duration and transmit independent data streams simultaneously. The principle of SMP is shown in Fig. 2.10. When a M-ary signal is transmitted, the spectral efficiency is increased compared to RC, and is equal to $N_t \log_2(M)$ bit/s/Hz, N_t being the number of LEDs. SMP does not exploit spatial diversity but exhibits a multiplexing gain that linearly grows with the number of transmit LEDs. One drawback of the technique is the complex receiver, which must perform demultiplexing to recover the data streams prior to demodulation.

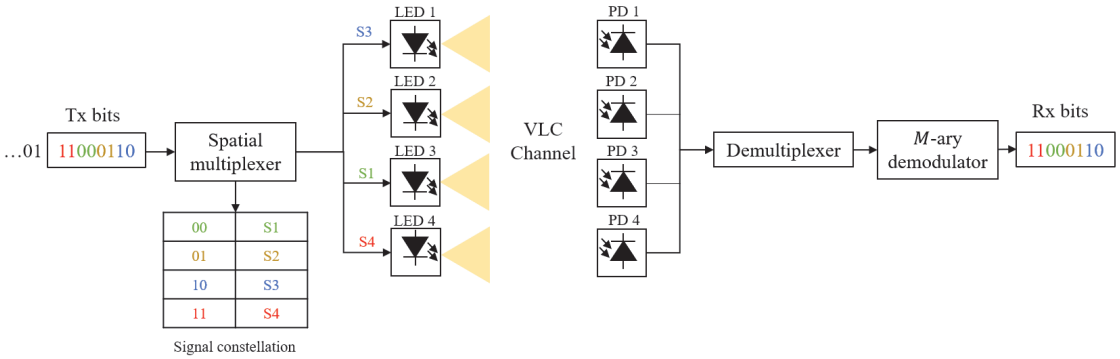

Figure 2.10 Principle of SMP in a 4x4 MIMO system with signal constellation of modulation order 4.

2.7.3 Principle of SM

Among the MIMO techniques, SM was originally developed for RF communication systems [89] and later adapted to VLC and renamed "optical spatial modulation (OSM)" [88]. Note, both terms can be found in the literature for VLC, referring to the same technique. For convenience, "SM" is used herein instead of "OSM". SM is a low-complexity modulation scheme based on the encoding of bits in the spatial domain in addition to the conventional signal constellation domain. In wireless communications, there are two possible implementations of SM. The first one is transmit SM, which considers the index of the transmitter to convey additional information. At the receiver side, the detector must estimate the index of the active transmitter. The second type of SM is receive SM which considers the index of the receive antenna. The latter is selected by means of spatial focusing techniques and the detector must estimate the index of the targeted receive antenna. In VLC, only the first form of SM, namely transmit SM is implemented. This is because VLC implemented with IM/DD is by nature noncoherent and power-based, thus making simple RF beamforming techniques (based on phase relationships between signals) impractical.

The principle of SM is detailed in Fig. 2.11. Within a symbol duration, a single transmit LED is selected and activated while the other transmit LEDs are turned off. The advantage of SM lies in its simple implementation at both the transmitter and the receiver. Moreover, ICI is mitigated as only one transmit LED is active among the total N_t LEDs. Therefore, the first $\log_2(N_t)$ incoming bits are mapped to a spatial symbol which corresponds to the index of the LED that will be active, and the next $\log_2(M)$ are mapped to a symbol in the M-ary signal constellation. Therefore, the spectral efficiency is improved by sending additional bits in the spatial domain and is equal to $\log_2(N_t) + \log_2(M)$ bit/s/Hz. At the receiver side, the SM receiver must detect which LED has conveyed the information

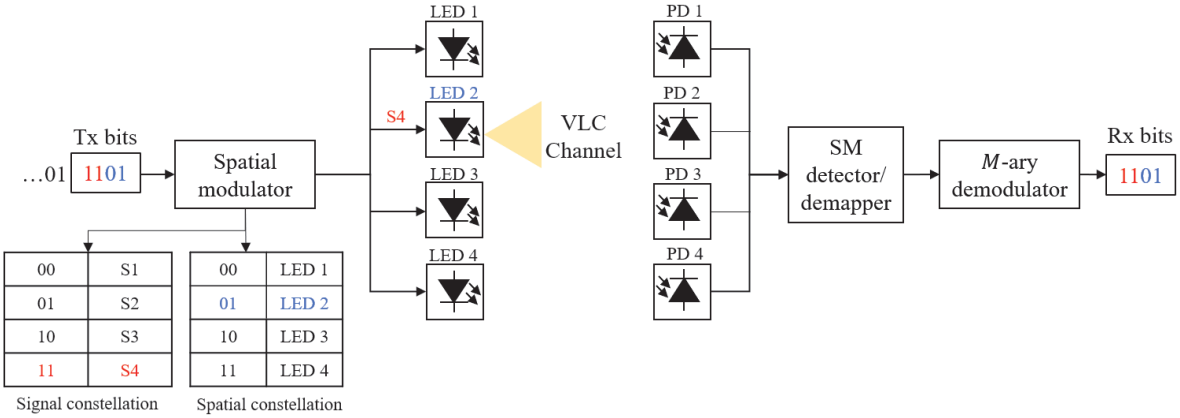

Figure 2.11 Principle of SM in a 4x4 MIMO system with a signal constellation of modulation order 4.

to recover the spatial information and then demodulate the signal. There are numerous extensions and specific cases of SM that are listed below and in Table 2.5.

Space shift keying (SSK)

SSK is the simplest form of SM considering only the index of the LED to transmit data [88, 87, 36]. In other words, no M-ary signal is transmitted and the incoming bits are encoded solely in the spatial domain. Consequently, only a spatial symbol is conveyed and the spectral efficiency is equal to $\log_2(N_t)$ bit/s/Hz. The LED that is selected by the spatial symbol simply transmits a pulse through the wireless optical channel. A proof-of-concept was reported in [120].

Generalized spatial modulation (GSM)

GSM is a generalization of SM where multiple LEDs can be activated concurrently [6, 106]. The number of active LEDs in a symbol duration is denoted N_a where $1 < N_a \leq N_t$. The spatial symbol selects N_a active LEDs among the N_t available LEDs while the remaining LEDs are idle. The N_a activated LEDs transmit the same M-ary signal. Therefore the spectral efficiency is $\log_2 \binom{N_t}{N_a} + \log_2(M)$ bit/s/Hz.

Generalized space shift keying (GSSK)

GSSK is a generalization of SSK as more than one LED can be activated at the same time in a symbol duration. GSSK can be implemented with a fixed number of active LEDs N_a and can therefore be considered a specific case of GSM where $M = 1$. However, in the literature GSSK is usually implemented with a varying number of active LEDs N_a with $1 < N_a \leq N_t$. [96, 15, 97, 98]. More specifically, in the latter implementation, the number and positions of ones in the incoming bits stream determine the number of active LEDs N_a and the LED index, respectively.

Optical spatial modulation OFDM (OSM-OFDM)

In SM, since one spatial symbol is sent within the time of a symbol interval and given that the symbol duration in OFDM is significantly longer than in single-carrier modulation schemes, combining SM and OFDM does not seem relevant at first. However, alternatives similar to conventional SM as described above have been developed. The most common one is referred as OSM-OFDM, which maps spatial bits to subcarriers [54, 142]. When a subcarrier is assigned by a spatial symbol to a LED index, it is disabled for the other LEDs, resulting in a loss of spectral efficiency. In this scheme, all LEDs are active concurrently. It is also worth mentioning that OFDM requires an IFFT and fast Fourier transform (FFT) operation at the transmitter and receiver, respectively, which compromises the advantage of simple implementation of SM-aided systems.

LED index modulation (LIM) is another MIMO technique based on OFDM to improve the spectral efficiency [131]. Index modulation refers to "the family of communication systems that consider other transmit entities than amplitudes/frequency/phases to convey information" as stated in [12]. SM can be seen as a special case of IM since it considers the index of the transmit LED to convey additional information. Unlike SM, LIM does not employ a spatial constellation, but uses multiple transmit LEDs to transmit different parts of the signal (polarity, real and imaginary parts) and to achieve better energy and spectral efficiency.

Extensions of SM and other LED modulations schemes are reported in Table. 2.5.

2.7.4 State of the art on the experimental demonstrations in VLC

Experimental investigations have been carried out in the literature to evaluate the performance of VLC in practice. In Table 2.6 are listed relevant recent experiments performed by various research groups in SISO and MIMO configurations. From that table, the following observations can be made:

1. DMT with bit loading is often selected as the "default" modulation scheme in VLC.
2. A significant share of these studies focused on achieving high-speed transmission with costly optical front-end components, such as micro-LEDs or LDs at the transmitter, which exhibit a large 3-dB bandwidth, and / or with highly-sensitive APDs at the receiver. In addition, transmissions of several Gbps are reported by employing RGB LEDs in conjunction with the WDM technique which allows the multiplexing of three independent data streams. Finally, many studies employed complex optical equipments such as dichroic mirrors, multiple lenses or highly selective color filters.

Table 2.5 Extensions of SM and LED index modulations.

Ref.	Name	Design features	Advantage	Disadvantage
[5]	**S-CAP**	Combination of SM and CAP.	Low-complexity at TX/RX.	DC bias addition required. High sensitivy to timing jitter in practice.
[93]	**GSPPM**	Combination of GSSK and PPM.	Enhanced spectral efficiency. Better energy efficiency than SSK and GSSK.	The pulse inversion technique at the TX requires a DC bias addition.
[106]	**MS-SM**	Combination of SM and SMP. N_a out of N_t selected LEDs transmit independent data streams simultaneously.	Enhanced spectral efficiency compared to GSM. More suited for illumination than SM.	Sensitivity to channel correlation. Complex receiver.
[132, 116]	**TD-SM**	Based on OFDM. Time-domain samples after IFFT operation are assigned to 1 out of N_t LEDs determined by a spatial symbol. DC bias addition and zero clipping operation.	Higher spectral efficiency and better BER performance compared to conventional OSM-OFDM due to time-domain spatial mapping and reduced ICI.	Large DC bias required. Hermitian symmetry operation. Complex receiver. A single LED is active in a symbol duration: not suited for lighting functions.
[131]	**GLIM-OFDM**	Based on 4 transmit LEDs and OFDM. Real and imaginary parts separation. Sign information encoding in LED indexes.	High spectral and power efficiency No DC bias required. No Hermitian symmetry operation.	2 out of 4 LEDs are active in a symbol duration. Complex receiver. Not well suited for illumination.
[133]	**NDC-OFDM**	Based on 2 LEDs and OFDM. 1 LED transmits the positive samples, while the other LED sends the absolute values of negative samples.	No DC bias required. High power efficiency. Improved spectral efficiency compared to OSM-OFDM. Robust against ICI.	Hermitian symmetry operation. 1 out of 2 LEDs is active in a symbol duration. Complex receiver. Not well suited for illumination.

3. The illumination level at the receiver is not consistently considered as the most relevant parameter. Although some studies report a luminance of more than 1000 lx, this illumination level is only recommended for specific tasks which require high precision (precision mechanics, color inspection, metal engraving etc...), as discussed in Section 2.4.2. A high level of brightness leads to more received optical power at the receiver, hence a higher SNR and better system performance. In contrast, a regular luminance for normal office work is 500 lx.

Table 2.6 Experimental VLC setups in SISO and MIMO configurations

Ref.	Year	Data rate	LED	PD	Distance	Modulation	Illumination
[121]	2010	513 Mbps	White	APD	0.3 m	DMT	1000 lx
[66]	2012	1 Gbps	White	APD	0.1 m	DMT	420 lx
[70]	2012	1.25 Gbps	RGB	APD	0.1 m	DMT	1000 lx
[126]	2013	3.22 Gbps	RGB	PIN	0.25 m	CAP	-
[28]	2014	400 Mbps	RGB	PIN	2 m	DMT	500 lx
[29]	2014	5.6 Gbps	RGBY	APD	1.5 m	DMT	720 lx
[18]	2014	50 Mbps	White	PIN	2m	OOK (MIMO 4x4)	350 lx
[112]	2015	1.1 Gbps	White	PIN	0.16 m	PAM	2000 lx
[54]	2015	1.34 Gbps	μLED	APD	1 m	OSM-OFDM (MIMO 2x2)	-
[134]	2015	8 Gbps	RGBY	PIN	1 m	CAP	451 lx
[53]	2016	1 Gbps	White	PIN	1 m	DMT (MIMO 3x3)	-
[26]	2016	10.4 Gbps	micro-LED	PIN	1.5 m	DMT	984 lx
[81]	2017	6.36 Gbps	RGB	PIN	1 m	DMT (MIMO 2x2)	-
[123]	2018	249 Mbps	White	PIN	1 m	Multi-band CAP (MIMO 4x4)	545 lx
[13]	2018	10.2 Gbps	RGB	PIN	-	DMT	-
[14]	2019	15.73 Gbps	RGB	PIN	1.6 m	DMT	-

2.8 Chapter summary

In this chapter, we presented the fundamental concepts of VLC. We reviewed the existing optical front-end technologies and we highlighted the pros and cons of each. Since the cost of implementation and the compatibility with the lighting function are key features in this research work, a commercially-available white LED typically used for indoor illumination and a low-cost silicon PIN PD will be employed.

Furthermore, we introduced the indoor illumination requirements, which will be taken into account in the following studies.

The characteristics of the optical wireless channel were also described. We have shown that the amount of power provided by the multiple reflections in indoor VLC is negligible when a direct path between the transmitter and the receiver exists. Therefore, the VLC systems will be investigated in a LOS configuration and the impact of the multiple reflections on walls, floor, obstacles or humans will be neglected.

We also introduced some of the major challenges faced in VLC, such as the bandwidth limitation and the nonlinearity of the LED. In order to deal with this limitation, we will investigate spectrally-efficient digital modulation schemes such as PAM, CAP, DMT and MIMO techniques. Regarding the LED nonlinearity, we will employ compensation techniques to improve system performance.

In the next chapter, we will thoroughly describe the CAP modulation scheme, and we will carry out an experiment to show the potential of CAP as a strong candidate for high-speed VLC transmissions.

CHAPTER 3

Study of a VLC link under illumination constraints with CAP modulation

3.1 Introduction

Two approaches are generally considered for VLC transmission using bandlimited front-end components. In the first one, the signal is narrowband and is modulated using single-band modulation schemes such as CAP or PAM. In this case, the channel is non-frequency-selective and no equalization is required. The throughput is, however, very low. In the second approach, the information signal is wideband and multi-band modulation schemes such as multi-band CAP or DMT-based techniques are employed in combination with adaptive bit-loading while avoiding complex equalization. Another classical approach, less extensively used for VLC, consists in extending the signal bandwidth as much as possible and using equalization to cope with the channel frequency selectivity. This is the method employed in this chapter and in Chapter 5. Given that the transmitted signal spectrum is not bounded by neighboring channels, the modulation bandwidth in VLC is a parameter that can be freely optimized without being constrained by overlapping spectra, as opposed to RF systems where the electromagnetic spectrum is strictly regulated.

Moreover, the signal PAPR has a great impact on VLC transmission due to the constraint of limited LED dynamic range. A low signal PAPR is preferred to maximize the occupation of the LED dynamic range, and therefore maximize the transmit power. Multi-band techniques are known to exhibit a high PAPR and this is why single-band modulation formats are usually preferred. Among the different modulation schemes used for VLC, many reasearch studies deal with single-band CAP modulation. This spectrally-efficient modulation technique is particularly suitable for VLC systems because of its low PAPR and simple transceiver structures compared to multi-band techniques (e.g. DMT, multi-band CAP).

In the literature, only a few experimental works have been carried out for VLC transmission based on CAP modulation. The authors of [129] used a red-green-blue-yellow LED model and the WDM technique to reach an aggregate data rate of 8 Gbps at a BER below 3.8×10^{-3}. A RGB LED is used in [126], allowing a transmission rate of 3.22 Gbps. In

addition, a data rate of 1.1 Gbps is reported in [127], using a white LED and a blue filter in front of the photodiode to increase the modulation bandwidth. However, none of those experimental studies took any illumination requirements into account.

Therefore, the aim of this chapter is two-fold: 1) to propose an experimental setup carrying out a VLC transmission with low-cost components; 2) to optimize the data rate while maintaining standard illumination levels. For this purpose, we concentrate our study on the implementation of single-band CAP modulation with low-cost components and low complexity at both the transmit and receive sides, while complying with illumination constraints.

The chapter is organized as follows: we firstly introduce the principle of CAP modulation with a description of each function to be carried out at both the transmitter and the receiver sides in Section 3.2. Then, in Section 3.3 the indoor lighting requirements recommended by standardization bodies and the properties of the white LED are introduced. The experimental setup is detailed, as well as the measurement method in Section 3.4. In Section 3.4.3 the channel estimation method with PN sequence is presented. Then, experimental and simulation results are analyzed and compared in Section 3.5. Finally, Section 3.6, concludes the chapter.

3.2 CAP modulation scheme

3.2.1 Principle of CAP

CAP modulation was historically developed for communication over copper wires [55] and has drawn a lot of interest recently for its potential as a suitable modulation for VLC due to its special properties. The implementation of CAP in IM/DD VLC systems is simple, as a pair of FIR filters is used to transmit an in-phase and a quadrature component in an orthogonal fashion [3]. An interesting property of CAP is that the baseband signal spectrum is shifted upwards (as with a carrier) but the amount of shift f_c is low and is such that the resulting spectrum remains in the baseband domain, i.e. the lower sideband extends near or at $f = 0$. The frequency upconversion is implicit as part of the pulse shaping filtering operation, thus obviating the mixing with a carrier produced by a local oscillator, hence the term "carrierless". The absence of spectral components near DC in the CAP signal can be an advantage for VLC channels since the received signal is high-passed filtered to remove the DC component as well as any contribution from ambient light.

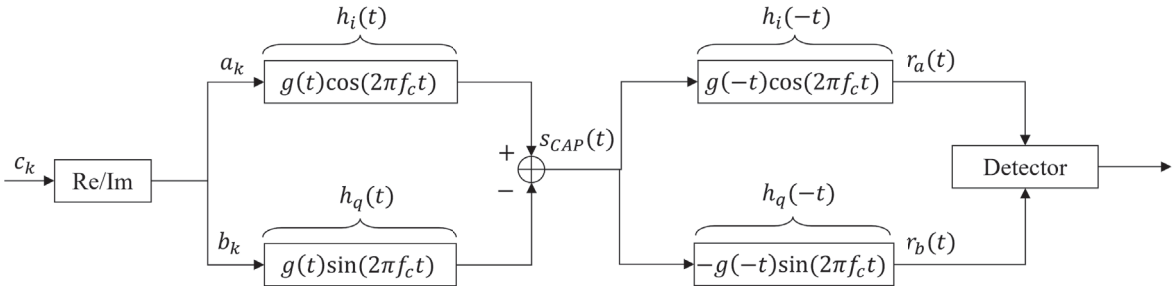

Figure 3.1 transceiver for a distortionless channel and a SRRC pulse shaping filter $g(t)$.

The CAP signaling scheme for a distortionless channel is illustrated in Fig. 3.1. First, the incoming bits are modulated into complex QAM symbols c_k. Then, the real and imaginary parts a_k and b_k are separated and convolved with the filters $h_i(t)$ and $h_q(t)$, respectively, which are obtained by multiplying a cosine and a sine of frequency f_c with a square-root raised cosine (SRRC) $g(t)$ such that

$$h_i(t) = g(t)\cos(2\pi f_c t), \tag{3.1}$$

and

$$h_q(t) = g(t)\sin(2\pi f_c t). \tag{3.2}$$

The center frequency of the CAP signal spectrum is therefore denoted f_c. In order to avoid any aliasing, f_c must be equal or greater than the maximum frequency of $g(t)$. Furthermore, it is desirable to maximize occupancy of the LED 3-dB modulation bandwidth, leading us to define f_c as being equal to the said maximum frequency, i.e.

$$f_c = \frac{(1+\alpha)}{2T}. \tag{3.3}$$

where α is the roll-off factor parameter denoting the excess bandwidth. The filter outputs are then subtracted, yielding the CAP signal $s_{CAP}(t)$ defined as

$$\begin{aligned} s_{CAP}(t) &= \sum_{k=-\infty}^{+\infty} a_k h_i(t-kT) - b_k h_q(t-kT) \\ &= \sum_{k} a_k g(t-kT)\cos(2\pi f_c(t-kT)) - b_k g(t-kT)\sin(2\pi f_c(t-kT)), \end{aligned} \tag{3.4}$$

which can also be further written as

$$s_{CAP}(t) = \mathrm{Re}\Big\{ \sum_k c_k g(t - kT) \exp\left(-j2\pi f_c(t - kT)\right) \Big\} \tag{3.5}$$

At the receiver, each stream is reconstructed by means of matched filtering where the receive filters $h_i(-t)$ and $h_q(-t)$ are matched to the respective transmit filters, i.e, their impulse responses are time-inverted versions of the latter.

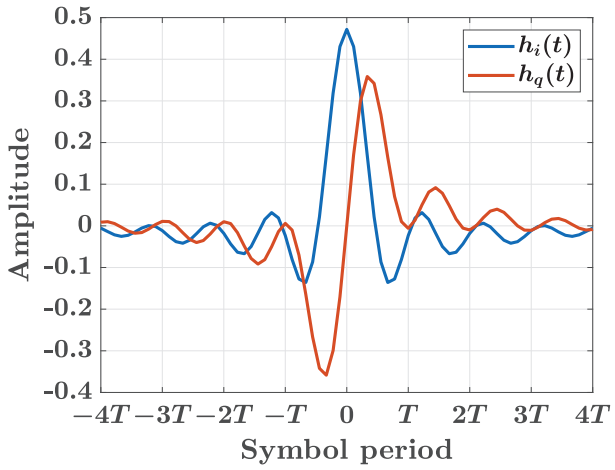

(a)

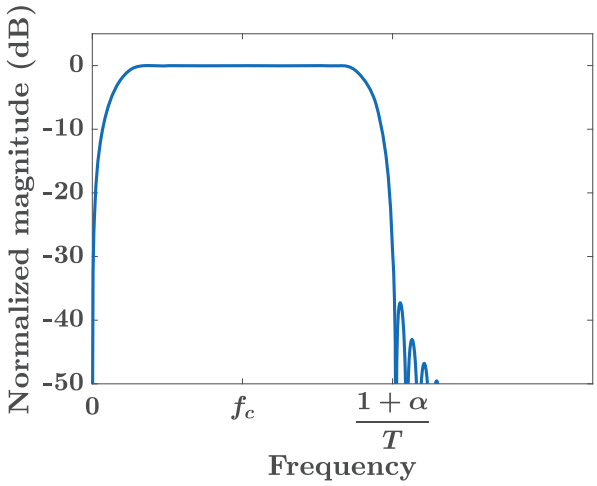

(b)

Figure 3.2 (a) Impulse response of transmit filters $h_i(t)$ and $h_q(t)$ and (b) spectrum of the CAP signal.

3.2.2 Comparison with QAM architecture

Let us now compare the CAP transceiver structure with that of well-known QAM, which share similarities. In fact, there is a fine difference between the two modulation schemes with respect to the implementation of the modulator: as described in Fig. 3.3. The QAM modulator relies on a local oscillator at the transmitter whereas CAP relies instead on a pair of orthogonal pulse shaping filters. Moreover, the transmitted signal in QAM can be expressed as

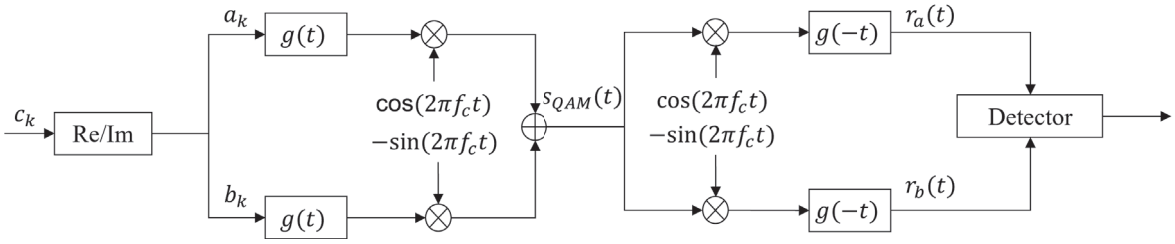

Figure 3.3 QAM transceiver for a distortionless channel and a SRRC pulse shaping filter $g(t)$.

$$s_{QAM}(t) = \mathrm{Re}\Big\{ \sum_k c_k[k] g(t - kT) \exp\left(-j2\pi f_c t\right) \Big\}. \tag{3.6}$$

The only mathematical difference between (3.5) and (3.6) lies in the addition of the multiplier $\exp(-j2\pi f_c kT)$ in (3.5) which corresponds to a phase shift of $2\pi kT$ in the time domain. In other words, in CAP the phase of the carrier is reinitialized for every subsequent transmitted symbol, as opposed to QAM where the symbols are continuously modulated by the carrier. This is due to the specific implementation of CAP, where the modulator is integrated in the pulse shaping filter, the latter having a fixed number of coefficients. It should also be understood that the use of FIR filters instead of local oscillators to implement twin quadrature rails is made practical by virtue of the fact that the effective carrier frequency f_c in CAP is very low with respect to the signal bandwidth.

The mathematical expressions of demodulated signals in QAM are presented in Appendix A. At the receiver side in QAM, the received signal is first multiplied by a carrier and then low-pass filtered by the matched filter $g(-t)$. This is equivalent to shifting the passband modulated signal back to baseband. In addition, the desired part is conserved, while the interference part stemming from the quadrature branch is negligible. As a result, QAM modulation is very robust against timing jitter. On the other hand, CAP performs the demodulation process in a single operation, namely matched filtering. Consequently, the interference component is not negligible between sampling times (i.e. when $t \neq kT$) and

the receiver is very sensitive to non-ideal sampling instants, which can occur for instance when the receiver clock does not exactly match that of the transmitter. Therefore, the very high sensitivity of CAP to timing jitter results in a rotation effect of the received constellation and can severely degrade the system performance [4]. In order to mitigate the effects of timing jitter in a practical bandlimited VLC system, one can employ a fractionally-spaced equalizer (FSE) as in [2]. The FSE was first introduced in [42] and consists in a simple FIR with input samples that are upsampled at a rate of K'/T, T being the symbol period. This type of FIR filter outputs a filtered signal with the same rate as the input. However, this filtered signal is then down-sampled by a factor of K' in order to get the output signal at the symbol rate. This output signal is then fed to a decision device in order to make decisions on the symbols. The key characteristic of the FSE is that at least two samples are taken per symbol at the input of the equalizer, thus relaxing the constraint on the sampling clock to be strictly adjusted.

Given that most VLC systems are non-coherent and employ IM/DD, CAP modulation is largely more used compared to QAM transceivers with the architecture described in 3.2.2 which requires the system to be coherent.

3.3 Illumination constraints and LED characteristics

3.3.1 White LED properties

A commercially available white LED was selected for this study (Lumiled LUXEON 3020), with a color temperature of 3000 K. The low-pass frequency response of the LED was measured using a network analyzer and provides a 3-dB bandwidth of 1.47 MHz. A blue filter can be used to suppress the slow phosphor response and reduce the contribution of parasitic lights. However, this comes at the cost of a significant decrease in signal power, as our measurements have shown. A decrease in electrical power of 26 dB was observed with a commercially-available blue filter with a central wavelength of 450 nm, a 25 nm bandwidth, and transmittance close to 1. Note, a blue filter with a central wavelength better adjusted with respect to the maximum relative power of the blue component could be selected. However, according to the component datasheet, this would lead to a only 20 % improvement in received optical power. Such a filter was therefore not implemented in the experimental setup. The LED outputs a luminous flux of 53 lm when the bias current is set to 120 mA, which is the figure recommended by the manufacturer. Moreover, the semi-angle at half luminance $\theta_{\frac{1}{2}}$ is equal to 55°.

3.3.2 Indoor lighting requirements

In Section 2.4, the concept of horizontal luminance was introduced, which is an important metric to assess the illumination distribution in space of a LED-based luminaire. According to European norm EN 12464-1 for the lighting of indoor work places, a horizontal luminance of 500 lx must be ensured at the user level to read and write in a typical office room [17]. In such a scenario, a luminaire made of multiple LEDs would be employed to achieve the desired illumination level, since a single mid-power LED provides a limited luminous flux.

In addition, in an office room, a distance of 2.25 m typically separates a desk or a workstation from the ceiling. Therefore, when the desk is placed right below the roof-mounted luminaire in the center of the room (i.e., $\theta = \phi = 0$), the luminous flux required to achieve 500 lx at the user level is 7078 lm using (2.5). Therefore, 134 LEDs of the selected type would be required to achieve the desired illumination level. It is assumed that all LEDs in the luminaire are located at the same point for the sake of simplicity. The horizontal luminance on the receiver plane in a typical room of size $5 \times 5 \times 3$ m^3 is illustrated in Fig. 3.4.

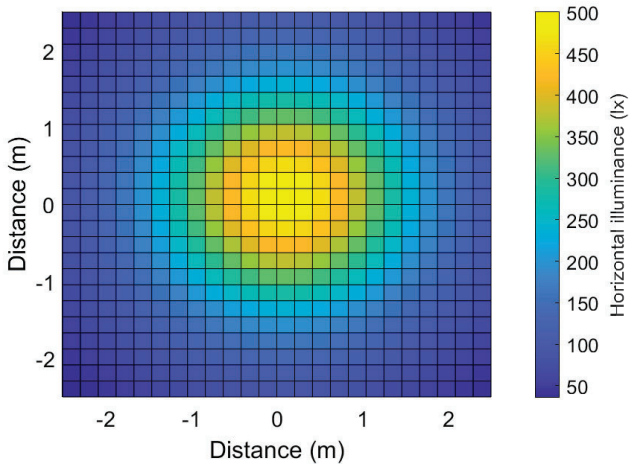

Figure 3.4 Horizontal illuminance on the receiver plane (top view) at a distance of 2.25 m from the ceiling

As depicted in Fig. 3.6, light fixtures employed for indoor illumination typically comprise multiple mid-power LEDs (such as the one we selected in this study) instead of a single high-power LED in order to facilitate heat dissipation and improve electro-optical conversion efficiency. If a diffuser is used in the luminaire as shown in Fig. 3.6, the distribution of luminance will be more homogeneous and the number of LEDs must be increased to obtain a luminance of 500 lx at the receiver location. However, in order to reduce the

size and complexity of the experimental setup, we use a single LED while still ensuring the desired level of illumination at the receiver side. Using (2.5), horizontal luminance is plotted against distance in Fig. 3.5. It can be observed that the requirement of 500 lx using a single LED is fulfilled when the link length is set to 20 cm. Note that the bandwidth limitation and nonlinear behavior of the VLC system are taken into account, and the results of this study can naturally be extended to an implementation scenario in a typical office room using a luminaire with a larger number of similar LEDs.

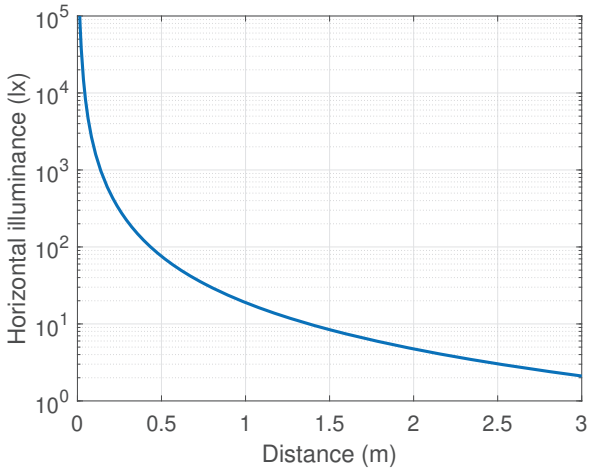

Figure 3.5 Horizontal illuminance for one LUXEON 3020 LED with respect to distance

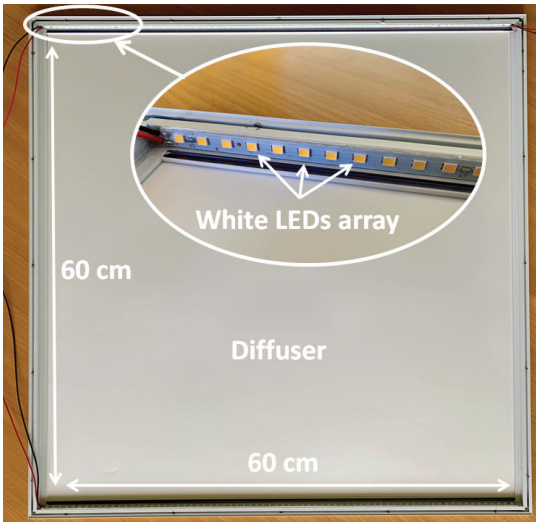

Figure 3.6 Typical LED light fixture used for indoor illumination (Sylvania START Panel Flat UGR19 600x600 Neutral White) consisting of 144 total mid-power LEDs and providing a luminous flux of 3500 lm.

3.4 Test bench presentation

3.4.1 Experimental setup

The diagram and a picture of the experimental setup are shown in Fig. 3.7 (a) and (b) respectively. The transmission steps are detailed below:

1. The CAP is generated offline using MATLAB. First, the incoming bits are modulated into QAM symbols. Then, the real and imaginary parts are separated, upsampled by a factor K and convolved with the in-phase and quadrature filters, respectively. The filter outputs are then subtracted. The oversampling factor K is chosen equal to 10 and the filter length is set to a length of 20 symbol periods to ensure the absence of ISI at sampling instants.
2. The CAP signal samples are then fed into the arbitrary waveform generator (AWG) (Tektronix, AWG 7052, 10 bits resolution) which operates at a sample rate $f_{awg} = K \times D_s$. The AWG output signal then modulates the LED light intensity using a custom board we designed for interfacing the LED and providing both the DC bias and the wideband modulating current.
3. The transmission is performed in a dark room to minimize the impact of ambient light. After transmission through the visible light channel, a 16-mm diameter lens concentrates the signal onto a low-cost silicon PIN (S-PIN) PD (OSRAM SFH-2400) with a 1 mm^2 active area.
4. A trans-impedance amplifier is used to convert the photocurrent into a voltage signal which is then sampled by a real-time oscilloscope (LeCroy 64 MXs-A) and saved for subsequent offline processing. The received signal is first resampled, and then passed through the matched filters. In this study, the outputs of the matched filters are downsampled by a factor of $K' = K/2$ and then recombined to obtain complex QAM symbols prior to equalization. The equalizer is a FSE-FFE operating at a rate of 2/T to mitigate timing jitter. The least mean squares (LMS) algorithm is employed to adapt the coefficients of the FSE-FFE [124]. The optimum coefficients are obtained after a training phase during which the first 30 000 received symbols are compared to known symbols. Lastly, QAM symbol demapping is performed to recover the transmitted bits stream.

3.4.2 Methodology

For the experiment, a 4-CAP and a 16-CAP signal are transmitted within different modulated bandwidths by setting the appropriate sampling rate of the AWG. The AWG output power is maintained at a constant level by properly using the whole dynamic range

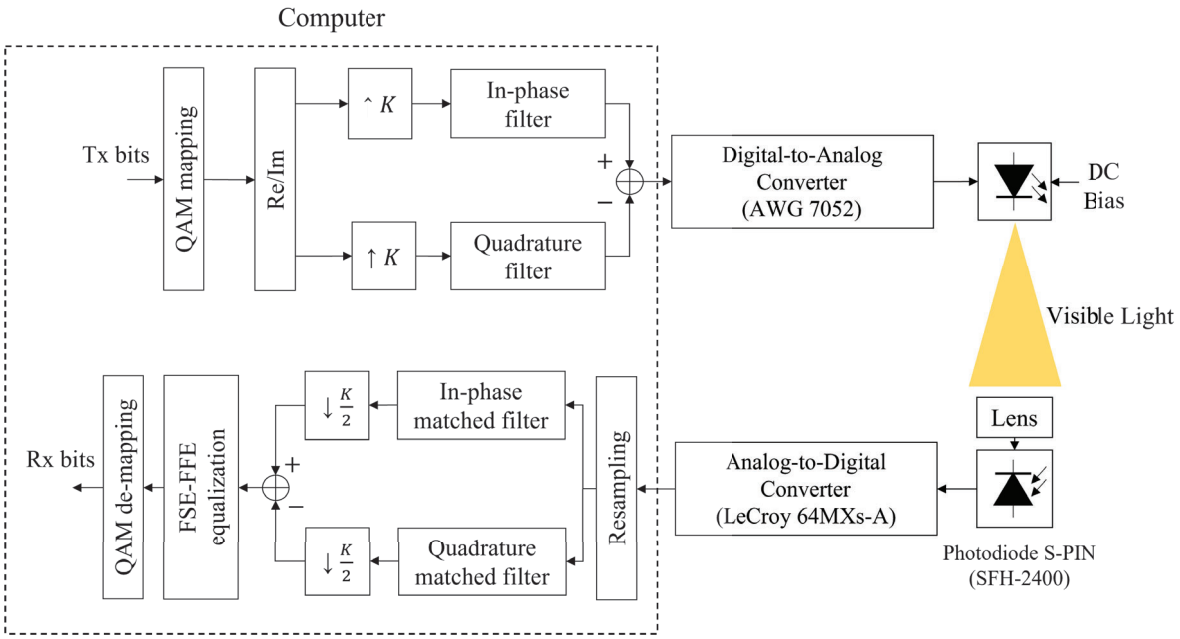

(a)

(b)

Figure 3.7 (a) Diagram and (b) picture of the VLC experimental setup.

of the LED. For example, considering a bandwidth of 45 MHz, the symbol rate D_s is $45 \div 1.2 = 37.5$ Mbaud and the required sampling rate is $f_{awg} = 10 \times 37.5 = 375$ MHz. The transmitted and received spectrum for a 16-CAP signal are presented in Fig. 3.8 (a) and (b), respectively. We can observe the bandwidth limitation effect of the LED. The larger the transmission bandwidth, the more the low-pass selectivity of the LED affects the signal and the weaker the received signal power. We determine the maximum bitrate of our system by increasing the modulated bandwidth of our signal until we reach the target BER specified as 10^{-3}, which is the forward error correction (FEC) limit. It is assumed that at a BER inferior to the FEC limit, the transmission is error-free when channel coding is used. Table 3.1 summarizes the relationship between the achieved data rates and the total occupied bandwidth, depending on the CAP modulation order.

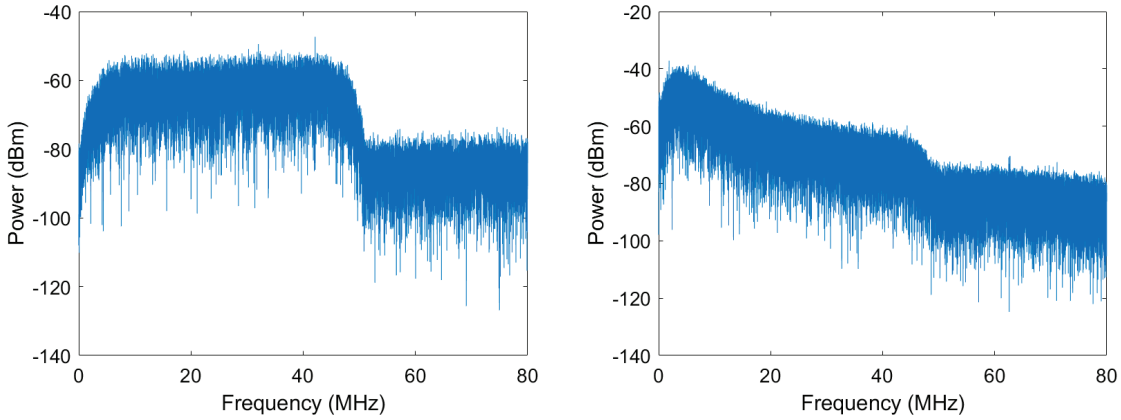

(a) (b)

Figure 3.8 Spectrum of the (a) transmitted and (b) received 16-CAP signal for a bandwidth of 51 MHz.

Table 3.1 Total bandwidth occupied by the CAP signal for various data rates

Data rate (Mbps)	140	150	160	170	180	190
Bandwidth for 4-CAP (MHz)	84	90	96	102	108	114
Bandwidth for 16-CAP (MHz)	42	45	48	51	54	57

3.4.3 Channel estimation with PN sequence

To verify our experimental VLC transmission, we developed a simulation model in which the CAP symbols are passed through a filter having coefficients based on the impulse response of the VLC channel. The CIR was obtained by performing the time domain correlation of a known and a received pseudo-noise (PN) sequence [83]. Thus, in this study, we used a binary maximum-length sequence with a length of 255 symbols to perform

channel estimation for the simulation model. This type of sequence was chosen for its very good periodic autocorrelation properties [102]. A PN sequence with a chip rate of 100 MHz (or equivalently of chip duration 10 ns) gives an estimation of the channel frequency response up to a maximum frequency of 50 MHz. The chip rate of the PN sequence has to be sufficiently large compared to the modulation bandwidth of the CAP-modulated signal. It should also be kept in mind that for the same data rate, the occupied bandwidth of 4-CAP is twice that of 16-CAP. Therefore, the clock rate of the AWG selected for 16-CAP and 4-CAP signals is 240 MHz and 408 MHz, respectively, since the obtained impulse responses have shown to exhibit a fair approximation of the system behavior in the bitrate range under study (see the results presented following Section 3.5). Note however that a more pragmatic approach based on an analytical model of the CIR will be presented in detail in Chapter 4. Following the filtering operation, the SNR was set in accordance with our measurements at the receiver side of the setup.

3.5 Numerical and experimental results

Fig. 3.9 illustrates the BER performance according to the transmission rate in simulation and in practice. We can observe that a maximum experimental bitrate of 142.4 Mbps and 184 Mbps is achieved for our setup with a BER of less than 10^{-3}, which corresponds to a modulation bandwidth of 85.44 MHz and 55.2 MHz for 4-CAP and 16-CAP, respectively. This is far beyond the 1.47 MHz 3-dB cut-off frequency of the white LED. Indeed, the use of CAP modulation enables large bandwidth operation when associated with an equalizer at the receiver side. Moreover, the BER performance of 4-CAP and 16-CAP for bitrates below 140 Mbps has been measured at less than 10^{-4}. The gap between the theoretical and experimental BER performances can be explained by the non-linearities inherent to the VLC components, which are not taken into account into simulations. Fig. 3.10 (a) and (b) represent the received 4-CAP and 16-CAP constellations after equalization. We notice slight distortions which we will investigate in a future study to further improve our VLC system.

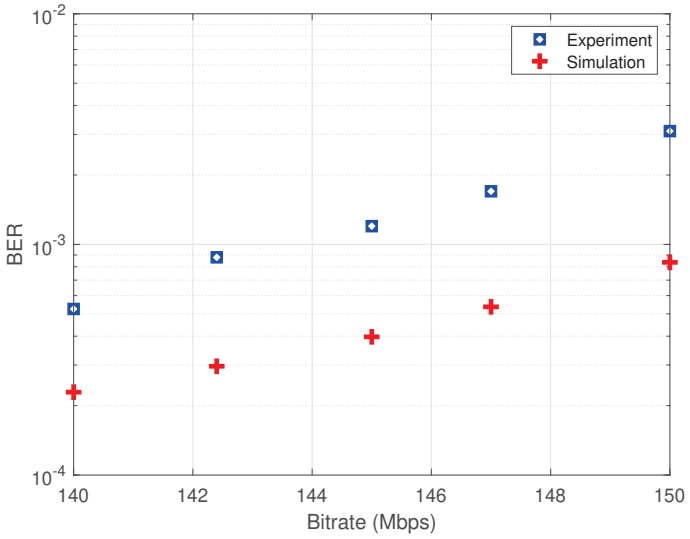

(a)

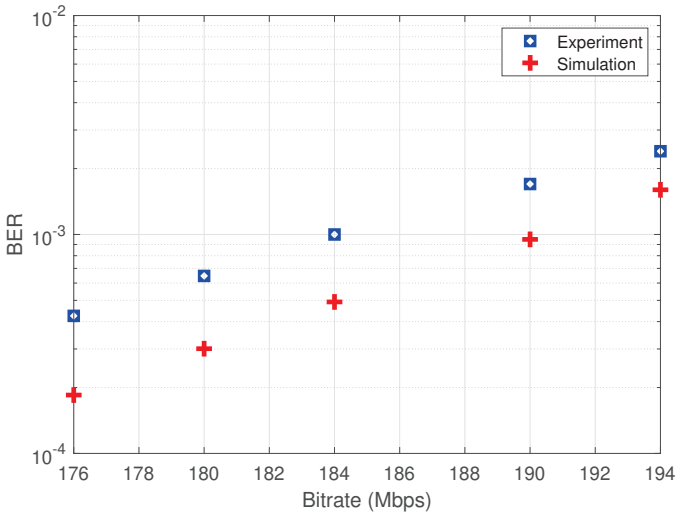

(b)

Figure 3.9 BERS of our experimental setup and simulation results for the (a) 4-CAP signal and (b) 16-CAP signal with various transmission rates.

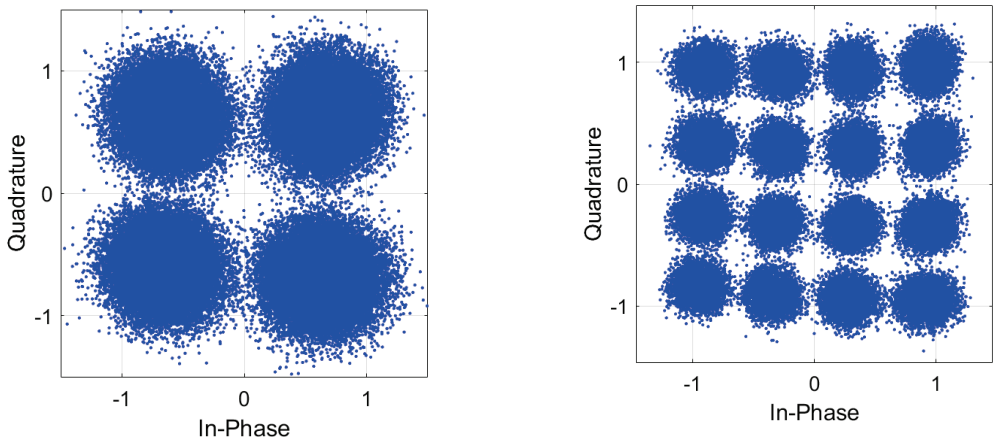

(a) (b)

Figure 3.10 (a) Received 4-CAP constellation for 142.4 Mbps and (b) received 16-CAP constellation for 184 Mbps after FFE.

3.6 Chapter summary

In this chapter, we demonstrated a low-cost VLC system compliant with the lighting requirements of a typical office room based on the CAP modulation scheme. We achieved a bitrate of 184 Mbps via a 16-CAP signal with a BER $\leq 10^{-3}$. The experiment demonstrates the potential of CAP in conjunction with equalization at the receiver to deliver high throughput on the order of a few hundred Mbps using a bandlimited white LED. These results on the optimization of the data rate with CAP under illumination constraints are the object of our published paper [73]. Furthermore, a detailed description of the implementation of CAP using MATLAB has been published as a technical article for the software company MathWorks [74].

Low-order CAP modulation such as 4-CAP or 16-CAP are classically employed in VLC. However, it is expected that the indoor lighting requirements lead to a sufficiently high SNR to enable transmission with higher modulation orders, for instance 32-CAP or 64-CAP. On the other hand, the use of higher modulation orders leads to more severe degradation caused by the nonlinear effects of the LED, which will be addressed in the next chapter. For this purpose, we will develop a simulation model taking into account non-linearity limitations with state-of-the art nonlinearity models and compensation improvements based on nonlinearity mitigation techniques.

CHAPTER 4

LED nonlinearity modeling and compensation

4.1 Introduction

In the previous chapter, we experimentally observed the impact of the LED nonlinearity on large bandwidth 16-CAP and 4-CAP signals. In fact, these nonlinear effects cannot be overlooked at high data rates. Moreover, we have forecasted that the illumination level of a typical room in normal working conditions (500 lx) could enable the use of higher modulation orders in order to increase the spectral efficiency, hence the throughput of the system. Laboratory studies have established that the impact of LED nonlinearity becomes more critical when high modulation orders are used [110]. To this extent, it becomes clear that a postdistortion or predistortion algorithm must be implemented to help mitigate the adverse effects that stem from nonlinearities in the LED. Therefore, this chapter is dedicated to the study of the impact of LED nonlinearity and its compensation. More specifically, we adopt here a systemic approach to characterize the experimental test bench presented in Chapter 3.2.

The remainder of this chapter is organized as follows: In Section 4.2, we present the simulation model structure and we propose an analytical model of the white LED frequency response to model the VLC channel. In addition, we evaluate the accuracy of the simulated transmission chain by putting an emphasis on the estimation of the received SNR. In Section 4.3, we introduce and compare the Hammerstein and Volterra series models, two nonlinearity models with memory. Then, in Section 4.4, we investigate a nonlinearity compensation technique based on the Volterra series model and we investigate its performance in simulation. Finally, Section 4.5 concludes this chapter.

4.2 VLC simulation model and assumptions

4.2.1 Link model

The simulated transmission chain employing CAP is presented in Fig. 4.1. The difference with the signaling previously described in Chapter 3 resides in the absence of downsampling operation at the output of the matched filters, and the use of a fractionally-spaced decision feedback equalizer (FSE-DFE) block, which will be detailed in Section 4.2.6. In the first instance, we focus on the modeling of the propagation channel.

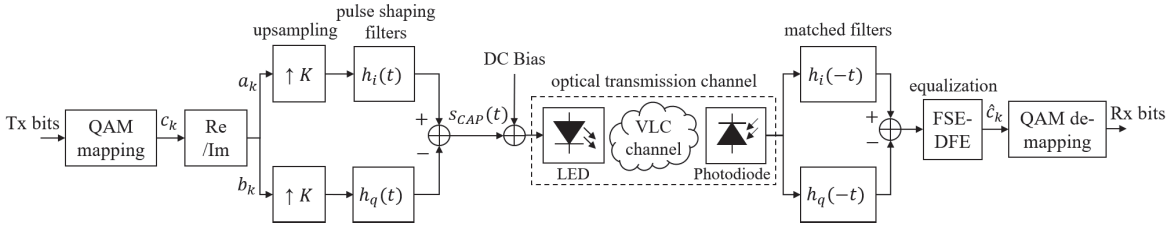

Figure 4.1 CAP modulation and demodulation scheme for a VLC system.

In a VLC link, several transfer functions are cascaded including the amplifiers characteristics, the LED response and the PD response. However, the LED is considered as the most limiting element with respect to the modulation bandwidth of the overall system. Therefore, an acceptable approximation to model the VLC channel consists in finding a simple FIR filter whose frequency response closely matches the frequency response of the white LED. Furthermore, the choice of a simulation model is a compromise between accuracy and complexity and we propose in the next Section a simple analytical expression to model the VLC channel.

The maximum system bandwidth under study is limited to 50 MHz in this work since the electronic components selected for the LED driver and the receiver, namely the amplifiers, have a limited bandwidth. In addition, the low-pass filter model of the VLC link would be inaccurate beyond this upper bound. Therefore, the received signal $y(t)$ in the simulation model can be expressed as

$$y(t) = \beta s_{CAP}(t) * h_{LED}(t) + n(t), \tag{4.1}$$

where $s_{CAP}(t)$ is the CAP modulated signal, β is a transfer DC gain between the input and output of the VLC experimental test bench and $n(t)$ is the additive noise, which is Gaussian-distributed with zero mean and is considered white over the bandwidth of interest (i.e. 50 MHz). In order to obtain an estimation of the SNR, which is a useful metric to assess the maximum system throughput, we need to determine the abovementioned elements, namely the time-domain or frequency-domain LED response, the channel transfer DC gain, and the noise power spectral density (PSD).

4.2.2 LED response analytic model

Let us recall that the white LEDs are built by depositing a phosphor layer on top of a blue LED chip. The phosphor, when excited by the blue LED light, generates the longer optical wavelengths which mix with the blue emission to form white light. In Chapter 2, we have established that the blue LED light impulse response can be approximated by

a first-order low-pass filter. Likewise, the phosphor layer is characterized by a lengthy relaxation time and thus behaves as a low-pass filter, thus severely limiting the LED's bandwidth for modulation purposes.

Therefore, the overall LED response can be modeled as the cascade of two channels: the first channel $h_b(t)$ corresponds to the blue light response, while the second channel $h_p(t)$ corresponds to the phosphor layer response. The overall LED impulse response can be written as [7, 113]

$$h_{LED}(t) = G_b h_b(t) + G_p \left(h_p(t) * h_b(t)\right), \tag{4.2}$$

where $*$ denotes the convolution operator and G_b and G_p are the power gains associated with the blue light response and the phosophor layer response, respectively. Under the assumption that most of the received optical power stems from the yellow photons [72], we have $G_p \gg G_b$ and a simplified model of the LED response can be derived from (4.2), such that

$$h_{LED}(t) = G_p \left(h_p(t) * h_b(t)\right). \tag{4.3}$$

The responses $h_b(t)$ and $h_p(t)$ can be modeled as simple first order low-pass filters [82], i.e.

$$\begin{aligned} h_b(t) &= u(t)e^{-2\pi f_b t}, \\ h_p(t) &= u(t)e^{-2\pi f_p t}, \end{aligned} \tag{4.4}$$

where f_b and f_p are the 3-dB cut-off frequencies of the blue light response and the phosphor layer response, respectively, and $u(t)$ is the unit step function.

The LED device considered here is the same as in Chapter 3, namely a low-cost white LED (Lumiled LUXEON 3020) with a color temperature of 3000 K typically used for lighting applications with a 3-dB modulation bandwidth measured at 1.47 MHz. The cut-off frequencies f_b and f_p are estimated at 12 MHz and 1.47 MHz, respectively.

The LED frequency response is obtained by taking the Fourier transform of (4.3), yielding

$$H_{LED}(f) = G_p \cdot \frac{1}{1 + j\left(\frac{f}{f_b}\right)} \cdot \frac{1}{1 + j\left(\frac{f}{f_p}\right)}. \tag{4.5}$$

It is noteworthy that G_p is set to 1 in order to normalize the frequency response ($H_{LED}(0) = 1$). The frequency response of the LED was measured with a network analyzer (HP-4195A) and compared with that of the proposed model in (4.5) in Fig. 4.2. It can be observed that the magnitude response of the proposed model fits closely with the measured one. Therefore, the former is assumed to be a reasonable approximation of the low-pass behavior of the chosen LED device in this study.

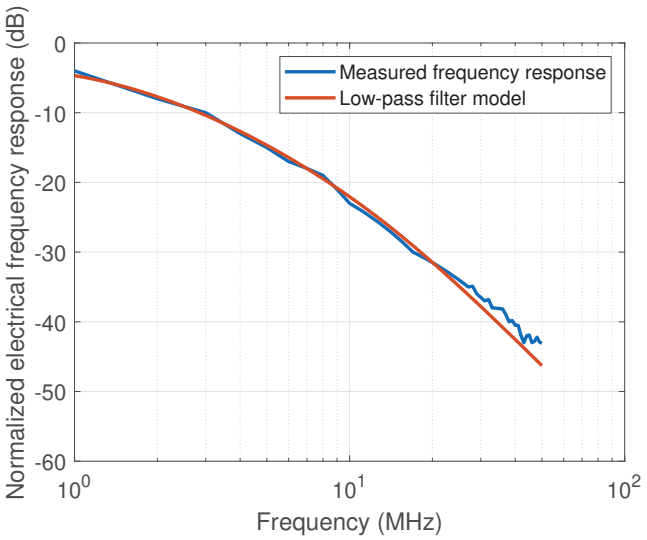

Figure 4.2 Measured LED magnitude response and proposed analytical model.

4.2.3 Channel transfer DC gain

In practice, the overall transfer function between the output of the AWG and the output of the receiver circuit has a DC gain β which can be empirically determined. The channel transfer DC gain depends on the link distance, and is therefore determined for a given illumination level. It can be measured at low frequencies within the 3-dB bandwidth of the LED (same gain as DC). To that end, a sinusoidal signal of frequency 90 KHz and of amplitude 1 Vpp is sent through the VLC system. At this frequency, the measured gain β is maximal and is equal to 2.9. With knowledge of the LED response and the determined channel transfer DC gain, the power of the information signal after transmission through the VLC channel can easily be estimated at the receiver side.

4.2.4 Noise PSD measurement

In this part, we determine an estimate of the noise PSD at the receiver output of the experimental setup. The noise one-sided PSD N_0 can be calculated as:

$$N_0 = 10 \log_{10} \left(\frac{P_{noise}}{B_{eq}} \right), \tag{4.6}$$

where P_{noise} is the noise power in Watts relative to a load of 50 Ω and B_{eq} is the noise-equivalent bandwidth over the positive frequency range. The following method is applied: first, the noise signal is sampled at a rate of 1 GHz using a real-time oscilloscope (LeCroy 64 MXs-A) and 5×10^6 samples are saved in the oscilloscope memory. During the noise signal acquisition, the LED is biased with a DC current set to 120 mA to take into account the shot noise induced by the mean emitted optical power. Next, using MATLAB, the digital signal is resampled and filtered by a low-pass SRRC filter with a noise-equivalent bandwidth of 50 MHz. The noise power P_{noise} at the output of the SRRC filter is calculated to be 1.25×10^{-7} W. Therefore, using (4.6), the noise PSD is equal to -146 dBW/Hz.

4.2.5 SNR estimation

Here, we evaluate the SNR in simulation and we compare it to the measured SNR on the experimental test bench. The SNR can be generally expressed as

$$\text{SNR} = 10\log_{10}\left(\frac{P_{signal}}{P_{noise}}\right) \tag{4.7}$$

where P_{signal} is the received signal power in Watts after matched filtering and relative to a load of 50 ohms, which can be computed as $P_{signal} = \frac{P_{rms}^2}{50}$, P_{rms} being the root mean square value of the received signal. In addition, from (4.6), we can express P_{noise} as:

$$P_{noise} = N_0 B_{eq}. \tag{4.8}$$

Let us calculate the SNR with two methods: 1) with the proposed simulation model and 2) in the experiment.

1) In simulation: The signal power P_{signal} is estimated after matched filtering while the noise power P_{noise} is computed using (4.8) and the noise PSD N_0 determined as described in 4.2.4. Moreover, in contrast to the well-known SRRC filter that has a noise-equivalent bandwidth equal by definition to $1/2T$, the noise-equivalent bandwidth of the receive matched filters in CAP is two times larger and equals $1/T$ due to the shifting of the

Table 4.1 Estimated SNR in simulation and in the experiment.

	P_{signal} (W)	P_{noise} (W)	SNR (dB)
Simulation	5.5×10^{-4}	5.6×10^{-8}	40
Experiment	3.3×10^{-4}	4.4×10^{-8}	38.75

spectrum around the frequency f_c. For instance, for a 135 Mbps 64-CAP signal, the baud rate is $1/T = 22.5$ Mbaud, and therefore the noise-equivalent bandwidth B_{eq} has the same value, i.e. 22.5 MHz.

2) In the experiment: A 135 Mbps 64-CAP probe signal is first transmitted through the VLC test bench and processed offline to determine the signal power P_{signal}. The measured signal comprises the useful signal plus the noise, the latter being however negligible with respect to the former. This measurement process is then repeated for the noise signal only (i.e. the AWG output is turned off).

The results are shown in Table 4.1. It can be seen that the estimated SNR in simulation is 1.25 dB higher compared to the SNR in the experiment. This difference in terms of SNR can be explained by several reasons. In fact, despite its simplicity, the proposed analytical channel model may not exhibit good accuracy at every frequency over the band of interest (50 MHz). In addition, the noise PSD estimation approach cannot take into account other additional sources of noise which are difficult to measure, such as the shot noise coming from the information signal itself (also referred to as signal-dependent shot noise), and the quantization noise from the ADC and DAC converters. As a result, the slight overestimation of the SNR will lead to better performance in the simulation model. Nevertheless, the proposed model has the virtue of being simple, and provides a fair approximation of the experimental VLC setup.

4.2.6 FSE-DFE equalization

FSE-DFE structure

It is well-known that adding a feedback filter to a linear equalizer yields superior performance when the error propagation is neglected [100], as it can effectively mitigate the post-cursor ISI. When the linear part of such an equalizer (or the feedforward filter) is fractionally-spaced, this type of equalizer is referred to as fractionally-spaced decision feedback equalizer (FSE-DFE) and is well described theoretically by the authors of [43], but its use is not straightforward. Thus, the following provides some details to help understand the equalization structure, which will be used in this chapter as well as in Chapter 5. As shown in Fig. 4.3, the feedforward filter of a FSE-DFE operates at rate K'/T, where T is the symbol period and K' determines how many samples there are in each symbol period T. Thereafter, we set K' to 4, which is also the chosen upsampling factor value of the signal denoted K and used throughout the system simulation (as well as in the AWG as part of the experimental testbench) to represent analog signals. It is noteworthy that the upsampling factor K is set to 4 to provide an appropriate tradeoff between performance and complexity. Therefore, the received signal is not downsampled at the input of the

equalizer since the feedforward filter operates at the same rate as the input signal. The downsampling operation takes place at the output of the feedforward filter in the equalizer. Furthermore, the downsampling is integrated into the equalization block in Fig. 4.1. The equalizer output, however, delivers equalized symbols $\hat{c}(n)$ at symbol rate $1/T$. The symbols $u(n)$ before decision can be expressed as follows:

$$u(n) = \sum_{i=0}^{M_f-1} w_i q(n + M_f - i) - \sum_{i=0}^{M_d-1} v_i \hat{c}(n + M_d - i) = \begin{bmatrix} \mathbf{w} \\ \mathbf{v} \end{bmatrix}^T \cdot \begin{bmatrix} \mathbf{q} \\ \hat{\mathbf{c}} \end{bmatrix}_{(n)} , \tag{4.9}$$

where $[.]^T$ is the transpose operator, M_f is the number of taps in the feedforward filter, M_d is the number of taps in the feedback filter, $\mathbf{w} = [w_0, w_1, \ldots, w_{M_f-1}]^T$ is the vector of feedforward filter coefficients, $\mathbf{v} = [v_0, v_1, \ldots, v_{M_d-1}]^T$ is the vector containing the feedback filter coefficients, $\mathbf{q}(n) = [q(n), q(n-1), \ldots, q(n - M_f + 1)]^T$ is the vector of input signal samples and $\hat{\mathbf{c}}(n) = [\hat{c}(n), \hat{c}(n-1), \ldots, \hat{c}(n - M_d + 1)]^T$ is the vector of reference signal samples.

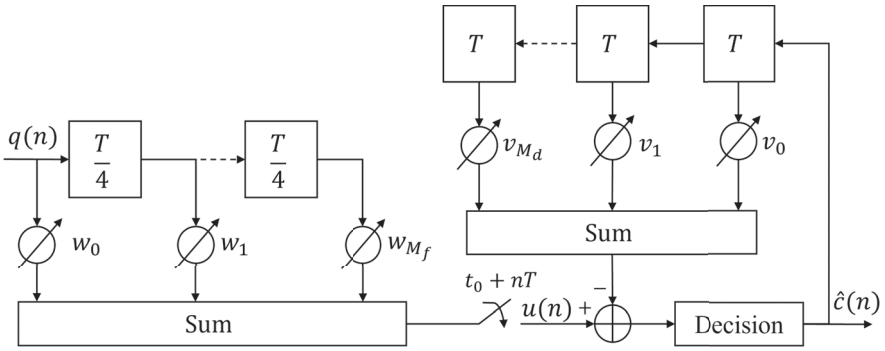

Figure 4.3 Block diagram of the FSE-DFE combining a FSE and a DFE.

Adaptation of LMS

The coefficients of the FSE-DFE can be optimized using the LMS algorithm. Based on the current set of weights at the n-th iteration, this adaptive algorithm creates the new set of weights according to

$$\begin{bmatrix} \mathbf{w} \\ \mathbf{v} \end{bmatrix}_{(n+1)} = \begin{bmatrix} \mathbf{w} \\ \mathbf{v} \end{bmatrix}_{(n)} + \mu e(n) \begin{bmatrix} \mathbf{q} \\ \hat{\mathbf{c}} \end{bmatrix}_{(n)} , \tag{4.10}$$

where the error $e(n)$ is computed as

$$e(n) = \hat{c}(n) - u(n), \tag{4.11}$$

and where μ is the step size parameter, which must be set to a value inferior to the maximum step size μ_{max} to ensure stability of the algorithm. The maximum step size is defined as [124]:

$$\mu_{max} = \frac{2}{\sigma_q^2 M_f + \sigma_{\hat{c}}^2 M_d}, \tag{4.12}$$

where σ_q^2 is the power of the input signal and $\sigma_{\hat{c}}^2$ is the power of the reference signal vector. In this study, the step size is chosen as $\mu = \frac{\mu_{max}}{3}$ to provide an appropriate tradeoff between performance and convergence speed.

4.3 Modeling the impact of LED nonlinearity

The LED electro-optical transfer characteristic relating the forward current and the output optical power is a nonlinear function as shown in Fig. 4.4 with data extracted from the datasheet of the white LED considered in this study. The nonlinear characteristics of the LED stem from the fact that the number of emitted photons is not directly proportional to the amplitude of the injected electric current in its active region. Moreover, the nonlinear transfer function $P_{opt}(I)$ of the white LED with values in mW can be fitted with a second-order polynomial function such that

$$P_{opt}(I) = -0.0014I^2 + 1.5864I + 1.0799. \tag{4.13}$$

where I is the input current in mA. Besides, the output optical power - forward voltage characteristic of the LED exhibits significantly more nonlinearity than the output luminous flux/forward current characteristic. In our study, the nonlinear distortions at the transmitter were significantly limited by employing a current source to drive the LED, instead of a voltage source.

The current-light intensity relationship of the LED also depends on the frequency of the applied signal, giving rise to a memory effect. Therefore, the nonlinearity models can be divided into two groups: memoryless and memory models. The memoryless models simply use power series such as the one in (4.13) to model the impact of LED nonlinearity.

However, this type of model is only adequate for narrowband signals. Memory models take the frequency-dependent nature of the LED into account and can be employed for large bandwidth signals. Given that the objective of this study is to investigate high-speed transmission systems, we will examine two well-known nonlinearity models with different complexity and accuracy, namely the Hammerstein model and the Volterra series model.

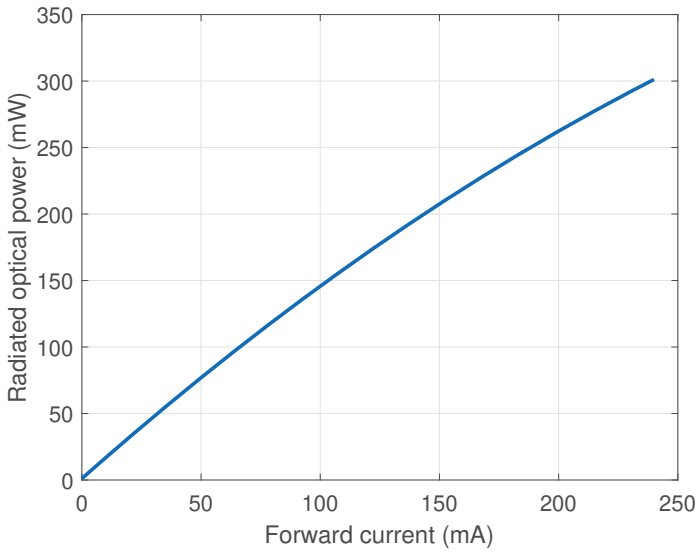

Figure 4.4 Lumiled LUXEON 3020 electro-optical static transfer function.

4.3.1 Hammerstein model

The Hammerstein model simply consists of a memoryless polynomial function followed by a linear time invariant (LTI) system that describes the LED memory effect as shown in Fig. 4.5. It can be mentioned that a variant of the Hammerstein model is the Wiener model, which differs in that the memoryless polynomial is preceded by the LTI system. Herein, the LTI system is assumed to be a first-order low-pass filter which describes the blue light response $h_b(t)$ with a cut-off frequency of 12 MHz, and the memoryless polynomial is the function presented in (4.13). Since the white LED consists of a blue light source coated with a phosphor layer, the distorted signal at the output of the Hammerstein model must be filtered by the impulse response of the phosphor layer $h_p(t)$.

4.3.2 Volterra series model

The second memory model we investigated is the Volterra model based on the Volterra series expansion. The output of the Volterra nonlinear model $p(n)$ can be expressed as [143]

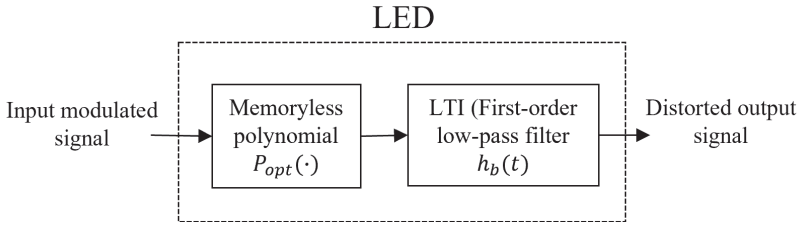

Figure 4.5 Block diagram of Hammerstein Model.

$$p(n) = \sum_{q=1}^{Q} \sum_{m_1=0}^{M_1-1} \cdots \sum_{m_k=0}^{M_k-1} h_k(m_1, \ldots, m_k) \prod_{l=1}^{q} s(n - m_l), \tag{4.14}$$

where $s(n)$ is the discrete-time input modulated signal, Q is the nonlinear order of the Volterra series expansion, M_k is the memory length at order k and $h_k(m_1, \ldots, m_k)$ is the Volterra kernel of k-th order at time delay m_k. Third-order and second-order Volterra series have been investigated by the authors of [111], and it was concluded that second-order kernels of the Volterra-series expansion lead to a fairly precise approximation of white LED nonlinear distortions. Therefore, in this study, only the terms up to the 2nd kernel order are considered and (4.14) can be further simplified such that

$$\begin{aligned} p(n) = & \sum_{m_1=0}^{M_1-1} h_1(m_1) s(n - m_1) \\ & + \sum_{m_1=0}^{M_2-1} \sum_{m_2=0}^{M_2-1} h_2(m_1, m_2) s(n - m_1) s(n - m_2). \end{aligned} \tag{4.15}$$

The Volterra series expansion includes a linear term which is nothing less than the impulse response of the channel (or that of the LED), and nonlinear terms which contain the kernel coefficients of 2nd order. The coefficients of the Volterra series are not determined in a straightforward manner. An adaptive algorithm must be employed to obtain the optimum coefficients, namely the recursive least squares (RLS) algorithm, which minimizes the least squares cost function defined as follows [144]:

$$\underset{h_k(m_1,\ldots,m_k)}{\operatorname{argmin}} \sum_{n=0}^{M_{samp}-1} \mid y(n) - p(n) \mid^2, \tag{4.16}$$

where $y(n)$ is the discrete-time received signal, $p(n)$ is the desired output of the series model and M_{samp} is the total number of samples. The principle of the RLS algorithm

is exhaustively detailed in [124] and in [100] and the block diagram of adaptive Volterra kernels estimation is depicted in Fig. 4.6. In RLS, the weights are updated as follows:

$$\mathbf{a}(n+1) = \mathbf{a}(n) + e(n)\mathbf{g}(n), \tag{4.17}$$

where $\mathbf{a}(n) = [a_0(n), a_1(n), \ldots, a_{M_1-1}(n), a_{00}(n), a_{01}(n), \ldots, a_{0M_2-1}(n), \ldots, a_{M_2-1M_2-2}(n), a_{M_2-1M_2-1}(n)]^T$ is the vector of kernel coefficients. The error $e(n)$ is calculated as

$$e(n) = y(n) - p(n) = y(n) - \mathbf{a}^T(n)\mathbf{s}(n). \tag{4.18}$$

The vector $\mathbf{s}(n)$ includes the samples of the signal at the input of the Volterra model and is written as $\mathbf{s}(n) = [s(n), s(n-1), \ldots, s(n-M_1+1), s^2(n), s(n)s(n-1), \ldots, s(n)s(n-M_2+1), \ldots, s(n-M_2)s(n-M_2+1), s^2(n-M_2+1)]^T$. Moreover, $\mathbf{g}(n)$ is the Kalman gain vector expressed as

$$\mathbf{g}(n) = \frac{\mathbf{P}(n)\mathbf{s}(n)}{\lambda_f + \mathbf{s}^T(n)\mathbf{P}(n)\mathbf{s}(n)}, \tag{4.19}$$

where $\mathbf{P}(n)$ is the current inverse correlation matrix and λ_f is the forgetting factor. The updated inverse correlation matrix for the next iteration is given by

$$\mathbf{P}(n+1) = \lambda_f^{-1}(\mathbf{P}(n) - \mathbf{g}(n)\mathbf{s}^T(n)\mathbf{P}(n)). \tag{4.20}$$

At the first iteration ($n = 0$), the inverse correlation matrix is initialized such that $\mathbf{P}(n) = I_{(M_1+M_2^2 \times M_1+M_2^2)}$, $I_{(M_1+M_2^2 \times M_1+M_2^2)}$ being the identity matrix, and the vector of kernel coefficients is set as $\mathbf{a}(n) = [1, 0, \ldots, 0]^T$.

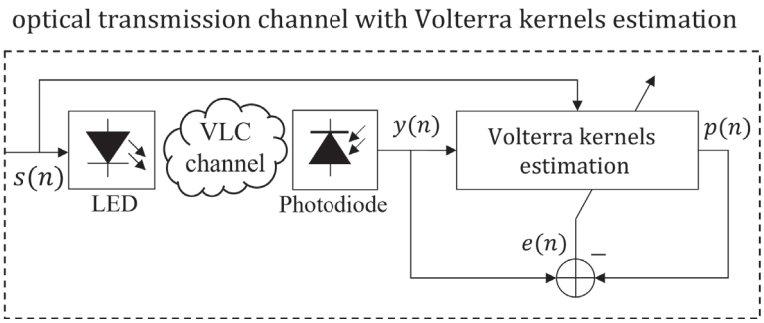

Figure 4.6 Block diagram of the Volterra kernels adaptive estimation.

4.3.3 Numerical results

The two different models we introduced are evaluated for a 64-CAP signal at a bit rate of 135 Mbps with a roll-factor of 0.15, hence a total bandwidth of 25.875 MHz. A probe signal is transmitted beforehand for the estimation of the Volterra series kernels on the test bench. The memory lengths M_1 and M_2 of the Volterra series model are set to 35 and 17, respectively, as a trade-off between performance and computational complexity. Moreover, the forgetting factor λ_f is chosen with a sufficiently small value such as 0.001.

The constellation diagrams are generated in simulation and are compared with that of the experiment (Fig. 4.7). Similar slight distortions on the top right and bottom left of the constellations can be observed. Let us introduce the concept of normalized mean-square error (NMSE) which quantifies the error between the symbols received in the experiment $\hat{s}_k$ and the symbols received in simulation s_k, which is written as

$$\mathrm{NMSE} = 10\log_{10}\left(\frac{\sum_{k=1}^{N_{symb}} |s_k - \hat{s}_k|^2}{\sum_{k=1}^{N_{symb}} |\hat{s}_k|^2}\right). \tag{4.21}$$

In the above, N_{symb} is the size of the sliding window and it is set to 100. The NMSE for the Hammerstein and Volterra model is respectively -25.2 dB and -29.6 dB. While it has the virtue of being simple, the Hammerstein model lacks accuracy for the case of large signal bandwidth. On the other hand, the Volterra model exhibits a more accurate representation of the nonlinearity impact of the LED. Moreover, the received constellation in the experiment is slightly noisier. This is explained by the difference in SNR in the simulation transmission chain as detailed in 4.2.5. Finally, this study highlights the necessity to implement a nonlinearity compensation algorithm for high modulation orders in high-speed VLC systems, which is the subject of the following subsection.

4.4 LED nonlinearity compensation

4.4.1 Adaptive Volterra-based postdistorter

Several linearization approaches have been proposed in previous works to mitigate the nonlinear distortions, including the Volterra series model [114, 122], the memory polynomial model [101], or more recently, machine learning algorithms [71, 79, 90]. In this study, the second-order Volterra series model is implemented, as it provides good performance at high data rate [144]. Herein, the Volterra series model is implemented as a postdistorter as opposed to 4.3.2 where the Volterra series was employed to model the nonlinearity of

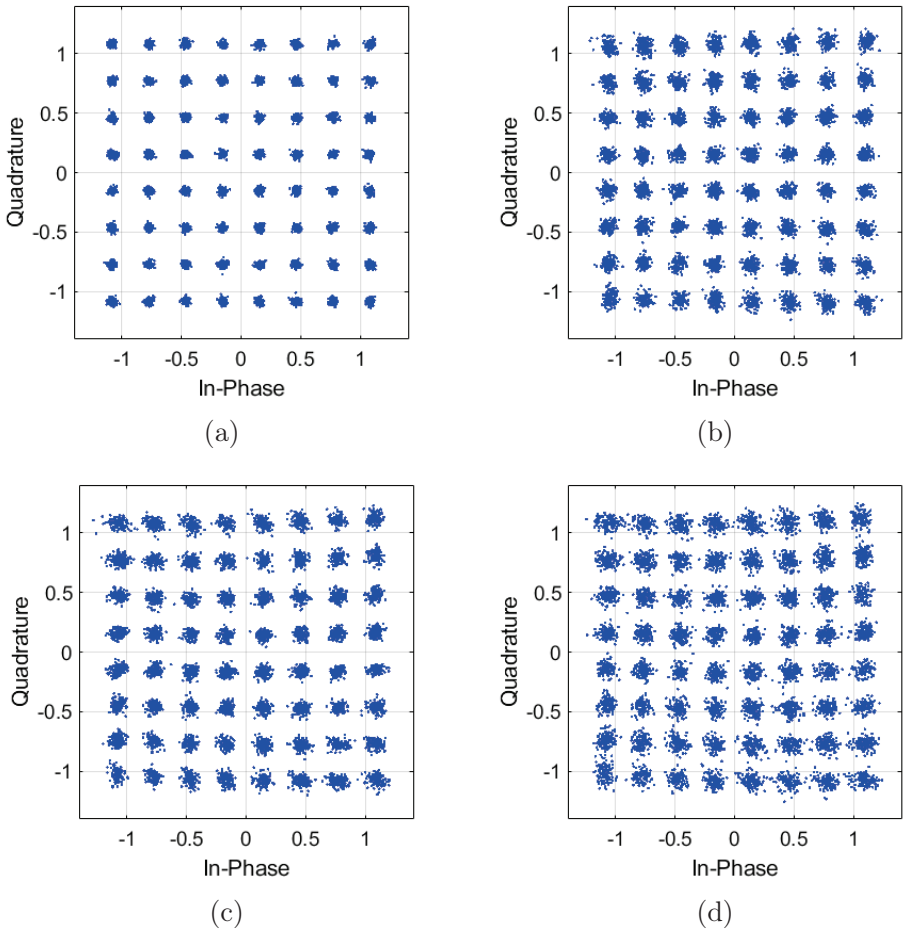

Figure 4.7 Received constellation in simulation (a) without the nonlinearity, (b) with the Hammerstein model, (c) with the Volterra model, and (d) in the experiment for a 64-CAP (with 6 bits encoded per symbol) at 135 Mbps.

the LED. Therefore, the only difference is that the algorithm searches for the optimum set of coefficients of the Volterra series to rectify the received discrete-time signal $y(n)$ with knowledge of the transmit sequence of undistorted symbols $s(n)$. A diagram of the adaptive postdistortion method is presented in Fig. 4.8. The output of the Volterra-based postdistorter $\hat{s}(n)$ can therefore be expressed as

$$\begin{aligned}\hat{s}(n) = &\sum_{m_1=0}^{M_1-1} h_1(m_1)y(n-m_1) \\ &+ \sum_{m_1=0}^{M_2-1}\sum_{m_2=0}^{M_2-1} h_2(m_1,m_2)y(n-m_1)y(n-m_2),\end{aligned} \tag{4.22}$$

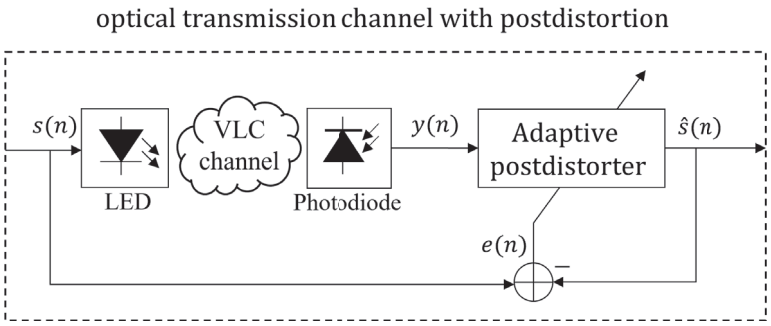

Figure 4.8 Principle of adaptive postdistortion for LED nonlinearity mitigation in VLC.

The optimum coefficients $h_k(m_1, \ldots, m_k)$ are adaptively determined by using the RLS algorithm, in a similar fashion as in Section 4.3.2, except that least squares cost function is defined now as

$$\underset{h_k(m_1,\ldots,m_k)}{\operatorname{argmin}} \sum_{n=0}^{M_{samp}-1} \mid s(n) - \hat{s}(n) \mid^2, \tag{4.23}$$

4.4.2 Numerical Results

The performance of the Volterra-based postdistorter is evaluated in simulation with a 135 Mbps 64-CAP signal. The modulated signal is first distorted by the Volterra series model and is then passed through the postdistortion function. Furthermore, the channel is assumed to be noiseless in order to focus solely on the ability of the proposed postdistortion technique to effectively mitigate the nonlinear distortions. It should be mentioned that a FSE-DFE is always applied to remove the residual ISI stemming from the LED response. When postdistortion is mentioned in the present document, we refer solely to the mitigation of nonlinearity. The LMS algorithm is employed to adapt the coefficients of the FSE-DFE, while the RLS algorithm is used to adapt the coefficients of the postdistortion function based on the Volterra series. For both LMS and RLS algorithms, the coefficients are adapted during a training phase. The number of feedforward taps and feedback taps of the equalizer is chosen to be sufficiently large, i.e. respectively 140 and 48, so that the coefficients of the equalizer converge to a set of optimum coefficients. Now the NSME metric is used to quantify the error between the symbols at the output of the FSE-DFE $\hat{c}_k$ and the undistorted symbols c_k at the transmitter (see Fig. 4.1).

Two cases are considered for this simulation: 1) the postdistortion compensation is applied (Fig. 4.9 (b)) and 2) the nonlinearity is left unmitigated (Fig. 4.9 (a)). The reported

NMSE is -27.7 dB for the former and -35.8 dB for the latter case, thus confirming the effectiveness of the proposed nonlinearity compensation technique.

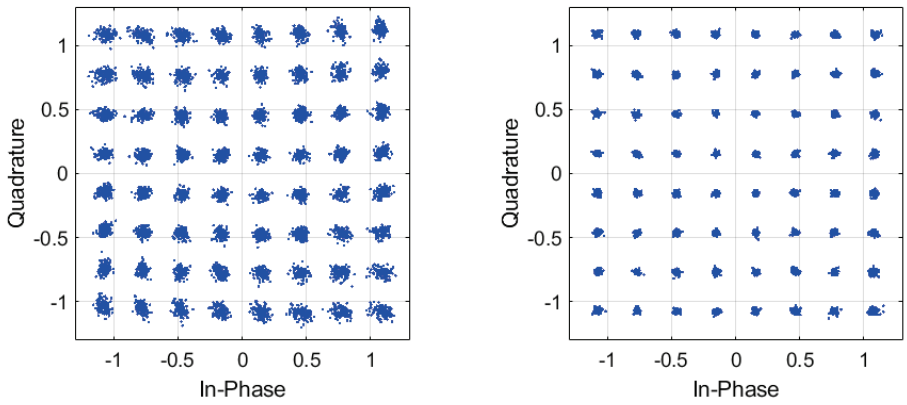

(a) (b)

Figure 4.9 Received constellation when (a) the nonlinearity is unmitigated (NMSE = -27.7 dB) and (b) when the nonlinearity is compensated by the Volterra postdistortion algorithm (NMSE = -35.8 dB) .

4.5 Chapter summary

In this chapter, we have presented a simulation model for our experimental VLC system that can model the distortions stemming from the LED nonlinearity. The distance between simulation and experiment in terms of SNR was quantified, and we have established that the numerical results might exhibit slightly superior performance due to a $\sim$ 2 dB overestimation in SNR.

Furthermore, we have evaluated two nonlinearity models with memory, namely the Hammerstein model and the Volterra series model. While the former benefits from a simpler implementation, it lacks accuracy for large signal bandwidths. More generally, we have shown that compensating the LED nonlinearity is critical to increase the throughput of VLC systems employing low-cost LEDs. These results have been published in the form of a technical article for the company MathWorks [74]. Finally, we have demonstrated that postdistortion based on the Volterra series is an appropriate choice to mitigate the nonlinear effects in high speed VLC systems.

In the next chapter, we will compare three modulation schemes, namely PAM, CAP and DMT. Moreover, the postdistortion method we presented will be applied in practice to PAM and CAP signals.

CHAPTER 5

Comparison of PAM and CAP modulation

5.1 Introduction

White LEDs are nowadays widely used for lighting applications [56]. They consist of a blue LED chip coated with a phosphor layer, producing white light. Unfortunately, their modulation bandwidth does not exceed a few MHz due to the relaxation time of the phosphor layer, thus severly limiting throughput [115]. To overcome this, spectrally-efficient signaling schemes are commonly considered in VLC, such as PAM, CAP, and DMT. However, it is still not clear which modulation scheme is best suited for VLC. Many experimental studies show that systems employing DMT can achieve data rates on the order of several Gbps [29, 13]. Some results have also shown that when PAM and CAP modulations are implemented, data rates of similar order can be achieved [127, 112].

Furthermore, comparisons of PAM, CAP and DMT have been carried out in the literature for VLC in terms of available bitrates and robustness against LED nonlinear distortions. In [110], the authors compared PAM, CAP and DMT on an experimental setup employing a white LED. Under different signal attenuations, they highlighted the robustness of two-level PAM (2-PAM) against LED nonlinearities, which performed advantageously with respect to CAP and DMT. The authors of [67] compared high-order PAM (8-PAM) and CAP (64-CAP) with DMT employing frequency-domain equalization. They reported better performance for DMT compared to high-order PAM and CAP. Moreover, CAP outperformed PAM for high data rates. In [113], the authors performed an optimization of the roll-off factor and demonstrated that 4-PAM can outperform 4-CAP and DMT.

It is noteworthy, however, that none of these studies took into account the constraints associated with the illumination function. VLC systems typically employ IM/DD, where the transmitted waveform is encoded in the instantaneous radiated optical power. In this context, the desired illumination brightness level limits the total optical power at the receiver, thus impacting communication link quality. Moreover, the authors of [67] and [113] did not consider a nonlinear LED dynamic range and did not provide experimental results, yet it is known that LED nonlinear distortions can severely degrade overall system performance [30]. It is reasonable to assume that modulations with higher PAPR will suffer more degradation due to nonlinearity. In previous work by our team [59], DMT was

optimized under lighting constraints with the same experimental VLC setup and a 100 Mbps transmission was achieved at a targeted BER of 10^{-3}. Therefore, this study focuses on optimization and comparison of PAM and CAP.

In this chapter, we study the impact of different parameters of single-band CAP and PAM when extending as much as possible the signal bandwidth while employing equalization and/or postdistortion techniques to jointly mitigate the frequency selectivity and the nonlinear effects of the LED. In addition, a constant brightness level that is compliant with illumination standards is maintained at the receiver. Moreover, given that a low signal PAPR is usually preferred to optimize the occupation of the LED dynamic range and thus maximize the transmit power, PAM and CAP were chosen over multi-band CAP and DMT-based techniques, which are known to exhibit higher PAPR and can induce a power penalty. For both CAP and PAM schemes, the impact of the roll-off factor and the maximum achievable bit rate is investigated in simulation while assuming a perfectly linear LED dynamic range. In addition, an experimental transmission is performed to study the performance of high-order 8-PAM and 64-CAP, with and without compensation of the LED nonlinearity. In our study, the average optical power is kept constant for all modulated signals to set the desired level of illumination. However, the electrical signal powers are different, since the modulated signals occupy the entire dynamic range of the LED as opposed to [110]. In addition and as opposed to [113], higher modulation orders will be studied, namely 8-PAM and 64-CAP and the LED nonlinearity will be integrated into the study through experiments.

The simulation model presented in Section 4.2 is employed for the numerical analysis in this chapter, and a linear transfer characteristic is assumed in the transmission chain model. However, in the experiment, adaptive postdistortion compensation must be applied to compensate the nonlinear impairments and thus linearize the VLC system. The experimental test bench and illumination constraints are identical to that of Chapter 3 and Chapter 4.

The remainder of the paper is organized as follows: Section 5.2 presents an analytical description of PAM and CAP modulation. In Section 5.3, the impact of the roll-off factor parameter is investigated, along with the maximum bit rate for different modulation orders under illumination constraints. In Section 5.4, an experimental transmission is performed to highlight the effects of LED nonlinearity and the modulation index is investigated. Finally, Section 5.5 concludes the chapter.

5.2 Modulation schemes

The two modulation schemes compared in this chapter are PAM and CAP. An analytical description of PAM is given in 5.2.1, while CAP is presented in 5.2.2.

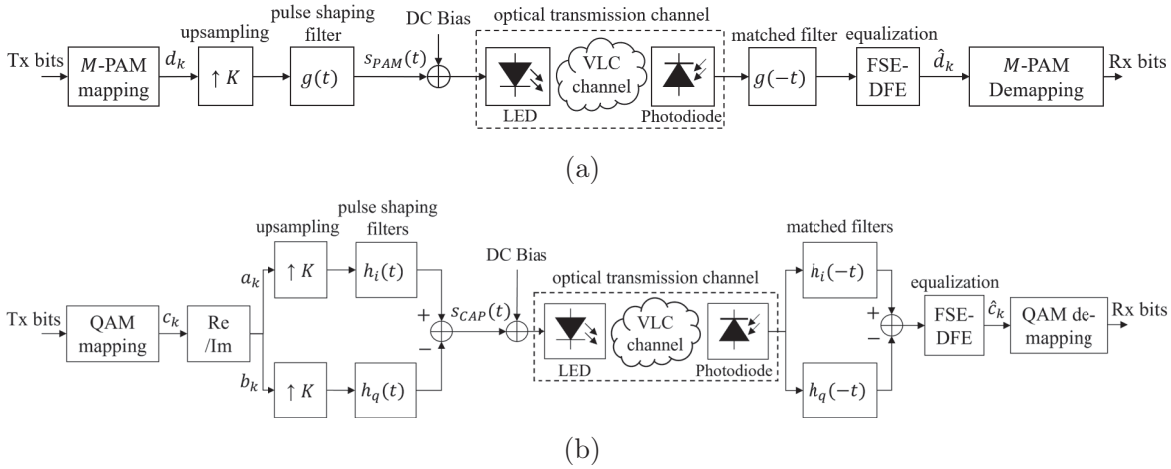

Figure 5.1 Schematic block diagrams of (a) PAM and (b) CAP transceivers for VLC.

5.2.1 PAM modulation

PAM is a modulation scheme where the information is encoded in the amplitude of the transmitted pulse. Here, a SRRC pulse shaping filter is employed to optimize spectral occupancy. Fig. 5.1 (a) shows a schematic of a PAM transceiver. The incoming bits are firstly modulated by a PAM modulator where the signal levels are defined as $\pm 1, \pm 3, \ldots, \pm M-1$, and where M is the modulation order. Then, the modulated symbol stream d_k is upsampled by a factor K and convolved with a SRRC filter $g(t)$, yielding the transmitted PAM signal prior to DC bias addition

$$s_{PAM}(t) = \sum_{k=-\infty}^{+\infty} d_k g(t - kT), \tag{5.1}$$

where T is the symbol period. The PAM modulation bandwidth B_{PAM} is therefore limited by the maximum frequency of the pulse shaping filter $g(t)$, such that

$$B_{PAM} = \frac{(1+\alpha)}{2T} = \frac{(1+\alpha)D_b}{2m_{PAM}}, \tag{5.2}$$

where α is the roll-off factor parameter denoting the excess bandwidth, D_b is the bit rate and m_{PAM} is the number of bits encoded in one PAM symbol. The PAM modulated spectrum for various values of α and the LED frequency response are shown in Fig. 5.2

(a). Then, a DC bias is added for illumination purposes and to ensure full swing of the modulated signal in the dynamic range of the LED. Note, after the DC bias addition, the modulated signal is unipolar and positive. At the receiver, the received signal is passed through the matched filter $g(-t)$ prior to equalization. The equalizer employed in this study is a FSE-DFE operating at the rate $4/T$. The principle of the FSE-DFE was detailed in 4.2.6. Finally, the equalized PAM symbols are de-mapped in order to recover the transmitted bits stream.

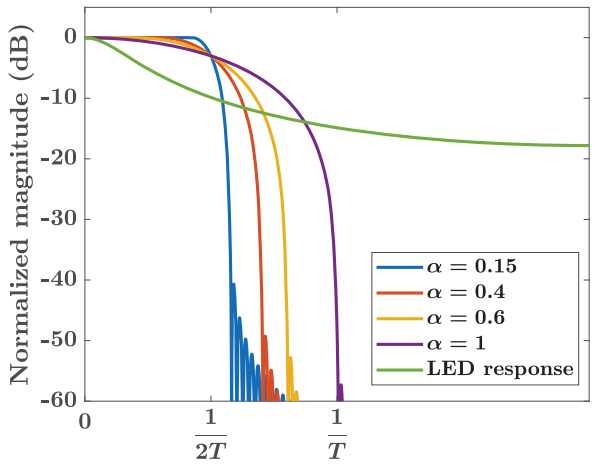

(a)

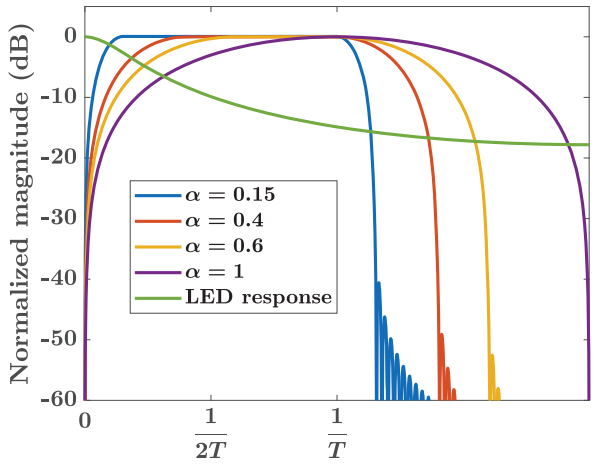

(b)

Figure 5.2 PAM (a) and CAP (b) modulated spectra for various roll-off factors and LED normalized frequency response.

5.2.2 CAP modulation

The principle of CAP modulation was well described in Section 3.2. Recall that the CAP modulated signal $s_{CAP}(t)$ prior to DC bias addition is defined as

$$s_{CAP}(t) = \sum_{k=-\infty}^{+\infty} a_k h_i(t - kT) - b_k h_q(t - kT), \tag{5.3}$$

where $h_i(t)$ and $h_q(t)$ are the in-phase and quadrature filters, respectively, and a_k and b_k are the real and imaginary parts of the QAM modulated symbols, respectively. The total occupied bandwidth B_{CAP} is equal to

$$B_{CAP} = \frac{(1+\alpha)}{T} = \frac{(1+\alpha)D_b}{m_{CAP}}, \tag{5.4}$$

m_{CAP} being the number of bits per symbol in CAP. The shape of the CAP modulated spectrum for various values of α and the LED frequency response is shown in Fig. 5.2 (b).

5.2.3 Spectral efficiency of PAM and CAP

The spectral efficiency is generally defined as the ratio between the bit rate D_b and the total occupied bandwidth B such that

$$\eta = \frac{D_b}{B}. \tag{5.5}$$

Thus, the spectral efficiencies of PAM and CAP, namely η_{PAM} and η_{CAP} respectively, can be derived using (5.5), (5.2) and (5.4) as follows:

$$\eta_{PAM} = \frac{2m_{PAM}}{(1+\alpha)}, \tag{5.6}$$

$$\eta_{CAP} = \frac{m_{CAP}}{(1+\alpha)}. \tag{5.7}$$

When comparing PAM and CAP modulations at the same spectral efficiency, we can note that a higher modulation order will be required for CAP compared to PAM modulation. In fact, the number of bits per symbol in CAP needs to be twice that of PAM, such that $m_{CAP} = 2m_{PAM}$.

5.3 Numerical analysis

5.3.1 Impact of roll-off factor

The roll-off factor α of the SRRC pulse shaping filter (for PAM) and the in-phase and quadrature filters (for CAP) can be jointly optimized with the modulation bandwidth

in order to maximize the system throughput. The roll-off factor impacts the modulated signal on two important fronts, namely 1) the spectral energy distribution and 2) the PAPR.

1) Spectral energy distribution: In PAM, most of the energy of the modulated spectrum is concentrated in the low frequencies. Therefore, when increasing the modulation bandwidth (hence, the data rate) beyond the 3-dB bandwidth of the LED, about the same power loss is experienced regardless of roll-off factor. On the other hand, the power in the CAP spectrum is concentrated around f_c and there is no energy at $f = 0$. Therefore, the CAP signal is more subject to power losses due to the LED low-pass behavior than PAM modulation. Moreover, in CAP, larger values of α lead to higher attenuation.

2) PAPR: A low PAPR is preferred in order to enable full swing of the modulated signal in the fixed dynamic range of the LED, and thus to maximize the transmitted electrical power.

5.3.2 Maximum throughput investigation

In order to evaluate the maximum bit rate of PAM and CAP in simulation, we define the power margin as the difference between the estimated SNR at the receiver after transmission through the VLC system and the SNR required to achieve a BER of 10^{-3} at a given bit rate. To this extent, a power margin superior to 0 dB implies a transmission at a BER $\leq 10^{-3}$ for an illumination of 500 lx.

In order to illustrate the notion of power margin, the BER performance of 4-PAM and 16-CAP as a function of SNR and at a throughput of 172.5 Mbps is presented in Fig. 5.3.

The received SNR after transmission for 4-PAM and 16-CAP is represented by vertical dashed lines and is equal to 34.7 dB and 40.6 dB, respectively. As explained in 5.3.1, the received SNR for 4-PAM and for 16-CAP at the same bit rate are not both equal because the PAM and CAP signals do not experience the same attenuation after transmission through the VLC channel. Furthermore, the transmit powers differ due to different PAPRs. In fact, the power of the 4-PAM signal at the transmitter before transmission through the VLC channel is determined to be 1.1 dB higher than that of 16-CAP. Moreover, the power loss due to the LED response at the considered bit rate of 172.5 Mbps is about -3.6 dB and -8.4 dB for 4-PAM and 16-CAP, respectively.

For both PAM and CAP, the noise-equivalent bandwidth is 43.125 MHz and the noise power spectral density is about -146 dBW/Hz. Therefore the received SNR of 4-PAM is about 5.9 dB higher than that of 16-CAP. In addition, it can be seen from Fig. 5.3 that

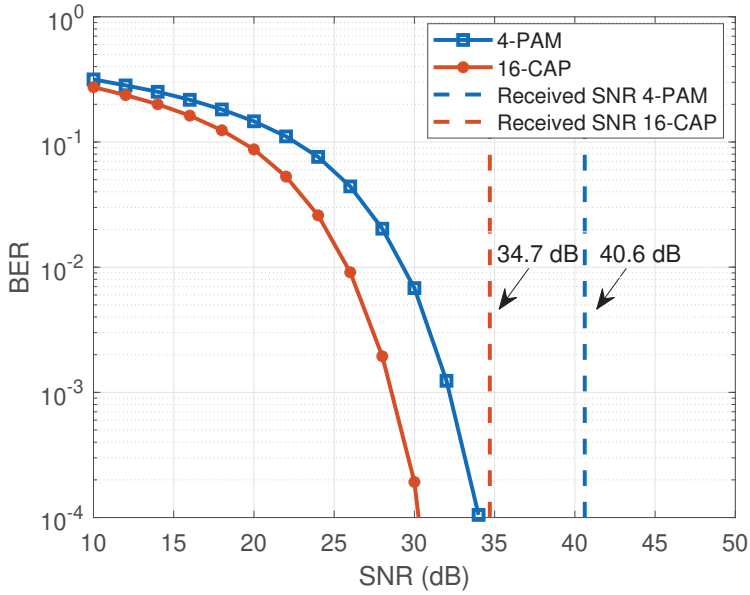

Figure 5.3 BER performance of 4-PAM and 16-CAP at 172.5 Mbps with $\alpha = 0.15$ and estimated received SNR for each modulation scheme.

the required SNR to achieve a BER of 10^{-3} is $\sim$ 32.2 dB for 4-PAM and $\sim$ 28.6 dB for 16-CAP. Consequently the power margin is equal to 8.4 dB and 6.1 dB for 4-PAM and 16-CAP, respectively.

The results for different power margins according to different values of α are shown in Fig. 5.4. It should be noted that the dashed red line on the graphs corresponds to the 50 MHz bandwidth bound of the VLC system. For example, as illustrated in Fig. 5.4 (a), for a 2-PAM signal and assuming a 50 MHz total occupied bandwidth, a 86.25 Mbps transmission at a BER lower than 10^{-3} can be achieved with a 0.15 roll-off factor and a very comfortable 18.4 dB margin. On the other hand, a transmission rate of only 72.5 Mbps is achievable given a roll-off factor of 0.4, albeit with a higher margin equal to 24.3 dB. It is of interest that for higher modulation bandwidths (obtainable with better electronic components), the red line would move upwards, indicating higher possible throughputs.

The following observations can be drawn from Fig. 5.4:

- *For PAM:* it can be noticed in Fig. 5.4 (a), (c) and (e) that, for a given power margin, the maximum bit rate is achieved for $\sim \alpha = 0.4$, i.e., when the PAPR is the lowest, as can be seen in Fig. 5.5. Under this condition, the input LED driving signal can span the full LED dynamic range and thus the transmitted electrical power can be maximized. Consequently, the power margin is increased, and a higher achievable

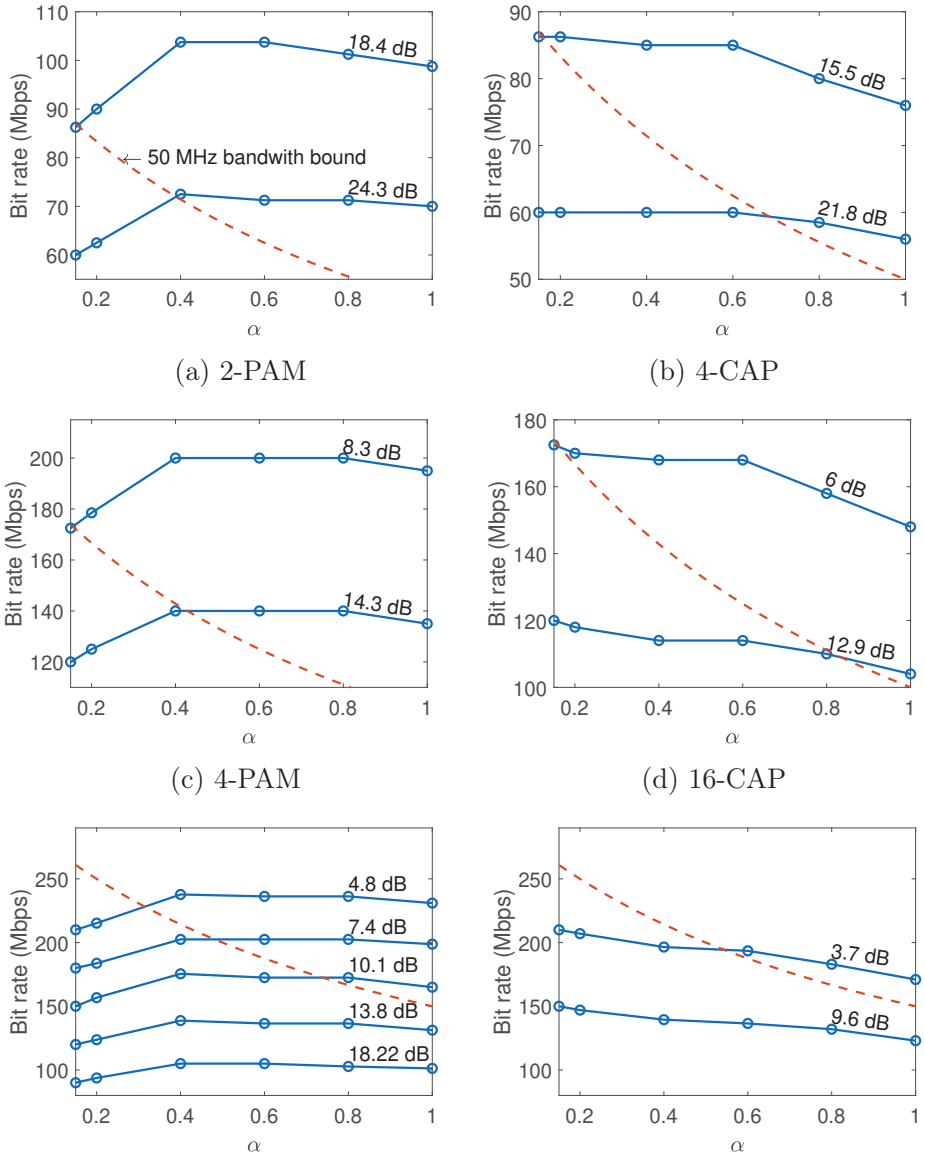

(a) 2-PAM (b) 4-CAP

(c) 4-PAM (d) 16-CAP

(e) 8-PAM (f) 64-CAP

Figure 5.4 Achievable bit rate for (a) 2-PAM, (b) 4-CAP, (c) 4-PAM, (d) 16-CAP, (e) 8-PAM and (f) 64-CAP for a given power margin according to various values of roll-off factor. The dashed red curve on the plots corresponds to the bandwidth boundary of 50 MHz.

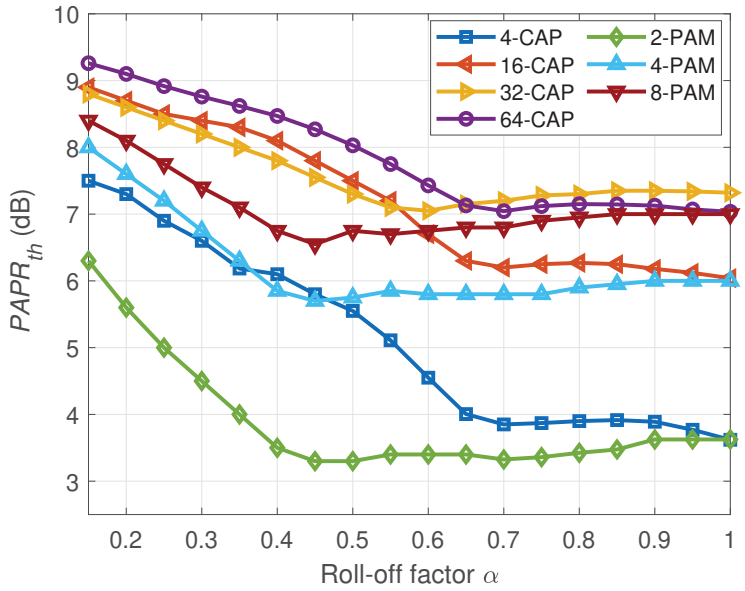

Figure 5.5 PAPR threshold of PAM and CAP signals for $P_r(PAPR > PAPR_{th}) = 10^{-4}$ for various roll-off factors.

bit rate can be achieved. It can also be seen that the PAPR slightly increases when α approaches 1 (on the order of 0.5 dB), which accounts for the slightly decreasing bit rate in Fig. 5.4 (a), (c) and (e).

- *For CAP:* unlike PAM; the power loss experienced by the signal after filtering by the LED impulse response increases with the value of α. This can be directly seen in Fig. 5.2 (b) which shows the shape of the CAP modulated spectrum for various values of α and the LED frequency response. As the roll-off increases, the signal spectrum is shifted around a frequency $f_c = (1+\alpha)/2T$ and is subject to a stronger attenuation after filtering by the LED response. On the other hand, the decreasing PAPR leads to more power at the receiver. In fact, the PAPR of CAP signals decreases when the roll-off factor increases to reach its minimum value for $\alpha = 0.6$ for 4-CAP, 16-CAP and 64-CAP and around 0.55 for 32-CAP as observed in Fig. 5.5. The power gain inherent to the decreasing PAPR does not compensate the power loss due to the attenuation by the LED which accounts for the monotonically decreasing curves in Fig. 5.4 (b), (d) and (f).

In addition, the maximum bit rate for PAM and CAP in a maximum bandwidth of 50 MHz can be achieved with a small value of α, typically 0.15, which yields both a positive power margin and a minimal bandwidth requirement. Moreover, PAM provides a power

margin gain on the order of 2-3 dB and 1-2 dB for 2-PAM and 4-PAM, with respect to 4-CAP and 16-CAP, respectively.

Finally, 8-PAM and 64-CAP are compared and revealed to approximately provide similar total throughput with a slight advantage of $\sim$ 1 dB in power margin for 8-PAM. In addition, simulation results (not shown in figure) show that 64-CAP exhibits slightly higher performance than 32-CAP. In fact, for a bit rate of 210 Mbps, 64-CAP exhibits a power margin of 3.85 dB compared to 3.45 dB for 32-CAP.

5.4 Experimental results

In this section, an experimental transmission is performed to verify the simulation results for high modulation orders (8-PAM and 64-CAP). Adaptive postdistortion compensation based on the Volterra series expansion is employed to mitigate the LED nonlinearity. Performance without postdistortion compensation is also assessed to evaluate the degree of sensitivity to nonlinear impairments. In addition, the modulation index parameter is investigated. Finally, a transmission with bit-loading DMT is performed for comparison with PAM and CAP. As DMT is not a main focus of this study, this is done to provide a comparative benchmark representing this popular modulation scheme.

5.4.1 Experimental setup

Fig. 5.6 shows a diagram of the experimental setup, which is the same as in Chapter 3 and in 3.4.1. The VLC transmission process is thus quickly recalled. Firstly, the modulated signals are generated offline with MATLAB and stored into an AWG memory (Tektronix, AWG 7052, 10 bits resolution). The latter performs a digital-to-analog conversion, and the output modulated signal is combined with a DC bias current by means of a custom board to provide the right level of illumination and to ensure that the driving signal occupies the entire LED dynamic range. The transmission is performed in dark conditions to mitigate the impact of ambient light.

At the receiver side, a 16-mm diameter lens concentrates the light onto a low-cost silicon PIN photodiode (OSRAM SFH-2400) with a 1 mm^2 active surface. The photodiode produces a photocurrent proportional to the received optical power, which is then converted into a voltage signal using a TIA, and high-pass filtered. The received signal is finally sampled by a real-time oscilloscope (LeCroy 64 MXs-A), digitized, and saved for subsequent offline processing. The latter includes resampling, synchronization, postdistortion, matched filtering, FSE-DFE equalization, symbol de-mapping and BER calculation.

The transmitted frame comprises 80 000 known symbols. At the receiver, the FSE-DFE equalizer coefficients are optimized based on the LMS algorithm. The number of feed-forward taps and feedback taps is respectively 140 and 48. Moreover, the coefficients of the postdistorter are obtained after a training phase using the RLS algorithm, and the memory length is set to 17 as a trade-off between performance and complexity.

The key system parameters used in the experiment are summarized in Table 5.1.

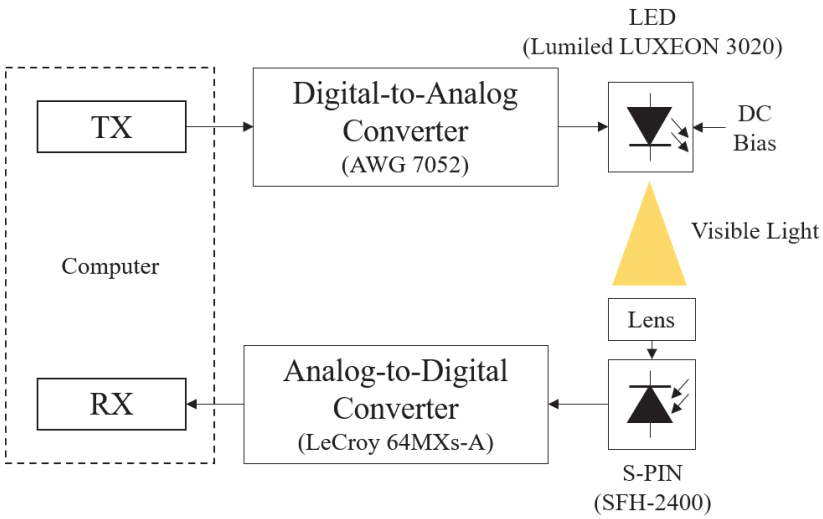

Figure 5.6 Diagram of the experimental VLC setup.

5.4.2 Investigating the modulation index

The assumption that the modulated signals occupy the entire dynamic range of the LED fully reflects the impact of LED nonlinearity, but it is not always necessary to use the full dynamic range in practical VLC systems. To this extent, we introduce the concept of modulation index M_I which is defined as the ratio between the current swing range $\pm\Delta I$ with respect to the DC bias current I_{DC} such that [91]

$$M_I = \frac{\Delta I}{I_{DC}}. \tag{5.8}$$

A modulation index of 1 corresponds to full occupation of the LED dynamic range. To achieve optimal transmission performance, an optimal modulation index can be adopted which can be smaller than 1 under LED nonlinearity. Hence, the following presents an investigation of the modulation index in our experiment.

The impact of the modulation index on the BER performance is experimentally investigated for 210 Mbps and 120 Mbps 8-PAM signals (Fig. 5.7). It can be observed that at

Table 5.1 System parameters

Parameter	Value
LED 3-dB modulation bandwidth	1.47 MHz
Semi-angle at half luminance $\theta_{\frac{1}{2}}$	55°
DC bias current	120 mA
LED output luminous flux	53 lm
Photodiode responsivity at 870 nm	0.65 A/W
Photodiode active surface	1 mm^2
Lens diamater	16 mm
Link distance	20 cm
Illumination level	500 lx
Upsampling factor K	4
SRRC filter length	40 symbol periods
LED dynamic range	0 - 240 mA
Noise PSD N_0	-116 dBm/Hz

210 Mbps, choosing a modulation index inferior to 1 slightly increases the BER, whereas at 120 Mbps, an optimum value of modulation index can be found between 0.65 and 0.85, even though the improvement in terms of BER performance is not so significant. This suggests that optimization of the modulation index is not straightforward and depends on the system transmission bit rate (or more specifically, the ratio between the bit rate and the effective system bandwidth).

When postdistorion is applied to the 120 Mbps 8-PAM signal, the transmission is error-free and is therefore not shown in the figure. However, the mean-squared error can be computed at the output of the equalizer and a degradation of around 1 dB was observed when the modulation index is decreased from 1 to 0.65. In fact, when the nonlinear distortions are mitigated by the postdistorter, the performance depends essentially on the received power. This suggests that a modulation index of 1 is the best choice when the nonlinearity is mitigated to ensure a fair comparison between CAP and PAM.

5.4.3 Impact of LED nonlinearity

In order to highlight the effect of the nonlinear characteristic of the LED on high-order PAM and CAP, transmissions with 64-CAP and 8-PAM were performed and the constel-

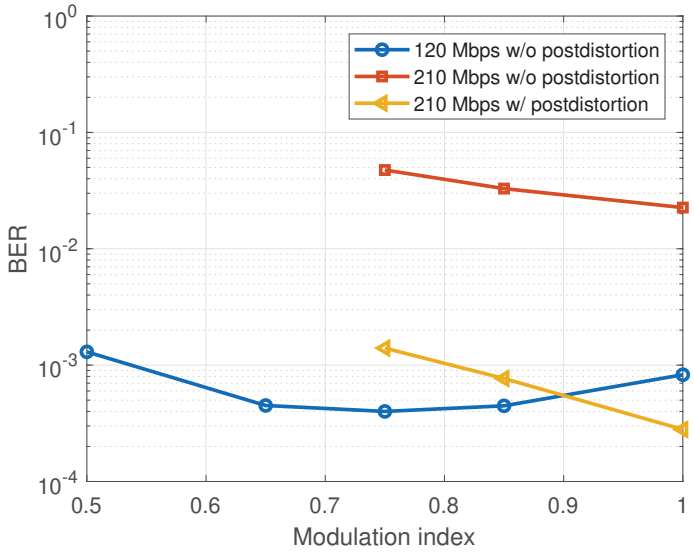

Figure 5.7 BER performance according to various values of modulation index for a 120 Mbps and 210 Mbps 8-PAM signal, without (w/o) and with (w/) postdistortion.

lation and eye diagrams with and without postdistortion compensation are shown in Fig. 5.8. Note, bit rates of 135 Mbps and 99 Mbps were chosen in this case for 64-CAP and 8-PAM respectively, so that the nonlinearity can be differentiated from the noise in the constellation and eye diagram. The impact of LED nonlinearity in 64-CAP is characterized by asymmetrical distortions on the bottom left and top right edge of the received constellation as shown in Fig. 5.8 (a), whereas in 8-PAM, the nonlinear distortions are characterized by a narrower spacing of amplitude levels in the upper and lower parts of the eye diagram as can be seen in Fig. 13 (c). Moreover, as shown in Fig. 5.8 (b) and (d), the postdistortion algorithm effectively mitigates the nonlinearity.

Secondly, we perform an experimental transmission of 8-PAM and 64-CAP at the same bit rate, namely 210 Mbps, for various values of roll-off factor α. It should be noted that at this bit rate, the power margin is around 4.8 dB for each modulation scheme, according to simulation results.

The received spectra of the 210 Mbps transmission with 8-PAM and 64-CAP are shown in Fig. 5.9 (a) and (b), respeectively, and the BER performance is plotted in Fig. 5.10. First, it can be seen that without nonlinearity compensation, 8-PAM provides the poorest BER performance regardless of the value of the roll-off factor, and the calculated BER is around $\sim 2.1 \times 10^{-2}$, whereas it is $\sim 3 \times 10^{-3}$ for 64-CAP. Therefore, in practice, CAP modulation with high modulation orders provides lower BER than PAM when nonlinearity

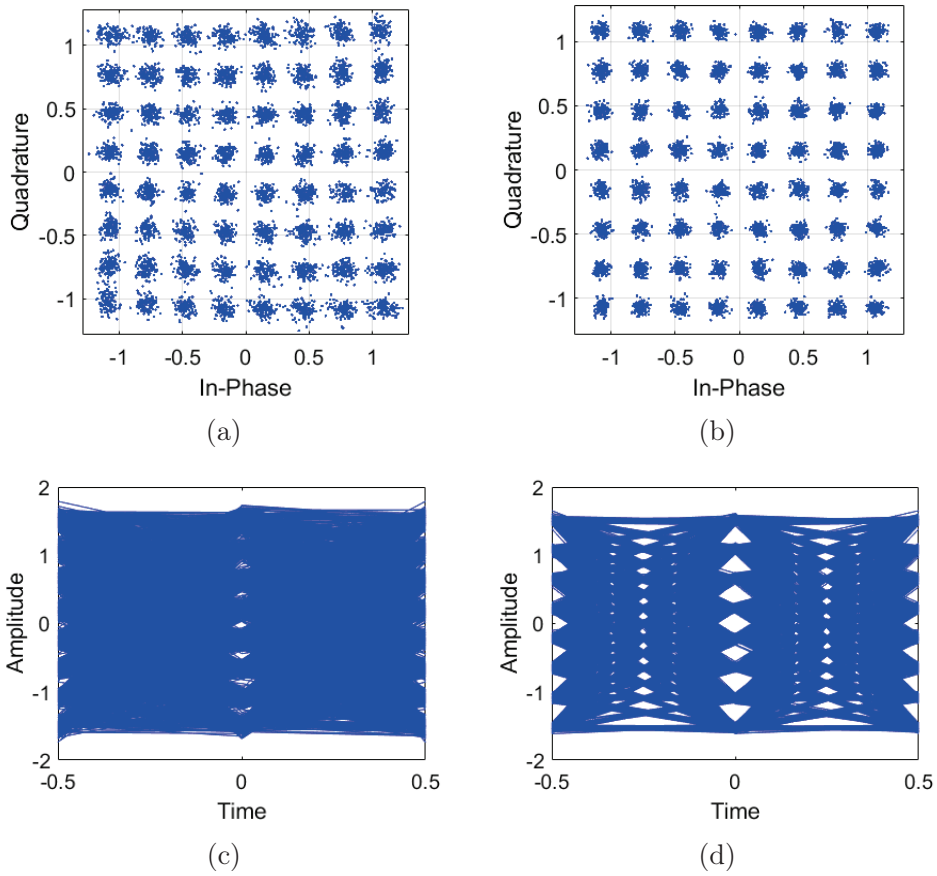

Figure 5.8 Received constellation diagrams for 135 Mbps 64-CAP signal without (a) and with (b) nonlinearity mitigation, and eye diagrams for 99 Mbps 8-PAM signal without (c) and with (d) nonlinearity mitigation.

compensation is absent. On the other hand, when the LED nonlinear distortions are mitigated, the 64-CAP signal suffers more degradation compared to 8-PAM, which supports the simulation results in Section 5.3.2. For instance, for $\alpha = 0.2$, the BER performance drops from 4.2×10^{-2} to 3.4×10^{-4} for 8-PAM and from 3×10^{-3} to 8.7×10^{-4} for 64-CAP.

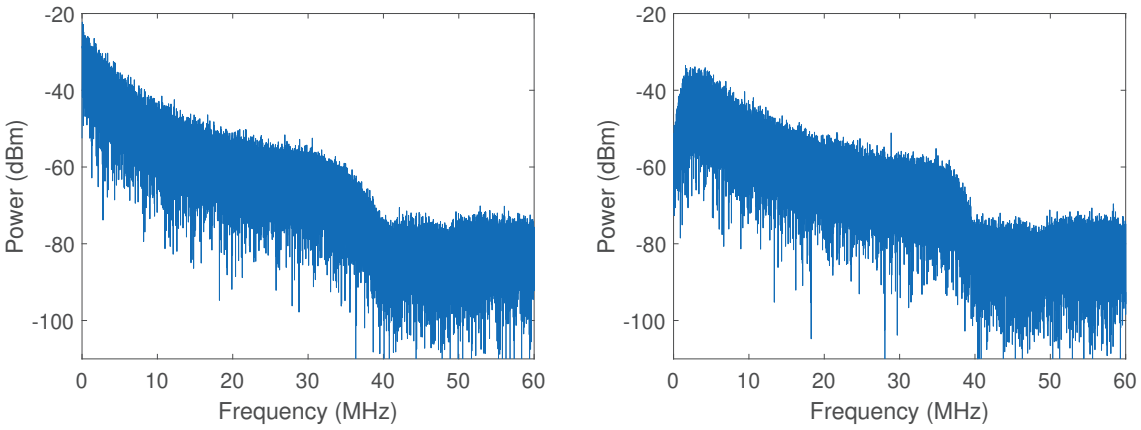

Figure 5.9 Received spectra for 210 Mbps 8-PAM (a) and 64-CAP (b) signals.

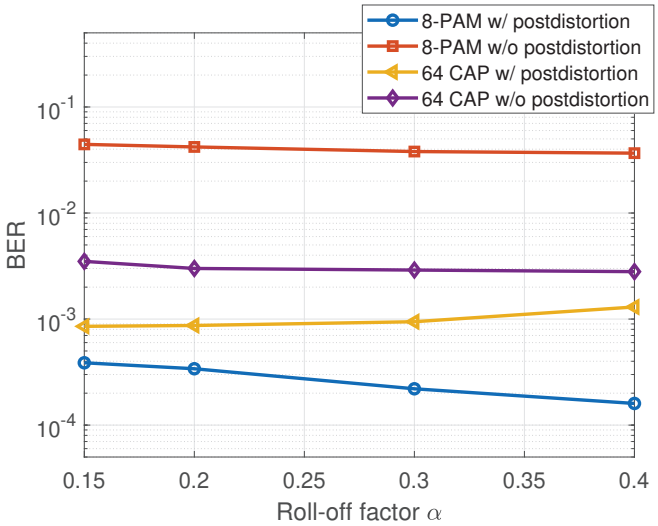

Figure 5.10 BER performance of 64-CAP and 8-PAM for various roll-off factors with compensation of the nonlinearity (w/ postdistortion) and without compensation (w/o postdistortion).

Furthermore, when postdistortion is applied, the BER performance of 8-PAM improves when the roll-off factor increases from 0.15 to 0.4 while that of 64-CAP becomes poorer, which is in line with the results provided by the simulation and presented in Fig.5.4 (c) and (f).

These results can be contrasted with [110] where low-level PAM is recommended over CAP because of the inherent robustness of the former scheme against nonlinear distortions. However, when high modulation orders are employed in the context of high speed communication, CAP exhibits more robustness compared to PAM against nonlinear distortions. Moreover, these results highlight the necessity of postdistortion for high-order PAM and CAP.

5.4.4 Comparison with previous DMT experiments

Other than in the case of PAM and CAP, DMT is a multicarrier modulation technique where the signal bandwidth is divided into subcarriers onto which are mapped QAM complex symbols. The principle of DMT is presented more exhaustively in Appendix B. With knowledge of the channel state, power allocation and bit loading algorithms can be employed to benefit as much as possible from the available modulation bandwidth and therefore maximize the system throughput for a target BER [80]. DMT offers the advantage of simple equalization since a single-tap equalizer is needed to compensate the effects of the flat fading channel experienced by each subcarrier, whereas a more complex equalizer is required for PAM and CAP to cope with ISI, such as FSE-DFE.

In a previous study from 2020 [59], an experiment was carried out with DMT under identical conditions and using the same experimental setup. Without compensating LED nonlinearity, a $\sim$ 100 Mbps transmission rate was successfully achieved at a BER of 10^{-3}, which is significantly less than the achievable transmission rates demonstrated in this study with PAM and CAP. A major reason for the difference of performance is the high PAPR in DMT. In fact, bilateral amplitude clipping must be applied to fit the signal within the dynamic range of the LED, at the expense of clipping noise. In addition, the LED nonlinear distortions on the time-domain DMT signal generate inter-carrier interference, which degrades the overall system performance.

For comparison purposes against PAM and CAP, let us assess the achievable bit rate of DMT when LED nonlinearity distortion is mitigated. To this end, DMT pilots with 512 subcarriers loaded with QAM symbols are sent through the VLC system. The sampling frequency of the AWG generator is set to 120 MS/s. At the receiver, the SNR per subcarrier for a target BER of 10^{-3} is calculated and the number of allocated bits per subcarrier is computed using Chow's algorithm. The results are presented in Fig. 5.11 (a) and (b). It can be observed that the SNR per subcarrier is significantly improved when the impact of LED nonlinearity is mitigated with the postdistorter, and the total number of allocated bits in one DMT symbol increases from 1646 to 2526. As a result, considering the cost of the cycling prefix set to 33 samples, the achievable practical transmission bit rate is $\sim$

95 Mbps and $\sim$ 145 Mbps without and with nonlinearity compensation, respectively. By comparing these results with that of 5.4.3, it can be concluded that DMT provides lower throughput than PAM and CAP.

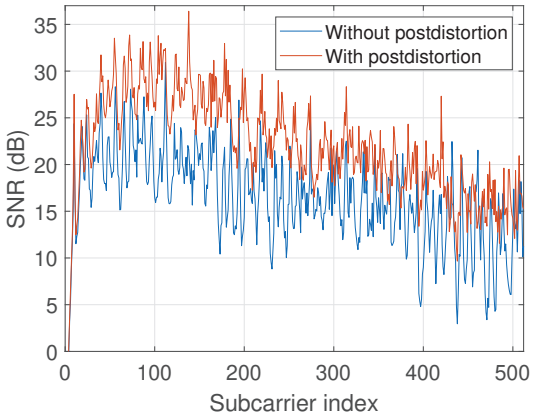

(a)

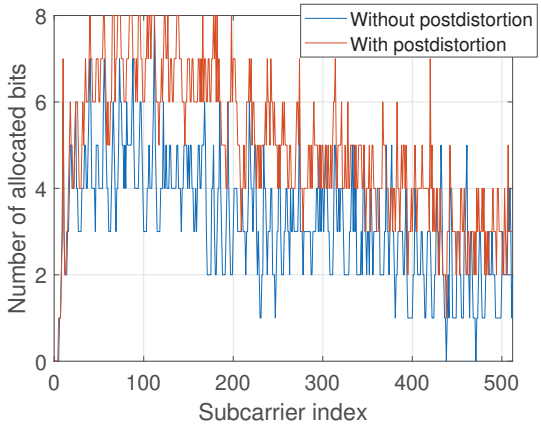

(b)

Figure 5.11 SNR (a) and number of allocated bits (b) per subcarrier.

5.5 Chapter summary

In this chapter, two modulation schemes were compared through simulation and experiment, namely PAM and CAP, employing a low-cost white LED and meeting the requirements of illumination standards for indoor lighting. It was observed that typical indoor lighting requirements lead to a sufficiently high SNR to enable transmission with high-order PAM and high-order CAP such as 8-PAM or 64-CAP. The impact of the roll-off factor on the system performance was also studied. It is shown that a small value of roll-off factor (i.e., 0.15) is preferred to achieve maximum throughput and reduce bandwidth requirements. However, when no bandwidth limitation is imposed by the electronic

circuitry, the optimum value is around 0.4 for PAM and 0.15 for CAP. The simulation results indicate a slight advantage for PAM over CAP in terms of achievable throughput. The achievable data rates for both modulation formats are nonetheless similar, and are on the order of a few hundred Mbps.

It was also found that the LED nonlinearity has a significant impact on the system performance when employing PAM and CAP with a large constellation size, and that the two modulation schemes are affected differently by the nonlinear distortions. Adaptive postdistortion based on the Volterra series expansion was implemented to cope with the nonlinear behavior of the LED in practice. The performance of highly spectral-efficient modulation schemes such as 8-PAM and 64-CAP were analyzed with and without postdistortion. In conclusion, the nonlinear distortions can severely degrade the performance of 8-PAM, whereas 64-CAP shows more robustness. However, when the VLC system is linearized by the postdistorer, 8-PAM is the most suitable modulation scheme. Finally, different values of modulation index were evaluated and it was concluded that setting the modulation index to 1 at high data rate is an appropriate choice to optimize the transmit power for PAM and CAP and obtain better overall performance, despite the presence of nonlinearity in the system. Obviously, when the nonlinear distortions are mitigated, it is also preferable to occupy the full dynamic range of the LED.

The performance study focused on single-band CAP and PAM modulation, which offer very good performance in terms of low PAPR in relation with our initial requirements. Furthermore, the results indicate that high-order CAP and PAM with postdistortion perform substantially better than DMT in terms of achievable transmission rate and are suitable for high-speed VLC systems under illumination constraints. The results presented in this chapter have been published in the IEEE Photonics Journal [99].

CHAPTER 6

MIMO techniques with imager

6.1 Introduction

In order to achieve high VLC throughputs in spite of the bandwidth limitation of the white LED, many research efforts have explored the use of spectrally-efficient modulations such as PAM, CAP modulation, and DMT in conjunction with equalization at the receiver. Another avenue to increase throughput consists in separately modulating the multiple LEDs which, in conjunction with multiple photodetectors at the receiver, leads to a MIMO link.

Among the MIMO techniques, spatial multiplexing (SMP) and spatial modulation (SM) are two widely used schemes, whose principles were described in 2.7.2 and in 2.7.3, respectively. In SMP, all the transmit LEDs are active during a symbol period and transmit independent optical symbols. In SM, a single LED is active and transmits an optical symbol during a symbol period, while the other LEDs are idle.

In the context of MIMO transmission, an imaging receiver can be employed to separate the beams at the receiver and improve the overall system performance. The application of imaging receivers to optical wireless communications has been extensively studied in the literature. Early studies in wireless infrared communications have demonstrated the benefits of employing an imaging receiver over a non-imaging receiver for reducing the power requirements due to a decrease in ambient light noise, receiver thermal noise, and multipath distortion [62]. In [61], a receiver chip with a photodetector array was designed for imaging setups. In addition, the performance of SM and SMP techniques were evaluated for both imaging and non-imaging systems in [19] and in [46].

The most recent laboratory experiments on imaging MIMO systems have considered a perfectly aligned setup [123, 53], and thus the impact of imager misalignment on the performance of MIMO techniques remains poorly understood to date. In a practical indoor scenario, the receiver location and orientation may vary due to the movements of the user below the transmit luminaire. In fact, user mobility is still a major challenge which must be addressed in order to unlock the full potential of VLC networks.

The goal of this chapter is to investigate the impact of imager misalignment on the performance of SMP and SM in the context of receiver mobility. In order to determine which MIMO technique is the best suited, SMP and SM are first compared. At this juncture, it was determined that SMP offered superior performance. Then a form of adaptive bit-loading is studied in conjunction with SMP to compensate the loss induced by the imager misalignmeent. In this chapter, channel gains measurements are performed on a 2×2 VLC experimental test bench we developed based on low-cost components.

The remainder of this chapter is organized as follows: in Section 6.2, the analytical error bound of SM and SMP techniques is derived. In addition, the concept of imaging receiver is presented and its performance is contrasted in simulation with that of the non-imaging receiver for both SMP and SM schemes. Then, in Section 6.4, the 2×2 experimental test bench is described. The compatibility of the MIMO setup with the lighting function is discussed in Section 6.5. In Section 6.6, the channel gains are measured for various locations of the imaging receiver. In Section 6.7, SM and SMP approaches are compared in simulation by leveraging channel responses measured on the test bench. As a second step, an adaptive modulation scheme is developed in conjunction with SMP in order to adapt the constellation order to imaging lens misalignment and maintain the best possible link quality. Lastly, Section 6.8 concludes the chapter.

6.2 SM and SMP techniques

6.2.1 MIMO system model

Consider a MIMO optical transmission system using N_t transmit LEDs and N_r PDs. The received signal $\mathbf{y} = [y_1, \ldots, y_{N_r}]^T$ can be expressed as

$$\mathbf{y} = \mathbf{H}\mathbf{x} + \mathbf{n}, \tag{6.1}$$

where $\mathbf{x} = [x_1, \ldots, x_{N_t}]^T$ is the transmitted signal vector, $\mathbf{n}$ is the noise vector (circularly symmetric AWGN with one-sided power spectral density N_0), and $\mathbf{H}$ is the $N_r \times N_t$ channel matrix. Under the assumption that the channel is frequency non-selective, the channel matrix consists in the real-valued transfer function of the optical wireless links, also referred to as the channel DC gains. It can be written

$$\mathbf{H} = \begin{bmatrix} h_{11} & \dots & h_{1N_t} \\ \vdots & \ddots & \vdots \\ h_{N_r1} & \dots & h_{N_rN_t} \end{bmatrix}, \tag{6.2}$$

where $h_{n_rn_t}$ represents the channel DC gain from a transmitter n_t to a receiver n_r.

6.2.2 Maximum likelihood detection

The BER performance of MIMO techniques in VLC can be analyzed based on the optimum maximum likelihood receiver. For the case of SM, the maximum likelihood receiver can jointly detect the index of the active LED and the transmitted symbol. Specifically, the maximum likelihood detector determines the constellation vector $\bar{\mathbf{x}}$ which minimizes the Euclidean distance metric between the actual received signal vector $\mathbf{y}$ and all possible received signals, i.e.

$$\bar{\mathbf{x}} = \arg\min_{\mathbf{x}} \|\mathbf{y} - \mathbf{H}\mathbf{x}\|_{\mathrm{F}}^2, \tag{6.3}$$

where $||.||_{\mathrm{F}}$ denotes the Frobenius norm.

6.2.3 Analytical BER expression of SM

When M-PAM modulation is employed with SM, the optical intensities are defined as follows:

$$P_{opt,p}^{\mathrm{SM}} = \frac{2P_t}{M+1}p \qquad \text{with } p = 1, \dots, M, \tag{6.4}$$

with P_t being the average emitted optical power. It is noteworthy that signal level "0" must be excluded since the active LED cannot be determined if it transmits nothing. Under the assumption that a maximum likelihood detector is employed at the receiver, the pairwise error probability (PEP) conditioned on the channel matrix $\mathbf{H}$ is the probability that the detector mistakes a transmitted signal vector $\mathbf{x}_{p^{(1)},n_t^{(1)}}$ with another signal vector $\mathbf{x}_{p^{(2)},n_t^{(2)}}$, and is given by [30]

$$\begin{aligned}\mathrm{PEP}_{\mathrm{SM}} &= \mathrm{PEP}(\mathbf{x}_{p^{(1)},n_t^{(1)}} \rightarrow \mathbf{x}_{p^{(2)},n_t^{(2)}}|\mathbf{H}) \\ &= Q\left(\sqrt{\frac{T}{4N_0}||\mathbf{H}\left(\mathbf{x}_{p^{(1)},n_t^{(1)}} - \mathbf{x}_{p^{(2)},n_t^{(2)}}\right)||_{\mathrm{F}}^2}\right) \\ &= Q\left(\sqrt{\frac{T}{4N_0}\sum_{n_r=1}^{N_r} \mid P_{opt,p^{(2)}}^{\mathrm{SM}} h_{n_r n_t^{(2)}} - P_{opt,p^{(1)}}^{\mathrm{SM}} h_{n_r n_t^{(1)}} \mid^2}\right),\end{aligned} \tag{6.5}$$

where $Q(m)$ is the Q-function defined as $Q(m) = \frac{1}{\sqrt{2\pi}}\int_m^{+\infty} \exp\left(\frac{-t^2}{2}\right)dt$. Using the PEP defined in (6.5) and considering all possible MN_t transmitted signal combinations, the BER of SM can be approximated by union bound methods, leading to

$$\begin{aligned}\mathrm{BER}_{\mathrm{SM}} = &\frac{1}{MN_t \log_2(MN_t)} \sum_{p^{(1)}=1}^{M} \sum_{n_t^{(1)}=1}^{N_t} \sum_{p^{(2)}=1}^{M} \sum_{n_t^{(2)}=1}^{N_t} d_{\mathrm{H}}(b_{p^{(1)}n_t^{(1)}}, b_{p^{(2)}n_t^{(2)}}) \\ &\times Q\left(\sqrt{\frac{T}{4N_0}\sum_{n_r=1}^{N_r} \mid P_{opt,p^{(2)}}^{\mathrm{SM}} h_{n_r n_t^{(2)}} - P_{opt,p^{(1)}}^{\mathrm{SM}} h_{n_r n_t^{(1)}} \mid^2}\right),\end{aligned} \tag{6.6}$$

where $d_{\mathrm{H}}(.,.)$ denotes the Hamming distance (defined as the number of nonidentical bits when comparing two bit sequence of equal length), $b_{p^{(1)}n_t^{(1)}}$ is the conveyed bit sequence when the optical power level $P_{opt,p^{(1)}}^{\mathrm{SM}}$ is emitted by transmitter $n_t^{(1)}$ and $b_{p^{(2)}n_t^{(2)}}$ is the conveyed bit sequence when the optical power level $P_{opt,p^{(2)}}^{\mathrm{SM}}$ is emitted by transmitter $n_t^{(2)}$. In SM, the first $\log_2(N_t)$ incoming bits are mapped to a spatial symbol which corresponds to the index of the LED that will be active and the next $\log_2(M)$ are mapped to a symbol in the M-ary signal constellation. For instance, assuming the most significant bit convention is adopted here and that $P_t = 1$, $N_t = 4$ and $M = 2$, the bit sequence "0 0 1" is assigned to the transmitted signal vector $\mathbf{x}_{1,2} = [0\ 0\ 0\ \frac{4}{3}]^T$ and the bit sequence "1 1 1" is assigned to $\mathbf{x}_{2,4} = [\frac{2}{3}\ 0\ 0\ 0]^T$, resulting in a Hamming distance $d_{\mathrm{H}}(b_{1,2}, b_{2,4})$ equal to 2.

6.2.4 Analytical BER expression of SMP

In SMP, the PAM signal levels are expressed as

$$P_{opt,p}^{\mathrm{SMP}} = \frac{2P_t}{M-1}p \qquad \text{with } p = 0, \ldots, (M-1). \tag{6.7}$$

The PEP in SMP is the probability that the detector mistakes a transmitted signal vector $\mathbf{x}_{p^{(1)}}$ with another signal vector $\mathbf{x}_{p^{(2)}}$, and is expressed as [30]

$$\begin{aligned} \mathrm{PEP}_{\mathrm{SM}} &= \mathrm{PEP}(\mathbf{x}_{p^{(1)}} \rightarrow \mathbf{x}_{p^{(2)}}|\mathbf{H}) \\ &= Q\left(\sqrt{\frac{T}{4N_0}||\mathbf{H}\left(\mathbf{x}_{p^{(1)}} - \mathbf{x}_{p^{(2)}}\right)||_{\mathrm{F}}^2}\right). \end{aligned} \tag{6.8}$$

Using the PEP defined in (6.8) and considering all possible M^{N_t} transmitted signal combinations, the BER of SMP can be approximated by union bound methods, thus yielding

$$\begin{aligned} \mathrm{BER}_{\mathrm{SMP}} = \frac{1}{M^{N_t}\log_2(M^{N_t})} \sum_{p^{(1)}=1}^{M^{N_t}} \sum_{p^{(2)}=1}^{M^{N_t}} d_{\mathrm{H}}(b_{p^{(1)}n_t^{(1)}}, b_{p^{(2)}n_t^{(2)}}) \\ \times Q\left(\sqrt{\frac{T}{4N_0}||\mathbf{H}\left(\mathbf{x}_{p^{(1)}} - \mathbf{x}_{p^{(2)}}\right)||_{\mathrm{F}}^2}\right), \end{aligned} \tag{6.9}$$

where $b_{p^{(1)}}$ is the conveyed bit sequence when the message $\mathbf{x}_{p^{(1)}}$ is emitted and $b_{p^{(2)}}$ is the conveyed bit sequence when the signal vector $\mathbf{x}_{p^{(2)}}$ is emitted. For instance, assuming $P_t = 1$, $N_t = 4$ and $M = 2$, the bit sequence "0 0 0 1" is assigned to the transmitted signal vector $\mathbf{x}_2 = [0\ 0\ 0\ 2]^T$ and the bit sequence "1 1 1 0" is assigned to $\mathbf{x}_{16} = [2\ 2\ 2\ 0]^T$, resulting in a Hamming distance $d_{\mathrm{H}}(b_2, b_{16})$ equal to 4. Since in SMP more than one LED can be active during a symbol period, the optical power must be equally distributed across all N_t emitters to ensure that SMP and SM are compared at the same mean output optical power. Thus, in fair comparison context, the transmitted signal vectors $\mathbf{x}_2$ and $\mathbf{x}_{16}$ would respectively become $[0\ 0\ 0\ \frac{1}{2}]^T$ and $[\frac{1}{2}\ \frac{1}{2}\ \frac{1}{2}\ 0]^T$.

6.3 Imaging vs non-imaging receiver

Receivers in MIMO can be of the imaging or of the non-imaging type. The difference between the two is illustrated in Fig. 6.1. In the former, an optical system is placed in front of the PDs array. Typically it consists of a single imaging lens whose role is to separate the light beams originating from different locations and redirect them, thus producing distinct spots (or images) onto the receiver plan. In other words, the imaging receiver can be seen as a hardware tool to decorrelate the signals emitted by the different transmit LEDs and thus mitigate the inter-channel interference (ICI) in a MIMO VLC system. In

the non-imaging case, separate non-imaging lenses, also referred to as concentrators, are placed in front of each receiver. Unlike the imaging lens, the non-imaging system does not form an image of the source, but aims solely at concentrating the light onto the PD surface.

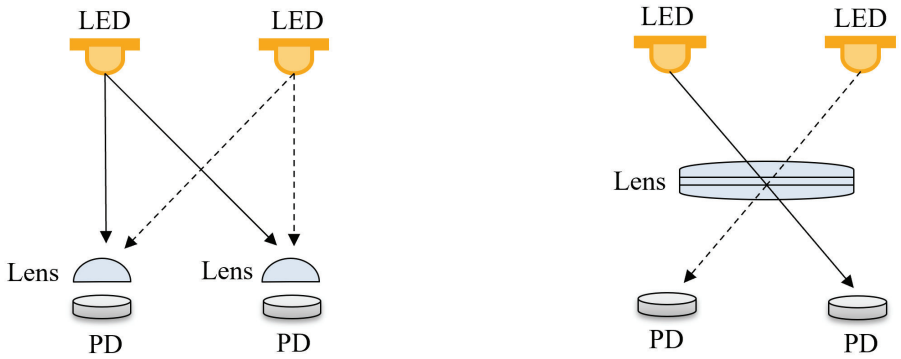

(a) (b)

Figure 6.1 Schematic of (a) non-imaging receiver and (b) imaging receiver.

Table 6.1 4×4 MIMO system simulation parameters

Parameter	Value
PD responsivity R	1
PD active surface A	1 mm^2
LED semi-angle $\theta_{\frac{1}{2}}$	55°
Field-of-view (FOV)	70°
Distance between LEDs	2.5 m
Distance between PDs	0.1 m

In order to evaluate the impact of the imaging receiver, the BER performance of SMP and SM is investigated theoretically and numerically at a spectral efficiency of 4 bit/s/Hz for the non-imaging and imaging case in a 4×4 configuration. The environment considered here is a typical room of size $5 \times 5 \times 3$ m^3, and the layout of the LED lamps is shown in Fig. 6.2. The distance between the transmit LEDs is set to 2.5 m to provide sufficiently wide illumination in the room and the distance between the PDs is 10 cm so that they could easily fit in a compact receiver. The receiver is placed in the center of the room at height of 0.75 m, so that the coordinates of PD1, PD2, PD3 and PD4 are respectively (2.55,2.45,0.75), (2.45,2.45,0.75), (2.45,2.55,0.75) and (2.55,2.55,0.75). The key parameters

selected for simulation are shown in Table 6.1 and the resulting 4×4 channel matrix $\mathbf{H}_{\mathrm{NImR}}$ in the non-imaging case is given by

$$\mathbf{H}_{\mathrm{NImR}} = 10^{-7} \times \begin{bmatrix} 0.2715 & 0.2542 & 0.2542 & 0.2385 \\ 0.2542 & 0.2715 & 0.2385 & 0.2542 \\ 0.2542 & 0.2385 & 0.2715 & 0.2542 \\ 0.2385 & 0.2542 & 0.2542 & 0.2715 \end{bmatrix}. \tag{6.10}$$

For a fair comparison, it is assumed that the imaging system receives the same amount of flux, i.e. the same received optical power as the non-imaging receiver. Therefore the channel matrix $\mathbf{H}_{\mathrm{ImR}}$ can be expressed as

$$\mathbf{H}_{\mathrm{ImR}} = 10^{-7} \times \begin{bmatrix} 0.2546 & 0 & 0 & 0 \\ 0 & 0.2546 & 0 & 0 \\ 0 & 0 & 0.2546 & 0 \\ 0 & 0 & 0 & 0.2546 \end{bmatrix}. \tag{6.11}$$

A useful metric to assess the similarity between the channel gains is the condition number of the channel matrix which is defined as the ratio of the largest singular value of that matrix to the smallest singular value. The condition number of the matrix given in (6.10) is equal to 636.5 and the condition number of the channel matrix in (6.11) is 1. Therefore, it is expected that using an imaging receiver can significantly improve the system performance. The performance is plotted against the SNR in Fig. 6.3, defined as $\frac{R^2 {P_r}^2}{\sigma^2}$, where σ^2 is the noise variance and P_r is the average received optical power defined as $P_r = \frac{1}{N_r} \sum_{i=1}^{N_r} \sum_{j=1}^{N_t} h_{ij} P_t$. The PD responsivity R is assumed to be 1 without loss of generality. It can be observed that at a BER of 10^{-3} SMP with imager performs ~ 36 dB better compared to the non-imaging SMP system and SM with imaging receiver provides a gain of ~ 16 dB compared to the non-imaging case. Moreover, SMP and SM exhibit similar performance when an imaging receiver is employed with a slight advantage of ~ 1.4 dB for the former at a BER of 10^{-3}. Another observation that can be drawn from the same figure is the better performance of SM compared to SMP when both techniques are used without an imager. This is explained by the fact that in SM only one LED is active

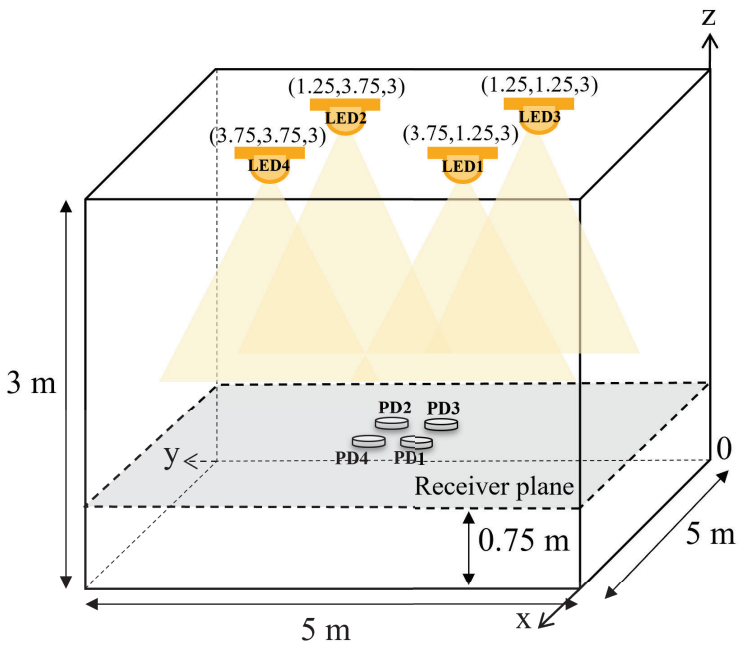

Figure 6.2 Indoor MIMO VLC system configuration in a typical room of size $5 \times 5 \times 3$ m^3.

during a symbol duration while the others are turned off, thus providing more robustness against channel correlation compared to SMP.

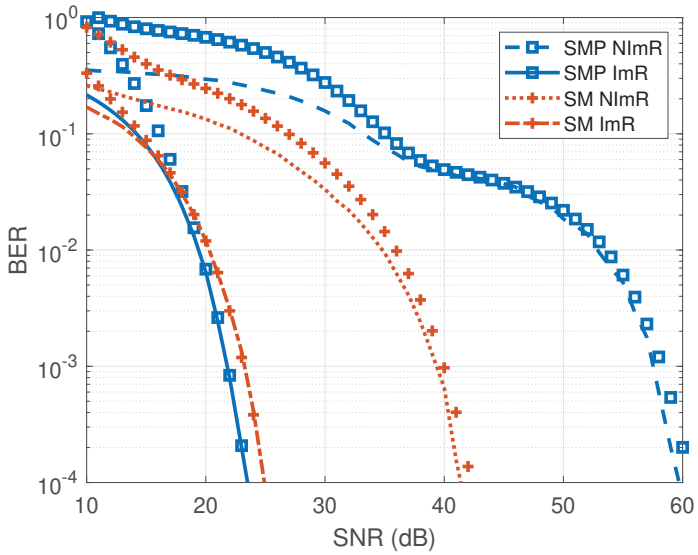

Figure 6.3 BER of SMP and SM using imaging receiver (ImR) and non-imaging receivers (NImR) for spectral efficiency of 4 bit/s/Hz. The Markers show the theoretical error upper bound and the lines show the simulation results.

Despite the significantly improved performance of MIMO imaging systems over non-imaging systems, one major drawback of the imager is user mobility. In fact, the communication link quality can be drastically degraded when the user is moving, i.e, when the imager is misaligned with respect to the the transmit LEDs. Therefore, the remainder of this chapter is dedicated to the investigation of the performance of MIMO techniques with imager misalignment.

6.4 MIMO test bench presentation

In this section, we present a 2×2 VLC test bench with realistc indoor distances based on typical low-cost components (white LEDs and PDs) and an imaging lens to separate the transmitted streams at the receiver.

6.4.1 Transmitter

The transmitter consists of two commercially-available white LEDs (Lumiled LUXEON 3020) with a color temperature of 3000 K. The transmit LEDs are fed by custom drivers that provide a DC bias current to ensure that the modulated current is unipolar and set the illumination level (Fig. 6.4 (a) and (b)).

6.4.2 Receiver

The imaging receiver consists of a single bi-convex lens placed in front of two low-cost silicon PIN PDs (OSRAM SFH-2400) with a 1 mm^2 active area (Fig. 6.4 (b) and (c)). The imaging lens separates the light beams by creating distinct spot images on the active areas of the PDs (Fig. 6.5). As a result, the off-diagonal elements in (6.2) are null and the diagonal elements (h_{11} and h_{22}) are decoupled subchannels. The imaging lens is a 50.8 mm diameter Thorlabs N-BK7 uncoated bi-convex lens (LB1630) with a focal length f_l = 100 mm. The incident light is converted by the PD into an electrical photocurrent, and the latter is converted into a measurable voltage by a TIA. Furthermore, the magnification factor of the system is determined by the thin lens equation, such that

$$\alpha_M = \frac{f_l}{f_l - u} = -\frac{d_r}{d_t} = -\frac{v}{u} \quad , \tag{6.12}$$

where d_t is the distance between the LEDs, d_r is the distance between the PDs, f_l is the focal length, u is the distance from the object to the lens, v is the distance from the lens to the image and α_M is the magnification factor. In our implementation, we chose to set the distance of the VLC link to $u = 2.25$ m, which corresponds to a realistic distance from the ceiling to the desktop level in a typical room. The distance between the two LEDs is set to d_t=40 cm, as it is a typical spacing distance between LEDs in a LED-based light

fixture. From (6.12), the distance between the PDs is determined to be $d_r = 1.9$ cm, while v =10.46 cm, and $\alpha_M = -0.047$. The spacing distance between the photodiodes in focal plane of receiver is chosen to enable integration in a compact system. Note, the optical parameters are interrelated and have a strong impact on the link geometry. Therefore, further investigation could be done on the imaging optical system to improve the compactness of the receiver, e.g. using a lens with smaller focal length.

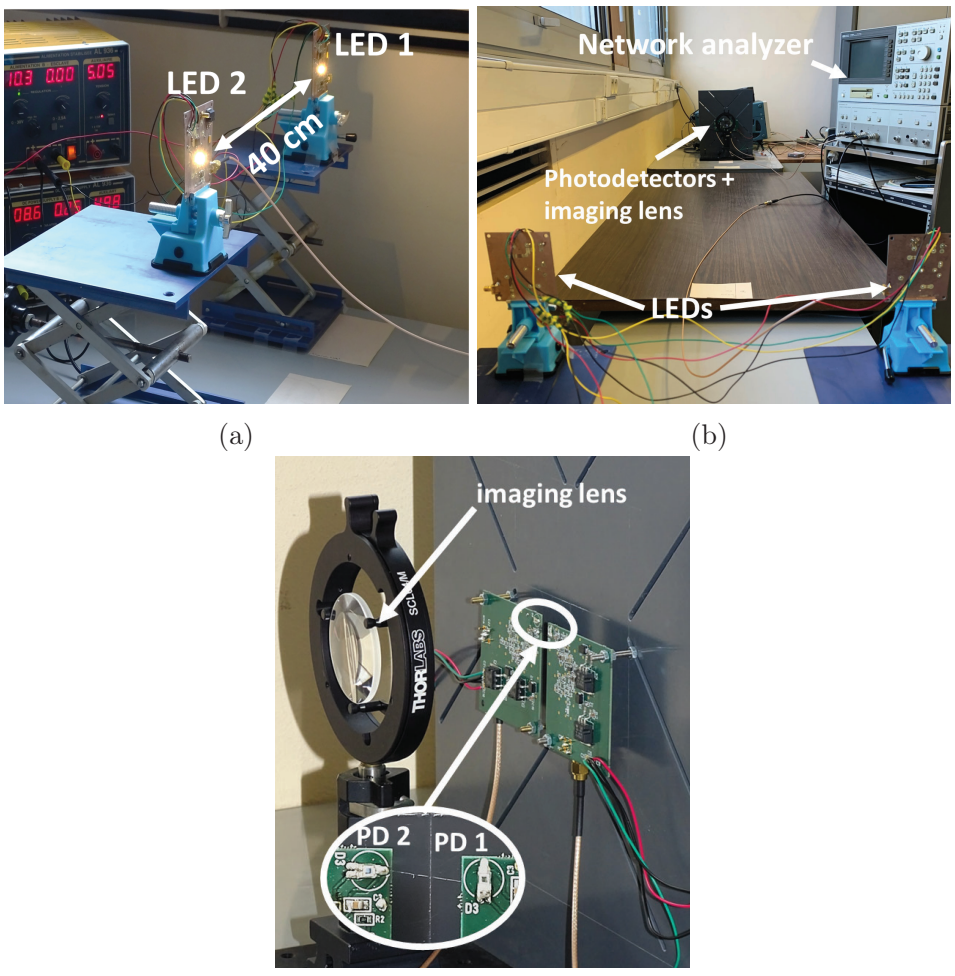

(a) (b)

(c)

Figure 6.4 Experimental MIMO setup: (a) transmitter, (c) receiver and (b) complete link.

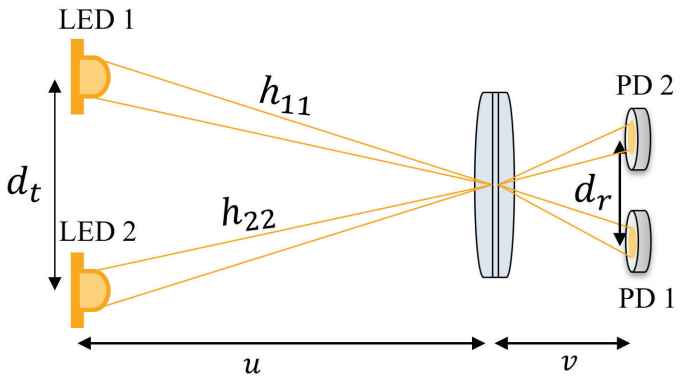

Figure 6.5 Experimental 2×2 MIMO setup with imager.

6.5 Lighting function

The LUXEON 3020 LED outputs a limited luminous flux of 53 lm. The same LED device was employed in Chapter 3 and it was concluded that a luminaire made of 134 such LEDs and delivering a total luminous flux of 7078 lm would be required to achieve a horizontal luminance of 500 lux at the receiver unit, which is the brightness level recommended by European standard EN 12464-1 for lighting of indoor work places [17]. However, luminaires often come with a diffuser, which is incompatible with an imaging receiver. Another way to achieve sufficient illumination is to employ LED spotlights used for indoor illumination which comprise multiple mid-power LED chips to facilitate thermal dissipation, and commonly output a total luminous flux of several hundreds of lumens. In practice, several LED spotlights could be arranged on a ceiling so that the horizontal luminance of each spotlight would add up to the total horizontal luminance at the desired location. In addition, given the magnification factor α_M of -0.047, a circular light source of diameter up to 2.1 cm could be focused onto the 1 mm^2 area of the PIN PD. Thus, ten 3020 LEDs could fit in a single LED spotlight which would yield a luminous flux of 530 lm.

6.6 Channel DC gain measurement and impact of imager misalignment

To assess the impact of imager misalignment, the receiver (lens and PDs) is laterally displaced by an offset Δd from the center line (Fig. 6.6). The received light spots are then slightly shifted with respect to the PDs due to the angle of incidence on the surface of the lens (Fig. 6.6). In practice, no light falls onto the PDs areas when Δd is in the order of several millimeters, preventing any communication between the transmitter and the receiver. A "smart" receiver would compensate either mechanically (moving the PDs) or electrically (choosing the right PDs in a larger matrix) in order to realign itself with

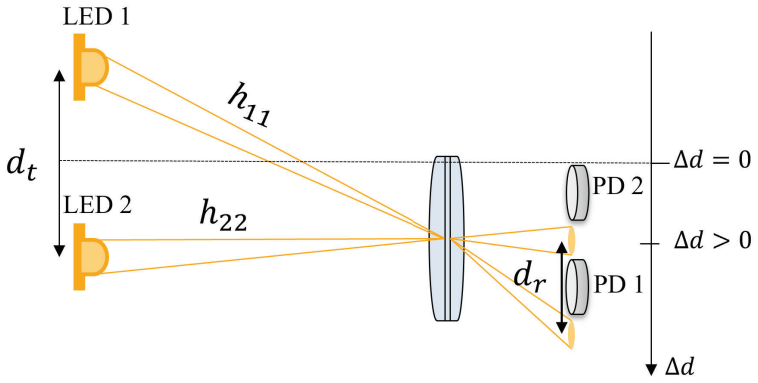

Figure 6.6 Schematic of the experimental 2×2 MIMO setup with imager misalignment.

the light spots. To emulate this, the PDs were manually and independently adjusted for each value of Δd.

The channel DC gains were measured using a network analyzer (HP-4195A) at low frequencies within the 3-dB bandwidth of the LED (same gain as DC). The results for various values of Δd up to 80 cm are presented in Fig. 6.7. For $\Delta d \leq 20$ cm, both gains remain stable. Above 20 cm, however, channel gains monotonically decrease with increasing Δd. The loss is mostly due to the light spots becoming elongated and less concentrated on the PD surface. It follows that the lateral asymmetric geometry results in one gain falling faster than the other. This could be avoided if the receiver could rotate itself towards the source of light.

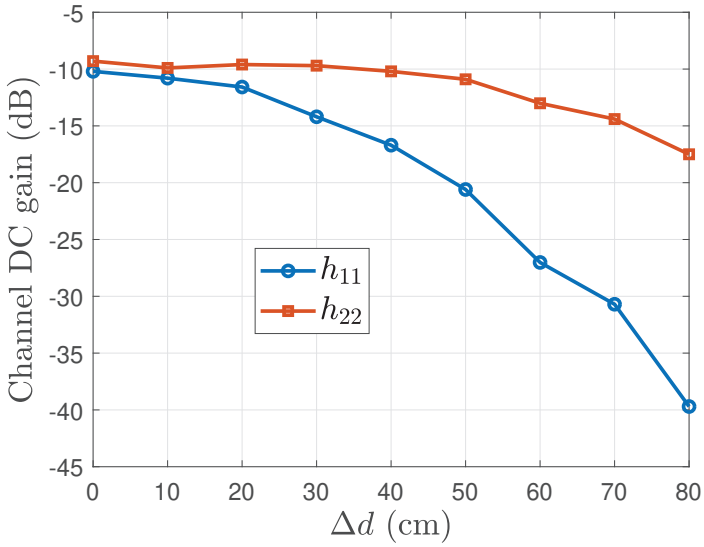

Figure 6.7 Measured channel DC gains h_{11} and h_{22} for various values of Δd.

6.7 Performance of MIMO techniques

6.7.1 Comparison of SMP and SM

BER performance of SMP and SM was evaluated through simulations incorporating channel measurements from Section 6.6. Performance is assessed at the same spectral efficiency and for two values of Δd (0 cm and 70 cm). Results are plotted in Figs. 6.8 and 6.9 against the SNR. It can be observed that SMP outperforms SM by about 3 dB and 7 dB at 4 bit/s/hz and 6 bit/s/Hz, respectively. In fact, for the same spectral efficiency, a higher constellation order is required for SM to operate compared to SMP. Therefore, the distance between received symbols is lower for the former, which significantly degrades the BER. For instance, at a spectral efficiency of 6 bit/s/Hz, the PAM constellation order is $M = 8$ for SMP and $M = 32$ for SM. Reducing the constellation size in SM would require a larger number of transmit LEDs, with the associated implementation complexity.

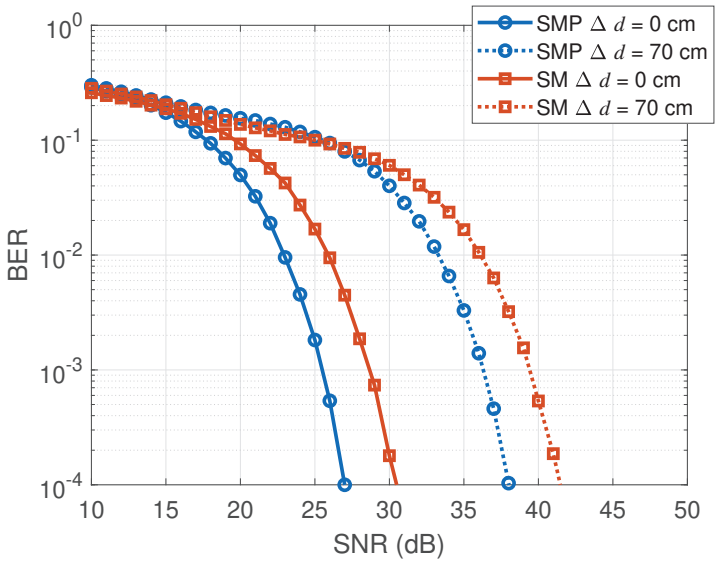

Figure 6.8 BER performance of SMP and SM for $\Delta d = 0$ cm and $\Delta d = 70$ cm at a spectral efficiency of 4 bit/s/Hz.

6.7.2 Bit loading in SMP

As shown in Section 6.6, channel gains can significantly differ if the receiver is displaced ($\Delta d \neq 0$). Therefore, a technique can be deployed with knowledge of the channel state information at the transmitter to adapt the constellation size on each sub-channel and therefore improve link reliability, while maintaining a constant spectral efficiency.

At $\Delta d = 70$ cm, the channel matrix $\mathbf{H}$ can be written as follows:

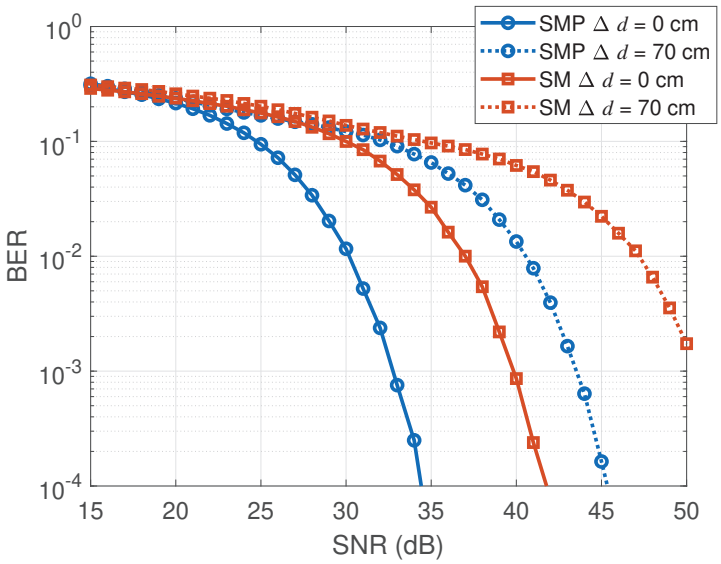

Figure 6.9 BER performance of SMP and SM for $\Delta d = 0$ cm and $\Delta d = 70$ cm at a spectral efficiency of 6 bit/s/Hz.

$$\mathbf{H} = \begin{bmatrix} 0.0292 & 0 \\ 0 & 0.1905 \end{bmatrix}. \tag{6.13}$$

To assess the potential of bit loading for this specific scenario, we manually select modulation orders independently for each subchannel while aiming for a fixed spectrum efficiency of 4 bit/s/Hz. Thus, LED 1 and LED 2 transmit a PAM signal of modulation order $M1 = 2$ and $M2 = 8$, respectively. The BER performance of the adaptive SMP technique is then compared with that of the conventional SMP (where the same constellation size $M = 4$ is used for each transmit LED) and the results are shown in Fig. 6.10. It can be seen that adaptive SMP provides a small improvement of 2.2 dB at a BER of 10^{-3} over conventional SMP when $\Delta d = 50$ cm. For $\Delta d = 70$ cm and $\Delta d = 80$ cm, however, adaptive SMP yields an advantage of 8.5 dB and 9.5 dB, respectively. It can be concluded that adaptively adjusting modulation orders would yield a significant gain.

6.8 Chapter summary

In this chapter, the performance of two MIMO techniques, namely SMP and SM were analyzed theoretically and by simulation with imaging and non-imaging receivers. It was concluded that MIMO imaging systems offer significantly better performance compared to non-imaging systems. As a second step, a 2×2 MIMO VLC test bench with imaging lens

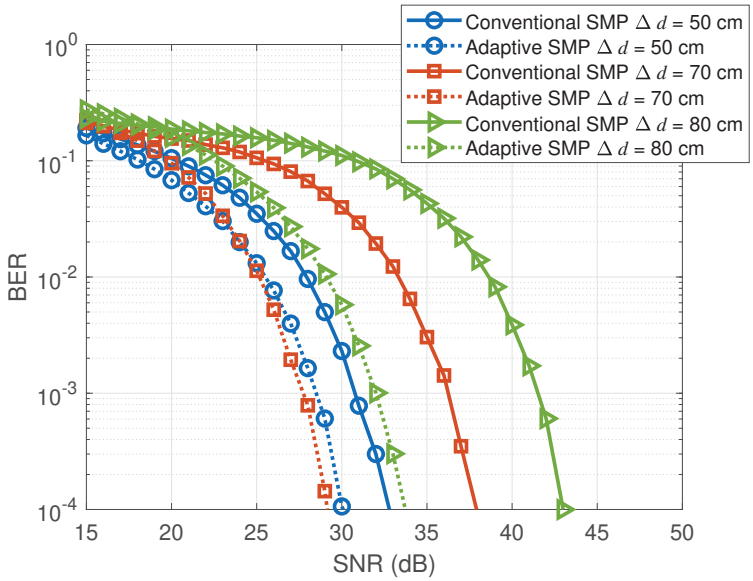

Figure 6.10 BER performance of adaptive SMP and conventional SMP for various values of Δd at a spectral efficiency of 6 bit/s/Hz.

was presented. Channel measurements were performed reflecting a geometry, distance, and component choices compatible with low-cost white LED luminaires, typical office environments, and recommended lighting levels. As part of these measurements, the impact of displacing the receiver (misalignment) was assessed. Using the measured channels, the BER performance of SM and SMP was compared at fixed spectral efficiencies, with SMP exhibiting superior performance. Misalignment was seen to induce significant loss (up to 12 dB), which can be partially compensated by some form of adaptive modulation.

CHAPTER 7

LU polynomial matrix decomposition

7.1 Introduction

In MIMO VLC systems, the signals emitted by multiple transmit light sources overlap at each receive PD, causing inter-channel interference (ICI), which systematically occurs and cannot be neglected, but can be mitigated by employing an imaging lens at the receiver for instance, as explained in the previous chapter. In addition to ICI, inter-symbol interference (ISI) may be encountered in MIMO VLC when the difference in optical path lengths between the different emitters and the receiver is significant with respect to the symbol period [45]. In most research works on MIMO VLC, there is no significant difference between the optical path delays, as the considered environment is typically a small office room. In addition, the system is highly bandlimited due to the narrow modulation bandwidth of the light sources, e.g. the LEDs,

Nevertheless, recent research works have demonstrated the benefits of using laser diodes (LDs) sources for joint illumination and data communication, as they exhibit a very high modulation bandwidth in the GHz range. This type of transmitter is expected to unlock the use of large signal modulation bandwidths. When LDs are employed at high data rate in large indoor space scenarios such as convention centers, shopping malls, factories, lecture halls or airports, the difference in optical path lengths becomes significant with respect to the symbol period and thus the aforementioned ISI can degrade the system performance. Moreover, the greater the signal bandwidth, the more severe the ISI.

In this chapter, we propose an effective decomposition technique referred to as lower-upper polynomial matrix decomposition (LU-PMD) for wideband MIMO VLC systems in large space indoor scenarios that completely cancels the ICI (without an imaging receiver) and reduces the MIMO channel into independent SISO additive noise channels, thereby avoiding the ISI. As a result, the LU-PMD method enables the use of SMP with larger modulation bandwidth, hence higher achievable throughput. This technique was originally proposed in [84] for RF MIMO systems and named unimodular-uppper polynomial matrix decomposition, and finally later renamed LU-PMD in [86]. Therefore, an adaptation of LU-PMD to MIMO VLC systems is proposed here, taking into account the constraints of

VLC systems such as the optical wireless channel and the limited dynamic range of the LDs.

The remainder of this chapter is organized as follows: in Section 7.2, the polynomial matrix model is presented. Then, in Section 7.3, the source of ISI in large indoor space environments is highlighted with simulations. In Section 7.4, the principle of LU-PMD is presented, followed by an example of application for a 4×4 MIMO VLC system. Then, SMP technique with LU-PMD is studied in Section 7.5. Lastly, Section 7.6 concludes the chapter.

7.2 Polynomial matrix model of wideband MIMO channel

Due to the different arrival times of optical signals at the receiver, the wideband MIMO channel establishing the link between the transmitter and the receiver can be described by a representation model in space and time. It follows that a MIMO system with N_r receive PDs and N_t transmit LDs can be modeled with a polynomial channel matrix $\mathbf{H}(z) \in \mathbb{R}^{N_r \times N_t}$ defined as

$$\mathbf{H}(z) = \begin{bmatrix} h_{11}(z) & \dots & h_{1N_t}(z) \\ \vdots & \ddots & \vdots \\ h_{N_r1}(z) & \dots & h_{N_rN_t}(z) \end{bmatrix}, \tag{7.1}$$

where the polynomial matrix coefficient $h_{n_rn_t}(z)$ located at the n_r-th row and the at the n_t-th column represents the z-transform of the discrete-time CIR between LD n_t and PD n_r. This coefficient can be expressed as follows:

$$h_{n_rn_t}(z) = \sum_{l=0}^{L-1} h^l_{n_rn_t} z^{-l}, \tag{7.2}$$

$h^l_{n_rn_t}$ being the impulse response sampled at the l-th delay and L being the number of samples, i.e. the total number of time delays in the discrete-time CIR. Note, z^{-1} represents the unit time delay. Under the assumption that the signal bandwidth is significantly smaller than the front-end optical components 3-dB bandwidth, the CIR solely comprises the channel DC gain, which was defined earlier in (2.10). It should be noted that (2.10) is a Dirac delta function weighted by the channel DC gain and shifted by an amount of time

equivalent to the signal propagation delay, whereas (7.2) is a discrete representation where the DC gain is associated with a delay in the indeterminate z. The polynomial form of the MIMO channel matrix can be contrasted with other studies in classical environments (small office rooms) where a scalar matrix is sufficient to model the MIMO channel. In this case, a polynomial decomposition is not necessary.

7.3 ISI in large indoor space scenario

In this section, the ISI stemming from the successive arrivals of signals emitted by the different LDs is described. We consider a large indoor space scenario of size $9 \times 9 \times 6$ m^3 with four transmit LDs and four PDs (Fig. 7.1). The receiver is located at coordinates (5;3;0.75) and the distance between PDs is 20 cm. LDs combined with diffusers are assumed to have a Lambertian radiation pattern with a semi-angle at half luminance equal to 60°. It is assumed that a direct path exists between the transmitter and the receiver and therefore multipath propagation due to the reflections of light on walls, floor or objects in the room is not considered as their contribution to the total received optical power is negligible (see Section 2.5.6).

Let us first focus on the sum of CIRs between all LDs and PD1, which can be expressed as $h_1(z) = h_{11}(z) + h_{12}(z) + h_{13}(z) + h_{14}(z) = 1 + 0.2806z^{-8} + 0.1873z^{-11} + 0.0978z^{-17}$, and is represented in Fig. 7.2. A bar chart is employed to represent the normalized amplitudes of the coefficients of each polynomial element. Moreover, the system baud rate is assumed to be 300 Mbaud and the upsampling factor is chosen as 4, yielding a temporal resolution, or sampling time, equal to 0.83 ns. It can be observed that the time delay difference between signals emitted by LD1 and LD3 is 6.67 ns, which is larger than the symbol period equal to 3.33 ns. Therefore, the received signal on PD1 is expected to be corrupted by other time-delayed signals, and by extension the same naturally applies to the other PDs. Furthermore, the combined normalized amplitude of the CIR $h_{12}(z)$, $h_{13}(z)$ and $h_{14}(z)$ represents 57 % of that of $h_{11}(z)$. From there, it becomes clear that employing more transmit LDs and / or increasing the data rate will result in more severe ISI. In addition, the severity of the performance degradation may also depend on the user location.

7.4 Principle of LU-PMD

A Closed-Loop MIMO system is considered here. It is assumed that the transmitter and the receiver have perfect knowledge of the channel state information (CSI) at all times. In practice, the channel would be estimated at the receiver using conventional channel estimation techniques and the CSI would be sent to the transmitter via feedback [68, 40].

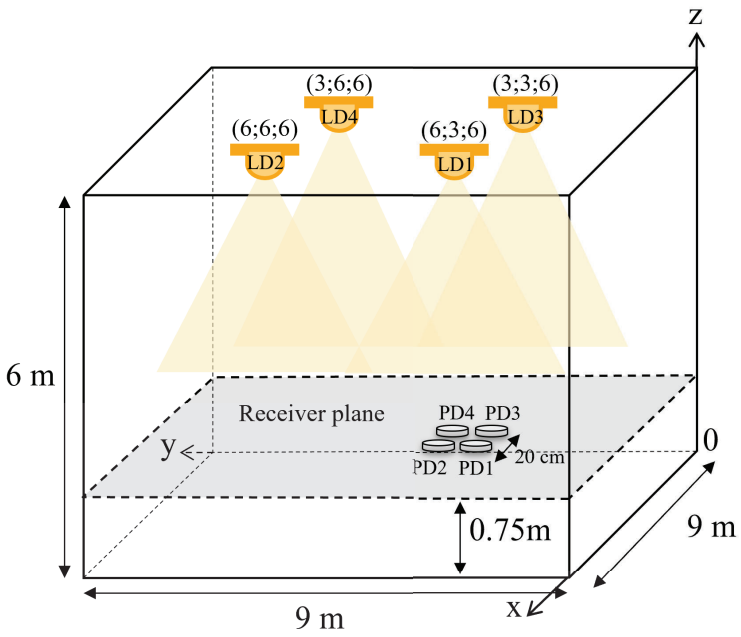

Figure 7.1 Indoor VLC system configuration in a large indoor environment.

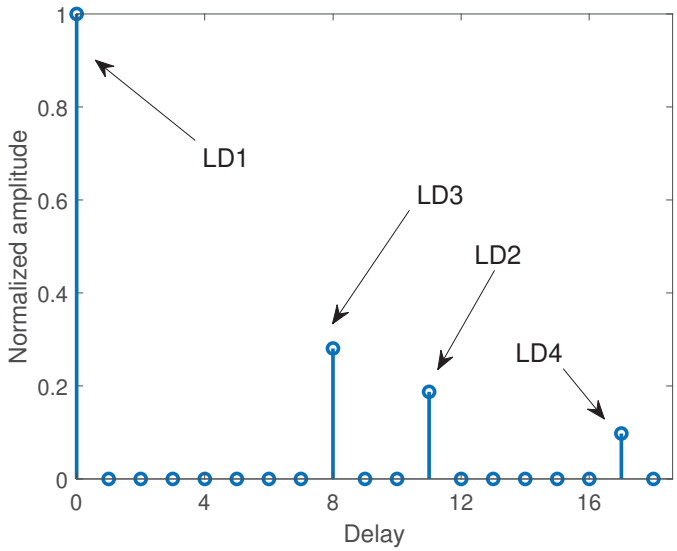

Figure 7.2 Time representation of the coefficients of the sum of CIRs between all LDs and PD1

The proposed LU-PMD algorithm combines the classical Smith form and the LU factorization method (Gauss elimination) and performs a factorization of the channel matrix under the form $\mathbf{H}(z) = \mathbf{U}(z)\mathbf{D}(z)\mathbf{V}(z)$, where $\mathbf{D}(z)$ is a diagonal polynomial matrix and $\mathbf{U}(z)$ and $\mathbf{V}(z)$ are simple unimodular polynomial matrices that can easily be inverted.

The LU-PMD algorithm performs the decomposition in two key steps: 1) A reduction step which aims at reducing a given diagonal element to the greatest common divisor of all the polynomial entries below the said diagonal element, and 2) a Gaussian elimination step which zeroes the entries below the diagonal elements of the matrix. First, the decomposition is applied to $\mathbf{H}(z)$ and the above-mentioned steps are repeated until a triangular superior matrix $\mathbf{R}(z)$ and a unimodular matrix $\mathbf{U}(z)$ are obtained such that $\mathbf{H}(z) = \mathbf{U}(z)\mathbf{R}(z)$. Then, the decomposition is applied a second time to $\mathbf{R}^T(z)$ which yields after factorization $\mathbf{R}^T(z) = \mathbf{V}^T(z)\mathbf{D}(z)$. The LU-PMD algorithm was described for a general case in [85]. In the next part, we will present an example of application of the LU-PMD technique for a 4×4 MIMO system.

7.4.1 Application of LU-PMD to a 4×4 MIMO system

Preliminary: the Bezout identity

First and foremost, explanations need to be given regarding the Bezout identity. The latter is an existence statement given below.

Bezout identity: For two polynomials $a(z)$ and $b(z)$, let $d(z)$ be the greatest common divisor (GCD) of $a(z)$ and $b(z)$ such that $d(z) = \gcd(a(z), b(z))$. Then, there exist polynomials $a^\sharp(z)$ and $b^\sharp(z)$ such that

$$a(z)a^\sharp(z) + b(z)b^\sharp(z) = d(z). \tag{7.3}$$

with $\deg(a^\sharp(z)) \leq \deg(a(z))$ and $\deg(b^\sharp(z)) \leq \deg(b(z))$. If the GCD $d(z) = 1$, the polynomial pair $[a(z), b(z)]$ is said to be irreducible. Equivalently, the polynomials of the said pair are mutually prime.

LU-PMD algorithm

The LU-PMD algorithm follows a two-stage process: 1) reduction, 2) Gaussian elimination. Let us first consider the decomposition of $\mathbf{H}(z)$ which is a 4×4 polynomial matrix written as

$$\mathbf{H}(z) = \begin{bmatrix} h_{11}(z) & h_{12}(z) & h_{13}(z) & h_{14}(z) \\ h_{21}(z) & h_{22}(z) & h_{23}(z) & h_{24}(z) \\ h_{31}(z) & h_{32}(z) & h_{33}(z) & h_{34}(z) \\ h_{41}(z) & h_{42}(z) & h_{43}(z) & h_{44}(z) \end{bmatrix}. \tag{7.4}$$

1) Reduction step: let us first consider the polynomial pair $[h_{11}^{\sharp}(z),h_{21}^{\sharp}(z)]$ solving the Bezout identity such that

$$h_{11}(z)h_{11}^{\sharp}(z) + h_{21}(z)h_{21}^{\sharp}(z) = d_1(z), \tag{7.5}$$

where $d_1(z)$ is the GCD of the pair $[h_{11}(z),h_{21}(z)]$. The matrix $\overline{\mathbf{A}}_{\mathbf{1}}(z)$ is then constructed with the elements of the Bezout identity such that

$$\overline{\mathbf{A}}_{\mathbf{1}}(z) = \begin{bmatrix} h_{11}^{\sharp}(z) & h_{21}^{\sharp}(z) & 0 & 0 \\ -h_{21}(z) & h_{11}(z) & 0 & 0 \\ 0 & 0 & 1 & 0 \\ 0 & 0 & 0 & 1 \end{bmatrix}. \tag{7.6}$$

Multiplying $\mathbf{H}(z)$ on the left by $\overline{\mathbf{A}}_{\mathbf{1}}(z)$ yields a new matrix $\widetilde{\mathbf{H}}_{\mathbf{1}}(z)$ which is expressed as

$$\widetilde{\mathbf{H}}_{\mathbf{1}}(z) = \begin{bmatrix} d_1(z) & \tilde{h}_{12}(z) & \tilde{h}_{13}(z) & \tilde{h}_{14}(z) \\ 0 & \tilde{h}_{22}(z) & \tilde{h}_{23}(z) & \tilde{h}_{24}(z) \\ h_{31}(z) & h_{32}(z) & h_{33}(z) & h_{34}(z) \\ h_{41}(z) & h_{42}(z) & h_{43}(z) & h_{44}(z) \end{bmatrix}. \tag{7.7}$$

At this point of the algorithm, two cases are considered:

Case 1: the pair of polynomials $[h_{11}(z), h_{21}(z)]$ is irreducible and we have $d_1(z) = 1$. In other words, its GCD is equal to 1 and those two polynomials are said to be mutually prime. This is the simplest case, because the iteration continues the Gaussian elimination step 2) described further in the text.

Case 2: the pair of polynomials $[h_{11}(z), h_{21}(z)]$ is **not** irreducible, i.e. the GCD $d_1(z)$ is not a constant. In this case, one can repeat the reduction step process, this time with the polynomial pair $[d_1(z), h_{31}(z)]$. The matrices $\overline{\mathbf{A}}_{\mathbf{1}}(z)$ and $\widetilde{\mathbf{H}}_{\mathbf{1}}(z)$ can be re-expressed as $\overline{\mathbf{A}}_{\mathbf{1,0}}(z)$ and $\widetilde{\mathbf{H}}_{\mathbf{1,0}}(z)$, respectively. An intermediate matrix $\overline{\mathbf{A}}_{\mathbf{1,1}}(z)$ is built with the elements of the Bezout identity $d_1(z)d_1^{\sharp}(z) + h_{31}(z)h_{31}^{\sharp}(z) = d_2(z)$ such that

$$\overline{\mathbf{A}}_{\mathbf{1},\mathbf{1}}(z) = \begin{bmatrix} 1 & 0 & 0 & 0 \\ 0 & d_1^\sharp(z) & h_{31}^\sharp(z) & 0 \\ 0 & -h_{31}(z) & d_1(z) & 0 \\ 0 & 0 & 0 & 1 \end{bmatrix}, \tag{7.8}$$

and the multiplication of $\widetilde{\mathbf{H}}_{\mathbf{1},\mathbf{0}}(z)$ on the left by $\overline{\mathbf{A}}_{\mathbf{1},\mathbf{1}}(z)$ will yield a matrix $\widetilde{\mathbf{H}}_{\mathbf{1},\mathbf{1}}(z)$ whose element in the first row and first column is the GCD of the pair $[d_1(z), h_{31}(z)]$, denoted $d_2(z)$, and the element in the third row and first column is 0. As a result, This process can be repeated with $\widetilde{\mathbf{H}}_{\mathbf{1},\mathbf{1}}(z)$ and the remaining polynomial elements below the diagonal element, with the objective of finding a polynomial pair that is irreducible and with a GCD equal to 1. For example, if the latter condition is never met, we have $\overline{\mathbf{A}}_{\mathbf{1}}(z) = \overline{\mathbf{A}}_{\mathbf{1},\mathbf{2}}(z)\overline{\mathbf{A}}_{\mathbf{1},\mathbf{1}}(z)\overline{\mathbf{A}}_{\mathbf{1},\mathbf{0}}(z)$ and $\mathbf{H}_{\mathbf{1}}(z) = \overline{\mathbf{A}}_{\mathbf{1}}(z)\mathbf{H}(z)$, where all the elements $\mathbf{H}_{\mathbf{1}}(z)$ below the first diagonal element are 0.

For the sake of simplicity and to demonstrate the algorithm in its entirety, we assume in what follows that the initial polynomial pair $[h_{11}(z), h_{21}(z)]$ is irreducible and that $d_1(z) = 1$. Therefore, the decomposition process continues now with the Gaussian elimination.

2) Gaussian elimination: the second step of the LU-PMD algorithm is the Gaussian elimination which is performed to zero the remaining elements under the diagonal element of the first column of $\widetilde{\mathbf{H}}_{\mathbf{1}}(z)$ given by (7.7). This operation is possible only if the diagonal element resulting from the prior reduction step is equal to 1. First, the matrix $\overline{\mathbf{L}}_{\mathbf{1}}(z)$ is defined as:

$$\overline{\mathbf{L}}_{\mathbf{1}}(z) = \begin{bmatrix} 1 & 0 & 0 & 0 \\ 0 & 1 & 0 & 0 \\ -h_{31}(z) & 0 & 1 & 0 \\ -h_{41}(z) & 0 & 0 & 1 \end{bmatrix}, \tag{7.9}$$

and the matrix $\mathbf{H}_{\mathbf{1}}(z) = \overline{\mathbf{L}}_{\mathbf{1}}(z)\widetilde{\mathbf{H}}_{\mathbf{1}}(z)$ is expressed as

$$\mathbf{H_1}(z) = \begin{bmatrix} 1 & \tilde{h}_{12}(z) & \tilde{h}_{13}(z) & \tilde{h}_{14}(z) \\ 0 & \tilde{h}_{22}(z) & \tilde{h}_{23}(z) & \tilde{h}_{24}(z) \\ 0 & \tilde{h}_{32}(z) & \tilde{h}_{33}(z) & \tilde{h}_{34}(z) \\ 0 & \tilde{h}_{42}(z) & \tilde{h}_{43}(z) & \tilde{h}_{44}(z) \end{bmatrix}. \tag{7.10}$$

The algorithm repeats for all columns of $\mathbf{H_1}(z)$. In order to present the more complete case as an example (i.e. without early simplifications), it is assumed in the following steps for the other columns that polynomial pairs are irreducible. Assuming $\tilde{h}_{22}(z)$ and $\tilde{h}_{32}(z)$ are mutually prime, their GCD is equal to 1 and it exists a pair of polynomials $[\tilde{h}^{\sharp}_{22}(z),\tilde{h}^{\sharp}_{32}(z)]$ solving the Bezout identity such that

$$\tilde{h}_{22}(z)\tilde{h}^{\sharp}_{22}(z) + \tilde{h}_{32}(z)\tilde{h}^{\sharp}_{32}(z) = 1. \tag{7.11}$$

Then the matrix $\overline{\mathbf{A}}_{\mathbf{2}}(z)$ is constructed such that

$$\overline{\mathbf{A}}_{\mathbf{2}}(z) = \begin{bmatrix} 1 & 0 & 0 & 0 \\ 0 & \tilde{h}^{\sharp}_{22}(z) & \tilde{h}^{\sharp}_{32}(z) & 0 \\ 0 & -\tilde{h}_{32}(z) & \tilde{h}_{22}(z) & 0 \\ 0 & 0 & 0 & 1 \end{bmatrix}. \tag{7.12}$$

Multiplying $\mathbf{H_1}(z)$ by the matrix $\overline{\mathbf{A}}_{\mathbf{2}}(z)$ yields the matrix $\widetilde{\mathbf{H}}_{\mathbf{2}}(z)$ expressed as

$$\widetilde{\mathbf{H}}_{\mathbf{2}}(z) = \begin{bmatrix} 1 & \tilde{h}_{12}(z) & \tilde{h}_{13}(z) & \tilde{h}_{24}(z) \\ 0 & 1 & \breve{h}_{23}(z) & \breve{h}_{24}(z) \\ 0 & 0 & \breve{h}_{33}(z) & \breve{h}_{34}(z) \\ 0 & \tilde{h}_{42}(z) & \tilde{h}_{43}(z) & \tilde{h}_{44}(z) \end{bmatrix}. \tag{7.13}$$

The Gaussian elimination step yields the matrix $\mathbf{H_2}(z)$ defined as $\mathbf{H_2}(z) = \overline{\mathbf{L}}_{\mathbf{2}}(z)\widetilde{\mathbf{H}}_{\mathbf{2}}(z)$

$$\mathbf{H_2}(z) = \begin{bmatrix} 1 & \tilde{h}_{12}(z) & \tilde{h}_{13}(z) & \tilde{h}_{14}(z) \\ 0 & 1 & \breve{h}_{23}(z) & \breve{h}_{13}(z) \\ 0 & 0 & \breve{h}_{33}(z) & \breve{h}_{34}(z) \\ 0 & 0 & \breve{h}_{43}(z) & \breve{h}_{44}(z) \end{bmatrix}, \tag{7.14}$$

where

$$\overline{\mathbf{L}}_{\mathbf{2}}(z) = \begin{bmatrix} 1 & 0 & 0 & 0 \\ 0 & 1 & 0 & 0 \\ 0 & 0 & 1 & 0 \\ 0 & -\tilde{h}_{42}(z) & 0 & 1 \end{bmatrix}, \tag{7.15}$$

Finally the matrix $\overline{\mathbf{A}}_{\mathbf{3}}(z)$ is constructed with the Bezout polynomials and the pair $[\breve{h}_{33}(z)\breve{h}_{43}(z)]$ such that

$$\overline{\mathbf{A}}_{\mathbf{3}}(z) = \begin{bmatrix} 1 & 0 & 0 & 0 \\ 0 & 0 & 0 & 1 \\ 0 & 0 & \breve{h}^{\sharp}_{33}(z) & \breve{h}^{\sharp}_{43}(z) \\ 0 & 0 & -\breve{h}_{43}(z) & \breve{h}_{33}(z) \end{bmatrix}, \tag{7.16}$$

and the multiplication with $\mathbf{H_2}(z)$ yields the upper triangular matrix $\mathbf{R}(z)$, i.e.

$$\mathbf{R}(z) = \overline{\mathbf{A}}_{\mathbf{3}}(z)\mathbf{H_2}(z) = \begin{bmatrix} 1 & \tilde{h}_{12}(z)\tilde{h}_{13}(z)\tilde{h}_{14}(z) \\ 0 & 1 & \breve{h}_{23}(z)\breve{h}_{24}(z) \\ 0 & 0 & 1 & \hat{h}_{34}(z) \\ 0 & 0 & 0 & \hat{h}_{44}(z) \end{bmatrix}. \tag{7.17}$$

Finally, we have

$$\begin{aligned}\mathbf{R}(z) &= \overline{\mathbf{A}}_{\mathbf{3}}(z)\overline{\mathbf{L}}_{\mathbf{2}}(z)\overline{\mathbf{A}}_{\mathbf{2}}(z)\overline{\mathbf{L}}_{\mathbf{1}}(z)\overline{\mathbf{A}}_{\mathbf{1}}(z)\mathbf{H}(z) \\ \mathbf{R}(z) &= \mathbf{U}^{-1}(z)\mathbf{H}(z),\end{aligned} \tag{7.18}$$

where $\mathbf{U}^{-1}(z)$, being unitary, is an easily invertible matrix. The last stage, i.e. the **factorization**, consists in decomposing $\mathbf{H}(z)$ into two factors, such that $\mathbf{H}(z) = \mathbf{U}(z)\mathbf{R}(z)$. Then, applying the LU-PMD algorithm a second time on $\mathbf{R}(z)^T$ performs a complete diagonalization of the channel matrix $\mathbf{H}(z)$

7.4.2 Numerical results

In this section, the LU-PMD technique is applied to the scenario described in Section 7.3. In this scenario, the channel matrix $\mathbf{H}(z)$ with normalized amplitudes can be expressed as

$$\mathbf{H}(z) = \begin{bmatrix} 1 & 0.2806z^{-8} & 0.1873z^{-11} & 0.0977^{-17} \\ 0.9724 & 0.3028^{-8} & 0.185z^{-11} & 0.1022z^{-17} \\ 1 & 0.2806z^{-8} & 0.2018z^{-11} & 0.1031z^{-17} \\ 0.9724 & 0.3028z^{-8} & 0.1993^{-11} & 0.1080z^{-16} \end{bmatrix}. \tag{7.19}$$

Fig. 7.3 (a) shows the matrix for the considered MIMO channel. It is noteworthy that the position of each bar chart block in the figure corresponds to the position of the polynomial element in the channel matrix $\mathbf{H}(z)$. The resulting diagonal matrix $\mathbf{D}(z)$ after LU-PMD is expressed as

$$\mathbf{D}(z) = \begin{bmatrix} 1 & 0 & 0 & 0 \\ 0 & z^{-8} & 0 & 0 \\ 0 & 0 & z^{-11} & 0 \\ 0 & 0 & 0 & \gamma(z) \end{bmatrix}, \tag{7.20}$$

and a representation with bar charts is shown in Fig. 7.3 (b). As expected, ICI is completely eliminated and there is no ISI. The amplitude of the first three diagonal elements is 1 and in this particular case, the coefficients of the second and third elements of $\mathbf{D}(z)$ are delayed by 8 and 11 unit time delays, respectively. The last diagonal element is determined to be $\gamma(z) = -4.66\times10^{-5}z^{-17} + 4.68\times10^{-5}z^{-16}$. Therefore, the last subchannel associated

with the polynomial $\gamma(z)$ suffers from a significantly reduced channel amplitude, in fact negligible with respect to the three other subchannels.

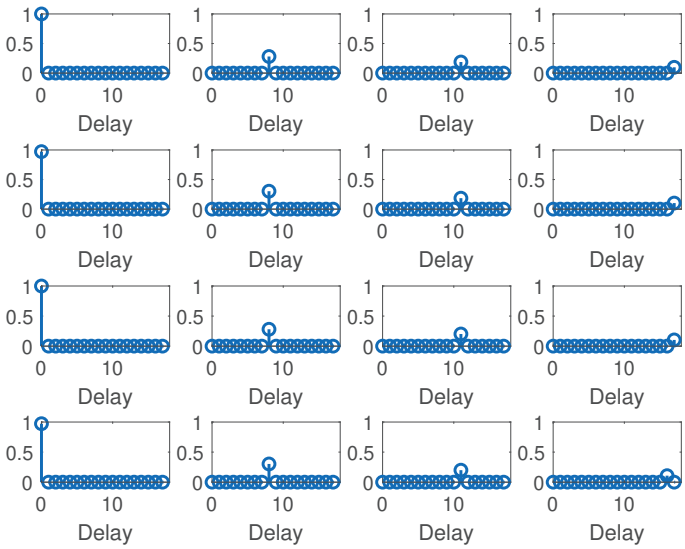

(a)

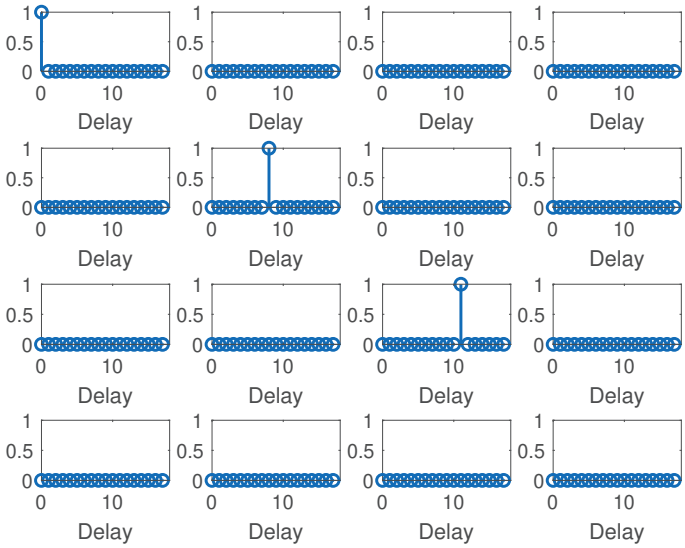

(b)

Figure 7.3 Space-time representation of the coefficients of (a) channel matrix $\mathbf{H}(z)$ and (b) diagonalized matrix $\mathbf{D}(z)$ after LU-PMD.

7.5 SMP with LU-PMD

7.5.1 Principle

In the context of SMP, a simple pre-coding and post-coding are required at the transmitter and the receiver respectively. The pre-coding filter is taken as $\mathbf{V_{pre}}(z) = \mathbf{V}(z)^{-1}$ and the post-coding filter is $\mathbf{U_{post}}(z) = \mathbf{U}(z)^{-1}$. Note that both pre-coding and post-coding filters are stable and causal. Moreover, as opposed to RF MIMO channels, the VLC channel is stationary, and therefore the pre-coding and post-coding matrices do not vary for a given user location.

Let us now denote $\mathbf{x}(z) = [x_1(z), \ldots, x_{N_t}(z)]^T$ the vector containing the spatially multiplexed signals on each transmit LD. After pre-coding, the signal becomes $\hat{\mathbf{x}}(z) = [\hat{x}_1(z), \ldots, \hat{x}_{N_t}(z)]$. After transmission through the MIMO VLC channel, the received signal vector $\mathbf{y}(z) = [y_1(z), \ldots, y_{N_r}(z)]^T$ is post-coded, yielding the signal vector $\hat{\mathbf{y}}(z) = [\hat{y}_1(z), \ldots, \hat{y}_{N_r}(z)]^T$ expressed as

$$\begin{aligned}\hat{\mathbf{y}}(z) &= \mathbf{U_{post}}(z)\mathbf{H}(z)\hat{\mathbf{x}}(z) + \mathbf{U_{post}}(z)\mathbf{n}(z) \\ &= \mathbf{U_{post}}(z)\mathbf{H}(z)\mathbf{V_{pre}}(z)\mathbf{x}(z) + \mathbf{U_{post}}(z)\mathbf{n}(z) \\ &= \mathbf{U}(z)^{-1}\mathbf{U}(z)\mathbf{D}(z)\mathbf{V}(z)\mathbf{V}(z)^{-1}\mathbf{x}(z) + \mathbf{U_{post}}(z)\mathbf{n}(z) \\ &= \mathbf{D}(z)\mathbf{x}(z) + \mathbf{U_{post}}(z)\mathbf{n}(z),\end{aligned} \tag{7.21}$$

where $\mathbf{n}(z)$ is the noise. The overall transmission process is described in Fig. 7.4. It should be noted that all diagonal entries of the resulting matrix $\mathbf{D}(z)$ are equivalent to additive noise channels (except for the last one), thus no additional complex equalization is required at the receiver. An interesting feature of the decomposition is that the ICI is completely canceled and the MIMO channel is reduced to $N_s = \min(N_t, N_r) - 1$ independent simple additive noise channels with no ISI. The degradation in LU-PMD stems from the noise enhancement after applying the post-coding filter $\mathbf{U_{post}}(z)$ which is not paraunitary. Moreover, $\mathbf{V_{pre}}(z)$, also not paraunitary, might enhance the signal power after the precoding operation. In VLC systems employing IM/DD, the LD driving signal must be unipolar and positive. Therefore, a DC bias current I_{DC} is applied to the signal to be transmitted. Moreover the LD dynamic range is fixed, constraining the output optical signal amplitude to be upper bounded by a maximum optical power P_{max} such that $0 \leq P_t(1 + M_j\hat{x}_j(z)) \leq P_{max}$, where $\hat{x}_j(z)$ is the precoded signal at the j^{th} transmit LD, P_t is the mean emitted optical power and M_j is the modulation index of the precoded signal

$\hat{x}_j(z)$. Therefore, the pre-coding operation will yield different modulation indices for each LD.

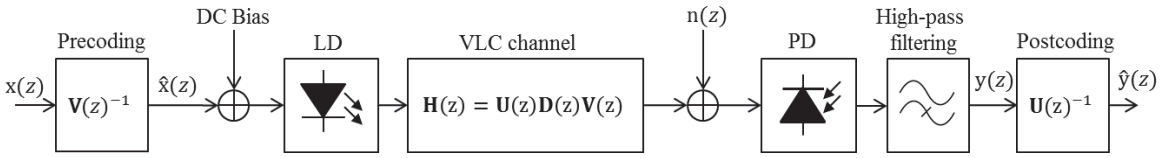

Figure 7.4 Diagram of VLC system employing SMP with LU-PMD.

7.5.2 Numerical results

In this section, the performance of SMP with LU-PMD is evaluated in simulation. A 2-PAM signal is selected for transmission at baud rate 300 Mbaud, yielding a total modulation bandwidth of 172.5 MHz (assuming square-root raised cosine filtering with roll-off factor 0.15), which is a realistic paramater value based on the characteristics of commercially-available components. Furthermore, the pre-coding filter and post-coding filter matrices are respectively determined to be

$$\mathbf{V_{pre}}(z) = \begin{bmatrix} 1 & -0.3114z^{-8} & -0.3067z^{-11} & -2.2878z^{-17} + 2.3268z^{-16} \\ 0 & 1 & 0.3741z^{-3} & 2.6219z^{-9} - 2.8374z^{-8} \\ 0 & 0 & 1 & 7.1809z^{-6} - 7.5855z^{-5} \\ 0 & 0 & 0 & 1 \end{bmatrix} \tag{7.22}$$

and

$$\mathbf{U_{post}}(z) = \begin{bmatrix} 0 & 1.0284 & 0 & 0 \\ 0 & 33.4181 & -32.4957 & 0 \\ 0 & -70.2639 & 0 & 70.2639 \\ 4.26 \times 10^{-4} & -4.34 \times 10^{-4} & -4.26 \times 10^{-4} & 4.34 \times 10^{-4} \end{bmatrix}, \tag{7.23}$$

and the modulation index after the precoding operation for LD1, LD2, LD3, and LD4 are determined to be 0.55, 0.55, 1 and 0.22, respectively.

The received eye diagrams at a SNR equal to 50 dB are shown in Fig. 7.5 for all four PDs. It can be observed that the eye diagram at PD1 is clear and the signal is almost

unaffected by the noise enhancement. The received signal on PD2 is also error-free. On the other hand, the received signals at PD3 suffers from the noise enhancement due to post-coding, and the calculated BER is 3.39×10^{-4}. Therefore, an aggregate data rate of 900 Mbps can be achieved by multiplexing 300 Mbaud 2-PAM signals over the three independent channels with a BER inferior to 10^{-3}.

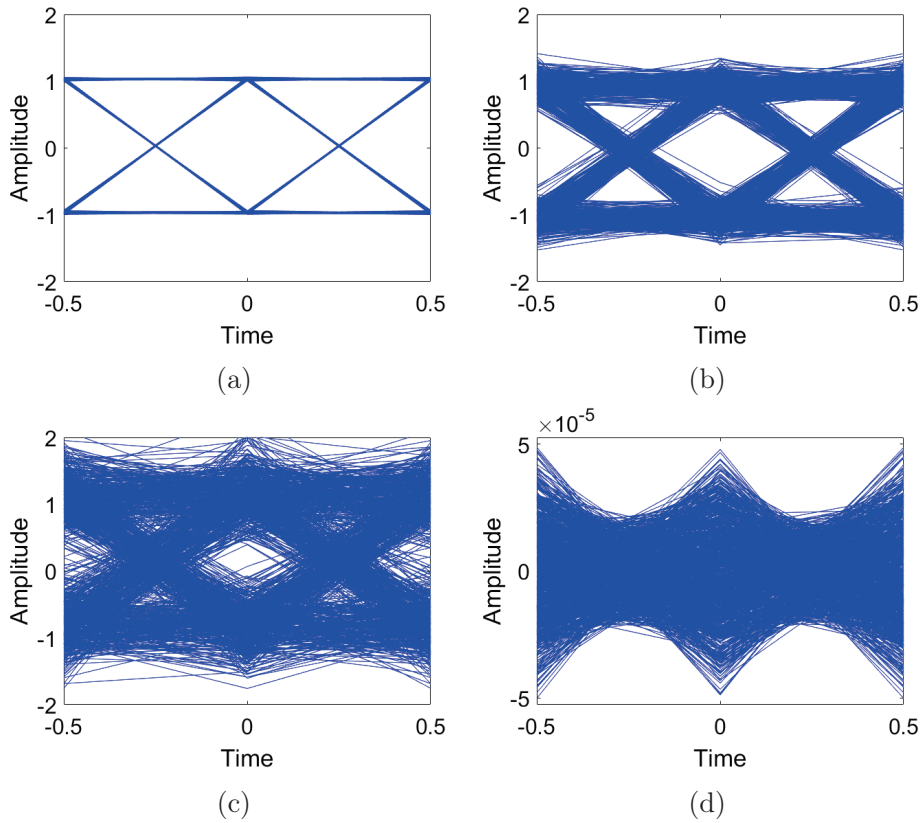

Figure 7.5 Received eye diagrams for (a) PD1, (b) PD2, (c) PD3 and (d) PD4, at SNR = 50 dB.

7.6 Conclusion

In this chapter, the LU-PMD algorithm was applied to a MIMO VLC channel in a large space environment. This technique suppresses the ICI by performing a complete diagonalization of the channel matrix and leads to independent SISO channels with no ISI, except for the last subchannel. When employing SMP with LU-PMD, the VLC system requires a simple pre-filtering and post-filtering operation at the transmitter and the receiver respectively, which are easy to implement since the pre-coding and post-coding matrices are causal and stable. The performance was evaluated in a 4×4 MIMO configuration with a 300 Mbaud 2-PAM signal and it was shown that an aggregate data rate of 900 Mbps

can be achieved at SNR = 50 dB, while maintaining a BER level below 10^{-3}. Due to lack of time, we could not provide more research effort with regard to the evaluation of the performance of SMP with LU-PMD. However, remaining research directions are given in the next chapter, which is the concluding chapter of this thesis.

CHAPTER 8

Conclusion and perspectives

8.1 Introduction

While 5G networks are currently being deployed, many research efforts are being channeled towards beyond 5G and 6G to fulfill the huge demands for growing data traffic. In this context, VLC is gaining momentum for a potential integration into the next generations of wireless technologies. Indeed, owing to its benefits, namely the energy-efficiency, the large unlicensed bandwidth, the electromagnetic interference immunity, and the low-cost installation, VLC can complement RF systems in indoor environments. However, VLC is still facing many challenges, preventing the data rate to be competitive. Among them, the limiting characteristics of the low-cost white LEDs, such as the nonlinearity, which causes severe distortions to the information signal, and the limited modulation bandwidth. In this thesis, we investigated signal processing techniques to optimize the system throughput in a VLC system. In addition, a major asset of VLC is the possibility to leverage the existing lighting infrastructure and to serve the dual purpose of illumination and communication simultaneously. Therefore, the lighting quality is an essential feature which has been taken into account in this research work.

In **Chapter 2**, the fundamental concepts of VLC were presented, including the characteristics of the optical wireless channel, the types of front-end optical components, the LED nonlinearity, the key metrics for indoor illumination, and finally state-of-the art digital modulation techniques. Moreover, recent VLC experimental transmission were reported. Based on the synthesis of these elements, we justified our assumptions and our decision to employ spectral-efficient modulation schemes such as PAM, CAP modulation, MIMO techniques, with widely used low-cost white LEDs and PIN PDs for the experimental testbeds.

In **Chapter 3**, the CAP modulation scheme was described theoretically in detail. In addition, the illumination requirement for normal working conditions in a typical office room was detailed and taken into account in the system design. Following a presentation of the different transmission steps with CAP modulation over the test bench, an optimization of the bitrate was performed. As a result, a bitrate of 184 Mbps with a BER lower than 10^{-3} was demonstrated with a 16-CAP signal, without compensation of the nonlinearity

and with a simple linear fractionally-spaced equalizer (FSE) to resolve any timing jitter issue. Distortions were noticed on the received constellation diagrams, which typically reflect the impact of LED nonlinearity. This observation led us to seek improvements at the receiver for nonlinearity mitigation.

Chapter 4 was dedicated to the development of a simulation model to evaluate the performance of transmission over the testbed described in Chapter 3. We proposed an analytical model for the LED frequency response, which is very close to the measured one. The received SNR was determined both in the simulation model and by experiment, and it was determined that the simulation exhibits a gain of $\sim$ 1-2 dB, which leads to a slight overestimation of the results compared to the experiment. Furthermore, a DFE block was added to the linear FSE, for a more effective ISI mitigation. As a second step, two models with memory were investigated to model the impact of the LED nonlinearity, namely the Hammerstein and the Volterra series model, and it was shown that the latter leads to a fair approximation of the nonlinear behavior of the LED. Therefore, the Volterra series model was also implemented as an adaptive postdistorter at the receiver to mitigate the nonlinearity. The postdistortion algorithm was tested in simulation and the results have shown its effectiveness in mitigating the LED nonlinearity, which justified its adoption in the further work.

In **Chapter 5**, two modulation schemes were compared under illumination constraints, namely PAM and CAP modulation, through both simulations and experimental measurements. We used the simulation model developed in Chapter 4 and the test bench described in Chapter 3 to evaluate the performance of both PAM and CAP. The impact of the roll-off factor parameter, which is directly related to the total occupied bandwidth, and the maximum achievable throughput for PAM and CAP for various spectral efficiencies were investigated. Moreover, adaptive postdistortion based on a Volterra series expansion was implemented to mitigate the effects of LED nonlinearity in practice. We also demonstrated that for high modulation orders, PAM can slightly outperform CAP when the LED nonlinearity is adequately compensated. In a linearized system, the data rates are nonetheless similar and are on the order of 210 Mbps. On the other hand, when the nonlinearity is left unmitigated, CAP show more robustness and can achieve higher bitrate than PAM. It was shown that both schemes in conjunction with equalization and nonlinearity compensation can significantly outperform DMT, which data rate is limited to 100 Mbps and 145 Mbps without and with nonlinearity postdistortion compensation, respectively.

In **Chapter 6**, two MIMO techniques, namely SMP and SM in conjunction with PAM modulation were presented. In the first instance, the BER performance of both tech-

niques were evaluated numerically and theoretically with and without imaging receiver. The results demonstrated a significant gain of ∼36 dB and ∼16 dB for SMP and SM, respectively, compared to the non-imaging case. As a second step, a 2×2 MIMO setup with imager was presented. This MIMO test bench reflects realistic indoor distances (2.25 m) and is compatible with the use of LED spotlights made of multiple mid-power LEDs to provide a sufficient level illumination in a room. Then, channel gains measurements were performed for various positions of the receiver to evaluate the impact of misalignment. For each location of the receiver, the PDs had to be manually and independently readjusted in order to capture the maximum light intensity. Furthermore, using the channel gains measured in practice, the BER performance of SMP and SM were evaluated for two spectral efficiencies, namely 4 bit/s/Hz and 6 bit/s/Hz. It was concluded that SMP offers superior performance. Lastly, it was shown that a form of adaptive bit-loading can be employed when the imager is misaligned with respect to the transmit LEDs to maintain the communication link quality.

Finally, we proposed in **Chapter 7** a lower-upper polynomial matrix decomposition named "LU-PMD" for MIMO VLC employing laser diodes in large indoor space scenarios such as airport halls, convention centers or factories for instance. The LU-PMD completely cancels the ICI and reduces the MIMO channel into independent SISO additive noise channels. As a result, the ISI stemming from the successive arrivals of signals emitted by different transmitters is mitigated. As a first step, the principle of the decomposition was described and an example of application for a 4×4 MIMO system was presented. Then, the SMP technique was employed in conjunction with pre- and post-coding by respectively using the pre-filter and post-filter matrices obtained after LU-PMD. A 300 Mbaud transmission with a 2-PAM signal was performed in simulation and it was shown that three resulting noise-additive sub-channels can be effectively used for transmission at relatively high SNR, yielding a bitrate rate of 900 Mbps, while the last sub-channel is unusable. The major drawback of the LU-PMD technique is that aforementioned pre- and post-filter matrices are not paraunitary. As result, the information signal after pre-coding is amplified and the current dynamic range of every LD is not fully leveraged. In addition, the noise after post-coding is amplified, thus degrading the system performance.

8.2 Author's contributions

The contributions of this thesis are concisely mentioned as follows:

- Proposed a method to optimize the bitrate with CAP modulation while maintaining a constant level of illumination at the receiver that is compliant with illumination

standards.

- Compared PAM and CAP modulation under illumination constraints in simulation and by experiment with a setup made of low-cost components. Demonstrated that for high modulation orders, the performance of PAM are strongly degraded in presence of nonlinearity compared to CAP. On the other hand, when the nonlinearity is mitigated by adaptive postdistortion, PAM can slightly outperform CAP. Showed that both PAM and CAP can outperform DMT in terms of achievable bit rate.

- Investigated the performance of two MIMO techniques, namely SMP and SM in simulation by leveraging the channels gains measured on a test bench employing an imaging receiver. Demonstrated superior performance for SMP. Assessed the impact of imager misalignment and proposed a form of adaptive bit-loading in conjunction with SMP to significantly improve the BER performance.

- Proposed for the first time the LU-PMD technique for MIMO VLC systems in large indoor environments to mitigate the ICI and the ISI stemming from the difference in the length of the optical paths.

8.3 List of publications

Journal paper

- R. L. Priol, M. Hélard, S. Haese and S. Roy, "Experimental Comparison of PAM and CAP Modulation for Visible Light Communication Under Illumination Constraints," in IEEE Photonics Journal, vol. 14, no. 2, pp. 1-11, April 2022, Art no. 7315811.

Conference papers

- R. Le Priol, S. Haese, M. Helard, A. Jabban and S. Roy, "Experimental VLC Transmission Employing CAP Modulation with Low-Cost Components under Illumination Constraints," 2019 IEEE 90th Vehicular Technology Conference (VTC2019-Fall), 2019, pp. 1-5.
- R. Le Priol, M. Helard, S. Haese, and S. Roy, "MIMO Techniques in a Visible Light Communication (VLC) Link with Imager," 2022 20th IEEE International New Circuits and Systems Conference (NEWCAS), 2022.

Technical article

- R. Le Priol, S. Haese, M. Hélard, A. Jabban, and S. Roy. "Optimizing data rates for visible light communication with carrierless amplitude and phase modulation," 2022. MathWorks Technical Articles and Newsletters.https://mathworks.com/company/newsletters/articles/optimizing-data-rates-for-visible-light-communication-with-carrierless-amplitude-and-phase-modulation.html

8.4 Perspectives

Several research avenues have been identified to further develop the work of this thesis.

1. The comparison study carried out in Chapter 5 shows the advantages of CAP and PAM over DMT in practical VLC systems. In addition, it was observed that for high modulation orders, CAP is more robust than PAM in presence of nonlinearity in the system. However, in practice the compensation of nonlinearity is not perfect due to temperature variations and aging of the components. To this extent, CAP could be more attractive than PAM. Therefore, an interesting research work could be the further exploration of this aspect of the comparison.

2. In Chapter 5, the LED nonlinearity was compensated at the receiver with postdistortion. The LED nonlinearity can also be compensated at the transmitter using predistortion, provided that a feedback exists from the receiver to the transmitter with information on the coefficients of the Volterra series. Therefore, an interesting approach would be to compare the performance of postdistortion versus predistortion.

3. In Chapter 6, we demonstrated the benefit of using an imager to separate the different beams at the receiver and avoid ICI. However, when the receiver is moved, the image spots are shifted with respect to the PDs due to the diffraction of light in the imaging lens. Therefore, we could consider the use of a receiver which is able to mechanically adjust the PDs angles and locations to detect the maximum light intensity. Recent advances in microelectromechanical systems (MEMS) have led researchers to explore their potential applications in VLC receivers, more specifically in a context of mobility. For instance, the authors of [105] employed a MEMS-based receiver for vehicular VLC which can control the rotation of the PD to find an optimum angle while the vehicle is moving. Therefore, an interesting study would be to integrate a MEMS-controlled array of PDs with an imaging lens to fully support user mobility in a MIMO configuration.

4. The performance of SMP with LU-PMD was evaluated in Chapter 7 for a single user location. An interesting study would be to investigate different user locations and / or with more transmitters and receivers. Performance evaluation could also be performed considering a richer multipath environment. Furthermore, laser sources at infrared could be evaluated as a possible application, as these communication scenarios are more mature and widely used. A complexity analysis would also be required in order to evaluate the power consumption relative to the implementation of the LU-PMD technique on mobile devices. One advantage of using LU-PMD in VLC is that the MIMO channel is static for a given user location. Therefore, the pre-filter and post-filter matrices can be computed only once. In fact, with knowledge of the environment geometry, such matrices could be pre-computed and their values stored in a table. Concerning the algorithm itself, an interesting point for future research would be to add an additional row in the MIMO channel matrix, so that the last diagonal element of the channel matrix can be reduced to 1. This could be achieved by selecting a number of photodiodes equal to the number of LEDs plus one. In addition, techniques to mitigate the noise amplification stemming from the post-coding operation at the receiver could be developed.

APPENDIX A

Demodulation of QAM and CAP received signals

A.1 QAM demodulation

The in-phase arm $r_a(t)$ after matched filtering in QAM (see Fig. 3.3) can be expressed as

$$r_a(t) = r_{II}(t) + r_{IQ}(t), \tag{A.1}$$

where $r_{II}(t)$ is the desired part and $r_{IQ}(t)$ is the interference part. The desired part can be further expressed as

$$\begin{aligned} r_{II}(t) &= \left(\sum_k a_k g(t - kT) \cos^2(2\pi f_c t) \right) * g(-t) \\ &= \underbrace{\frac{1}{2} \sum_k a_k g(t - kT) * g(-t)}_{1^{st} \text{ term}} \\ &+ \underbrace{\left(\frac{1}{2} \sum_k a_k g(t - kT) \cos(4\pi f_c t) \right) * g(-t)}_{2^{nd} \text{ term}} . \end{aligned} \tag{A.2}$$

The second term in (A.2) vanishes because it is equivalent to filtering a signal $g(t)$ modulated around the frequency $2f_c$ with a low-pass filter of maximum frequency f_c. The interference part $r_{IQ}(t)$ can be expressed as

$$\begin{aligned} r_{IQ}(t) &= \left(\sum_k a_k g(t - kT) \sin(2\pi f_c t) \cos(2\pi f_c t) \right) * g(-t) \\ &= \left(\frac{1}{2} \sum_k b_k g(t - kT) \sin(4\pi f_c t) \right) * g(-t). \end{aligned} \tag{A.3}$$

The interference part vanishes too. Therefore we have

$$r_a(t) = \frac{1}{2}\sum_k a_k g(t - kT) * g(-t). \tag{A.4}$$

Following a similar derivation, the quadrature arm $r_b(t)$ can be expressed as

$$r_b(t) = \frac{1}{2}\sum_k b_k g(t - kT) * g(-t). \tag{A.5}$$

A.2 CAP demodulation

Let us first denote the quantities $h_{II}(t)$ and $h_{IQ}(t)$ such that

$$\begin{aligned} h_{II}(t) &= g(t)\cos(2\pi f_c t) * g(-t)\cos(2\pi f_c t), \\ h_{IQ}(t) &= g(t)\sin(2\pi f_c t) * g(-t)\cos(2\pi f_c t). \end{aligned} \tag{A.6}$$

In CAP, the in-phase arm $r_a(t)$ after matched filtering can be written as follows:

$$\begin{aligned} r_a(t) &= r_{II}(t) + r_{IQ}(t) \\ &= \sum_k a_k \delta(t - kT) * h_{II}(t) - \sum_k b_k \delta(t - kT) * h_{IQ}(t). \end{aligned} \tag{A.7}$$

Note that $g(t) = g(-t)$. Let us further expand the term $h_{II}(t)$:

$$h_{II}(t) = \int_{-\infty}^{\infty} g(\tau)\cos(2\pi f_c \tau) g(t - \tau)\cos(2\pi f_c t - 2\pi f_c \tau) d\tau, \tag{A.8}$$

$$2h_{II}(t) = \int_{-\infty}^{\infty} g(\tau) g(t - \tau)\left(\cos(4\pi f_c \tau - 2\pi f_c \tau) + \cos(2\pi f_c t)\right) d\tau, \tag{A.9}$$

$$\begin{aligned} 2h_{II}(t) = &\underbrace{\int_{-\infty}^{\infty} g(\tau) g(t - \tau)\cos(2\pi f_c t)\, d\tau}_{1^{st}\text{ term}} \\ &+ \underbrace{\int_{-\infty}^{\infty} g(\tau) g(t - \tau)\left(\cos(4\pi f_c \tau - 2\pi f_c \tau)\right) d\tau}_{2^{nd}\text{ term}}. \end{aligned} \tag{A.10}$$

The second term in (A.10) vanishes because it is equivalent to filter a signal $g(t)$ modulated around the frequency $2f_c$ with a low-pass filter of maximum frequency f_c. As a result, we have

$$h_{II}(t) = \frac{1}{2}\cos(2\pi f_c t)\int_{-\infty}^{\infty} g(\tau)g(t-\tau)d\tau. \tag{A.11}$$

The quantity $h_{IQ}(t)$ can be expanded in a similar fashion such that

$$\begin{aligned} h_{IQ}(t) = & \int_{-\infty}^{\infty} g(\tau)\sin(2\pi f_c\tau)g(t-\tau)\cos(2\pi f_c t - 2\pi f_c\tau)d\tau \\ & = \int_{-\infty}^{\infty} g(\tau)\sin(2\pi f_c\tau)g(t-\tau)\cos(2\pi f_c\tau)\cos(2\pi f_c t)d\tau \\ & + \int_{-\infty}^{\infty} g(\tau)\sin(2\pi f_c\tau)g(t-\tau)\sin(2\pi f_c\tau)\sin(2\pi f_c t)d\tau. \end{aligned} \tag{A.12}$$

Using trigonometric formulas, we have

$$\begin{aligned} h_{IQ}(t) = & \underbrace{\frac{1}{2}\cos(2\pi f_c t)\int_{-\infty}^{\infty} g(\tau)g(t-\tau)\sin(4\pi f_c\tau)d\tau}_{1^{st}\text{ term}} \\ & \underbrace{-\frac{1}{2}\sin(2\pi f_c t)\int_{-\infty}^{\infty} g(\tau)g(t-\tau)\cos(4\pi f_c\tau)d\tau}_{2^{nd}\text{ term}} \\ & \underbrace{+\frac{1}{2}\sin(2\pi f_c t)\int_{-\infty}^{\infty} g(\tau)g(t-\tau)d\tau}_{3^{rd}\text{ term}}. \end{aligned} \tag{A.13}$$

Note that in (A.13), the first two terms vanish because one again, they correspond to low-pass filtering of signals centered around $2f_c$. Therefore, only the third term remains such that

$$h_{IQ}(t) = \frac{1}{2}\sin(2\pi f_c t)\left(g(t) * g(t)\right). \tag{A.14}$$

Finally, as initially defined, $r_a(t)$ is the sum of a desired part in (A.11) and an interference part in (A.14) such that

$$r_a(t) = \underbrace{\frac{1}{2}\sum_k a_k \delta(t-kT) * \left(\cos(2\pi f_c t)\left(g(t) * g(t)\right)\right)}_{\text{Desired part}} \underbrace{-\frac{1}{2}\sum_k b_k \delta(t-kT) * \left(\sin(2\pi f_c t)\left(g(t) * g(t)\right)\right).}_{\text{Interference part}} \tag{A.15}$$

The derivation can also naturally be applied to the quadrature arm $r_b(t)$, which yields

$$r_b(t) = \underbrace{\frac{1}{2}\sum_k b_k \delta(t-kT) * \left(\cos(2\pi f_c t)\left(g(t) * g(t)\right)\right)}_{\text{Desired part}} \underbrace{-\frac{1}{2}\sum_k a_k \delta(t-kT) * \left(\sin(2\pi f_c t)\left(g(t) * g(t)\right)\right).}_{\text{Interference part}} \tag{A.16}$$

APPENDIX B
DMT signaling scheme

The structure of a DMT transmitter is detailed in Fig. B.1 (a). First, serial-to-parallel (S/P) is performed and the incoming bits are modulated by a QAM modulator, generating a block of $N-1$ usable symbols $X = \{X_1, X_2, X_3, ..., X_{N-1}\}$. The symbols are then mapped to N subcarriers, the first and central subcarriers being zeroed. Next, Hermitian symmetry is applied prior to a $2N$-point IFFT operation in order to output a discrete real-valued samples expressed as [95]

$$\begin{gathered} S(k) = \frac{1}{\sqrt{2N}} \sum_{n=0}^{2N-1} 2\mathrm{Re}\left\{ X_n \exp(j2\pi n \frac{k}{2N}) \right\}, \\ k = 0, 1, ..., 2N-1; \\ X_0 = X_N = 0 \text{ and } X_{2N-n} = X_n^*, \end{gathered} \tag{B.1}$$

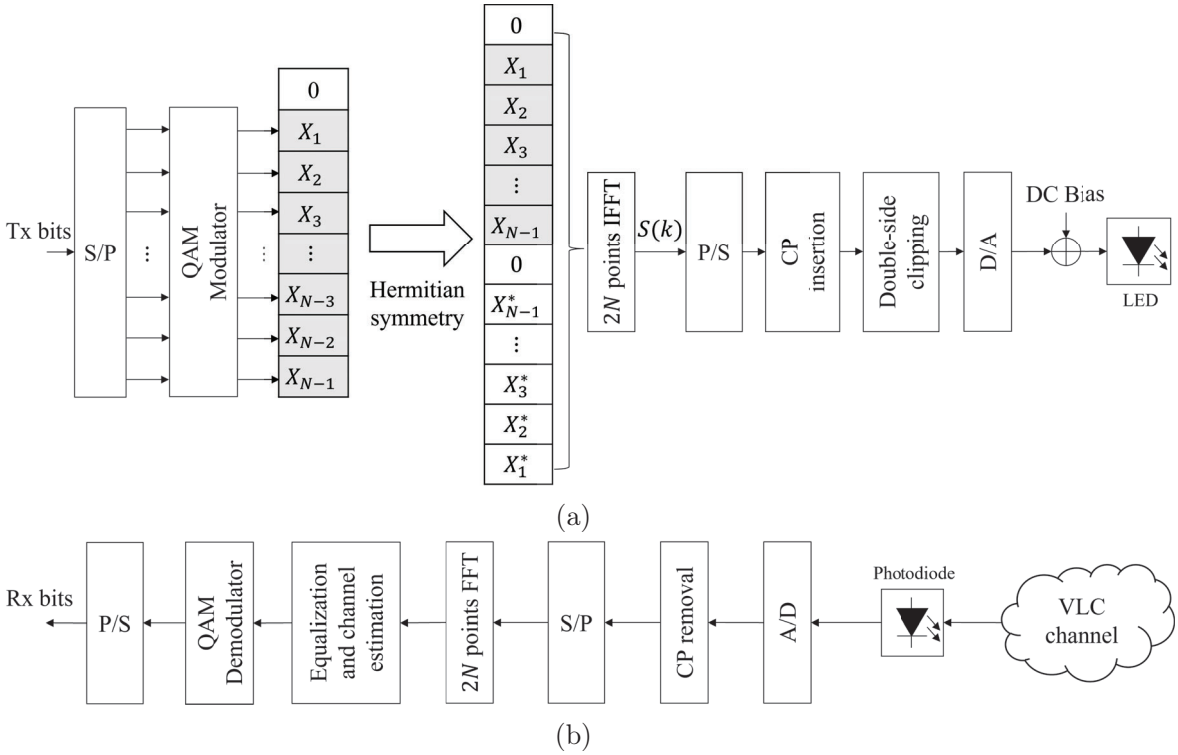

Figure B.1 Block diagram of DMT (a) transmitter and (b) receiver.

where X_n^* denotes the complex conjugate of X_n. Then, parallel-to-serial (P/S) conversion is performed prior to cycling prefix (CP) insertion of size N_{CP} and bilateral amplitude clipping is applied. Following digital-to-analog (D/A) conversion, a DC bias is added, the

latter having a two-fold function: 1) to ensure the LED driving signal is unipolar and positive, and 2) to set the desired amount of illumination.

At the receiver side (Fig. B.1 (b)), A/D conversion is performed to digitize the receive signal and S/P is applied prior to a AN points FFT. Then, one-tap equalization and/or channel estimation are performed. Lastly, the symbols are de-mapped with a QAM demodulator and P/S is applied to recover the information bits.

LIST OF REFERENCES

[1] Zubair Ahmed, Long Zhang, Grahame Faulkner, Dominic O'Brien, and Steve Collins. A shot-noise limited 420 Mbps visible light communication system using commerical off-the-shelf silicon photomultiplier (SiPM). In *2019 IEEE International Conference on Communications Workshops (ICC Workshops)*, pages 1–5. IEEE, 2019.

[2] Kabiru O. Akande, Paul Anthony Haigh, and Wasiu O. Popoola. Joint equalization and synchronization for carrierless amplitude and phase modulation in visible light communication. In *2017 13th International Wireless Communications and Mobile Computing Conference (IWCMC)*, pages 876–881, 2017.

[3] Kabiru O. Akande, Paul Anthony Haigh, and Wasiu O. Popoola. On the implementation of carrierless amplitude and phase modulation in visible light communication. *IEEE Access*, 6:60532–60546, 2018.

[4] Kabiru O. Akande and Wasiu O. Popoola. Impact of timing jitter on the performance of carrier amplitude and phase modulation. In *2016 International Conference for Students on Applied Engineering (ISCAE)*, pages 259–263. IEEE, 2016.

[5] Kabiru O. Akande and Wasiu O. Popoola. Spatial carrierless amplitude and phase modulation technique for visible light communication systems. *IEEE Systems Journal*, 13(3):2344–2353, 2019.

[6] S. P. Alaka, T. L. Narasimhan, and A. Chockalingam. Generalized spatial modulation in indoor wireless visible light communication. In *2015 IEEE Global Communications Conference (GLOBECOM)*, pages 1–7, 2015.

[7] Noha Anous, Tarek Ramadan, Mohamed Abdallah, Khalid Qaraqe, and Diaa Khalil. Impact of blue filtering on effective modulation bandwidth and wide-angle operation in white LED-based VLC systems. *OSA Continuum*, 1(3):910–929, Nov 2018.

[8] J. Armstrong and A.J. Lowery. Power efficient optical OFDM. *Electronics Letters*, 42(6):370, 2006.

[9] Jean Armstrong. OFDM for optical communications. *Journal of Lightwave Technology*, 27(3):189–204, 2009.

[10] Jean Armstrong and Brendon Schmidt. Comparison of asymmetrically clipped optical OFDM and DC-biased optical OFDM in AWGN. *IEEE Communications Letters*, 12(5):343–345, 2008.

[11] Shlomi Arnon. *Visible Light Communication*. Cambridge University Press, 2015.

[12] Ertugrul Basar, Miaowen Wen, Raed Mesleh, Marco Di Renzo, Yue Xiao, and Harald Haas. Index modulation techniques for next-generation wireless networks. *IEEE Access*, 5:16693–16746, 2017.

[13] R. Bian, I. Tavakkolnia, and H. Haas. 10.2 Gb/s visible light communication with off-the-shelf LEDs. In *2018 European Conference on Optical Communication (ECOC)*, pages 1–3, 2018.

[14] Rui Bian, Iman Tavakkolnia, and Harald Haas. 15.73 Gb/s visible light communication with off-the-shelf LEDs. *Journal of Lightwave Technology*, 37(10):2418–2424, 2019.

[15] Rui Bian, Stefan Videv, Alexander D. Griffiths, Jonathan J. D. McKendry, Enyuan Xie, Erdan Gu, Martin D. Dawson, and Harald Haas. Experimental demonstration of generalised space shift keying for visible light communication. In *2017 IEEE International Black Sea Conference on Communications and Networking (BlackSeaCom)*, pages 1–5. IEEE, 2017.

[16] Salah Bourennane, Mike Wolf, Zabih Ghassemlooy, Shihe Long, and Mohammad Ali Khalighi. Investigating channel frequency selectivity in indoor visible-light communication systems. *IET Optoelectronics*, 10(3):80–88, 2016.

[17] British Standards Institution. Light and lighting - lighting of work places. part 1: Indoor work places. EN 12464-1 Std., 2011.

[18] Andrew Burton, Hoa Le Minh, Zabih Ghassemlooy, Edward Bentley, and Carmen Botella. Experimental demonstration of 50-Mb/s visible light communications using 4×4 MIMO. *IEEE Photonics Technology Letters*, 26(9):945–948, 2014-05.

[19] Pankil M. Butala, Hany Elgala, and Thomas D. C. Little. Performance of optical spatial modulation and spatial multiplexing with imaging receiver. In *2014 IEEE Wireless Communications and Networking Conference (WCNC)*, pages 394–399. IEEE, 2014.

[20] Zahra Nazari Chaleshtori, Andrew Burton, Zabih Ghassemlooy, and Stanislav Zvanovec. A flexible OLED based VLC link with m-CAP modulation. In *2019 15th International Conference on Telecommunications (ConTEL)*, pages 1–6. IEEE, 2019.

[21] Zahra Nazari Chaleshtori, Petr Chvojka, Stanislav Zvanovec, Zabih Ghassemlooy, and Paul Anthony Haigh. A survey on recent advances in organic visible light communications. In *2018 11th International Symposium on Communication Systems, Networks & Digital Signal Processing (CSNDSP)*, pages 1–6. IEEE, 2018.

[22] Yu-Chieh Chi, Dan-Hua Hsieh, Chung-Yu Lin, Hsiang-Yu Chen, Chia-Yen Huang, Jr-Hau He, Boon Ooi, Steven P. DenBaars, Shuji Nakamura, Hao-Chung Kuo, and Gong-Ru Lin. Phosphorous diffuser diverged blue laser diode for indoor lighting and communication. *Scientific Reports*, 5(1):18690, December 2015.

[23] Danial Chitnis, Long Zhang, Hyunchae Chun, Sujan Rajbhandari, Grahame Faulkner, Dominic O'Brien, and Steve Collins. A 200 Mb/s VLC demonstration with a SPAD based receiver. In *2015 IEEE Summer Topicals Meeting Series (SUM)*, pages 226–227. IEEE, 2015.

[24] Chi-Wai Chow, Yun-Han Chang, Liang-Yu Wei, Chien-Hung Yeh, and Yang Liu. 26.228-Gbit/s RGBV Visible Light Communication (VLC) with 2-m Free Space Transmission. In *2020 Opto-Electronics and Communications Conference (OECC)*, pages 1–3, Taipei, Taiwan, October 2020. IEEE.

[25] Hyunchae Chun, Chien-Jung Chiang, Andrew Monkman, and Dominic O'Brien. A study of illumination and communication using organic light emitting diodes. *Journal of Lightwave Technology*, 31(22):3511–3517, 2013.

[26] Hyunchae Chun, Sujan Rajbhandari, Grahame Faulkner, Dobroslav Tsonev, Enyuan Xie, Jonathan James Donald McKendry, Erdan Gu, Martin D. Dawson, Dominic C. O'Brien, and Harald Haas. LED based wavelength division multiplexed 10 gb/s visible light communications. *Journal of Lightwave Technology*, 34(13):3047–3052, 2016.

[27] *Cisco Annual Internet Report (2018–2023)*. Cisco White Paper, 2020.

[28] Giulio Cossu, Raffaele Corsini, Amir M. Khalid, and Ernesto Ciaramella. Bi-directional 400 Mbit/s LED-based optical wireless communication for non-directed line-of-sight transmission. In *Optical Fiber Communication Conference*, page Th1F.2. OSA, 2014.

[29] Giulio Cossu, Ali Wajahat, Raffaele Corsini, and Ernesto Ciaramella. 5.6 Gbit/s downlink and 1.5 Gbit/s uplink optical wireless transmission at indoor distances ($\geq$ 1.5 m). In *2014 The European Conference on Optical Communication (ECOC)*, pages 1–3. IEEE, 2014.

[30] Svilen Dimitrov and Harald Haas. *Principles of LED Light Communications*. Cambridge University Press, Cambridge, United Kingdom, 2015.

[31] Svilen Dimitrov, Sinan Sinanovic, and Harald Haas. Clipping noise in OFDM-based optical wireless communication systems. *IEEE Transactions on Communications*, 60(4):1072–1081, 2012.

[32] Hany Elgala, Raed Mesleh, and Harald Haas. A study of LED nonlinearity effects on optical wireless transmission using OFDM. In *2009 IFIP International Conference on Wireless and Optical Communications Networks*, pages 1–5, 2009.

[33] Mohammed Abd Elkarim, M. M. Elsherbini, Hala M. AbdelKader, and Moustafa H. Aly. Exploring the effect of LED nonlinearity on the performance of layered ACO-OFDM. *Appl. Opt.*, 59(24):7343–7351, 2020.

[34] Maged A. Esmail and Habib A. Fathallah. Indoor visible light communication without line of sight: investigation and performance analysis. *Photonic Network Communications*, 30(2):159–166, 2015.

[35] European Norm. Photobiological safety of lamps and lamp systems en 62471., 2008.

[36] Thilo Fath, Marco Di Renzo, and Harald Haas. On the performance of space shift keying for optical wireless communications. In *2010 IEEE Globecom Workshops*, pages 990–994. IEEE, 2010.

[37] Nirmal Fernando, Yi Hong, and Emanuele Viterbo. Flip-OFDM for optical wireless communications. In *2011 IEEE Information Theory Workshop*, pages 5–9. IEEE, 2011.

[38] R. X. G. Ferreira, E. Xie, J. J. D. McKendry, S. Rajbhandari, H. Chun, G. Faulkner, S. Watson, A. E. Kelly, E. Gu, R. V. Penty, I. H. White, D. C. O'Brien, and M. D. Dawson. High bandwidth GaN-based micro-LEDs for multi-Gb/s visible light communications. *IEEE Photonics Technology Letters*, 28(19):2023–2026, 2016.

[39] Chadi Gabriel, Mohammad-Ali Khalighi, Salah Bourennane, Pierre Leon, and Vincent Rigaud. Investigation of suitable modulation techniques for underwater wireless

optical communication. In *2012 International Workshop on Optical Wireless Communications (IWOW)*, pages 1–3. IEEE, 2012.

[40] Zhipeng Gao, Yuhao Wang, Xiaodong Liu, Fuhui Zhou, and Kai-Kit Wong. FFDNet-based channel estimation for massive MIMO visible light communication systems. *IEEE Wirel. Commun. Lett.*, 9(3):340–343, 2020.

[41] Zabih Ghassemlooy, W. Popoola, and S. Rajbhandari. *Optical wireless communications: system and channel modelling with MATLAB*. CRC Press, Boca Raton, FL, USA, Second edition, 2018.

[42] R. D. Gitlin and S. B. Weinstein. Fractionally-spaced equalization: An improved digital transversal equalizer. *The Bell System Technical Journal*, 60(2):275–296, 1981.

[43] R. D. Gitlin and S. B. Weinstein. Fractionally-spaced equalization: An improved digital transversal equalizer. *Bell System Technical Journal*, 60(2):275–296, 1981.

[44] Liane Grobe and Klaus-Dieter Langer. Block-based PAM with frequency domain equalization in visible light communications. In *2013 IEEE Globecom Workshops (GC Wkshps)*, pages 1070–1075, Atlanta, GA, USA, 2013. IEEE.

[45] Jelena Grubor, Sebastian Randel, Klaus-Dieter Langer, and Joachim W. Walewski. Broadband information broadcasting using LED-based interior lighting. *Journal of Lightwave Technology*, 26(24):3883–3892, 2008.

[46] Amit Kumar Gupta and Ananthanarayanan Chockalingam. Performance of MIMO modulation schemes with imaging receivers in visible light communication. *Journal of Lightwave Technology*, 36(10):1912–1927, 2018.

[47] Harald Haas. Wireless data from every light bulb. TED Talk. Available: https://www.ted.com/talks/harald_haas_wireless_data_from_every_light_bulb, 2011.

[48] Harald Haas, Liang Yin, Yunlu Wang, and Cheng Chen. What is LiFi? *Journal of Lightwave Technology*, 34(6):1533–1544, 2016.

[49] P. A. Haigh, Z. Ghassemlooy, S. Rajbhandari, and I. Papakonstantinou. Visible light communications using organic light emitting diodes. *IEEE Communications Magazine*, 51(8):148–154, 2013.

[50] Paul Anthony Haigh, Zabih Ghassemlooy, and Ioannis Papakonstantinou. 1.4-Mb/s white organic LED transmission system using discrete multitone modulation. *IEEE Photonics Technology Letters*, 25(6):615–618, 2013.

[51] Paul Anthony Haigh, Zabih Ghassemlooy, Ioannis Papakonstantinou, and Hoa Le Minh. 2.7 Mb/s with a 93-kHz white organic light emitting diode and real time ANN equalizer. *IEEE Photonics Technology Letters*, 25(17):1687–1690, 2013.

[52] Hoa Le Minh, Dominic O'Brien, Grahame Faulkner, Lubin Zeng, Kyungwoo Lee, Daekwang Jung, and YunJe Oh. 80 Mbit/s visible light communications using pre-equalized white LED. In *2008 34th European Conference on Optical Communication*, pages 1–2, Brussels, Belgium, 2008. IEEE.

[53] Chin-Wei Hsu, Chi-Wai Chow, I-Cheng Lu, Yen-Liang Liu, Chien-Hung Yeh, and Yang Liu. High speed imaging 3 × 3 MIMO phosphor white-light LED based visible light communication system. *IEEE Photonics Journal*, 8(6):1–6, 2016.

[54] Muhammad Ijaz, Dobroslav Tsonev, Jonathan J D McKendry, Enyuan Xie, Sujan Rajbhandari, Hyunchae Chun, Grahame Faulkner, Erdan Gu, Martin D Dawson, Dominic O'Brien, and Harald Haas. Experimental proof-of-concept of optical spatial modulation OFDM using micro LEDs. In *2015 IEEE International Conference on Communication Workshop (ICCW)*, pages 1338–1343. IEEE, 2015.

[55] G.-H. Im, D.B. Harman, G. Huang, A.V. Mandzik, M.-H. Nguyen, and J.-J. Werner. 51.84 Mb/s 16-CAP ATM LAN standard. *IEEE Journal on Selected Areas in Communications*, 13(4):620–632, 1995.

[56] International Energy Agency. *Lighting sales by type in the Sustainable Development Scenario, 2010-2030*. https://www.iea.org/data-and-statistics/charts/lighting-sales-by-type-in-the-sustainable-development-scenario-2010-2030. last update 2020.

[57] M. S. Islim, S. Videv, M. Safari, E. Xie, J. J. D. McKendry, E. Gu, M. D. Dawson, and H. Haas. The impact of solar irradiance on visible light communications. *Journal of Lightwave Technology*, 36(12):2376–2386, 2018.

[58] ITU Telecommunication Standardization Sector (ITU-T). ITU-T GG.9991 Std.. High-speed indoor visible light communication transceiver – System architecture, physical layer and data link layer specification, 2019.

[59] Ahmad Jabban, Sylvain Haese, and Maryline Helard. Theoretical and experimental optimization of DMT-based visible light communication under lighting constraints. *EURASIP Journal on Wireless Communications and Networking*, 2020(1):99, 2020.

[60] Ruonan Ji, Shaowei Wang, Qingquan Liu, and Wei Lu. High-speed visible light communications: Enabling technologies and state of the art. *Applied Sciences*, 8(4):589, 2018.

[61] Valencia M. Joyner, David M. Holburn, Dominic C. O'Brien, and Grahame E. Faulkner. A CMOS imaging diversity receiver chip with a flip-chip integrated detector array for optical wireless links. In *LEOS 2006 - 19th Annual Meeting of the IEEE Lasers and Electro-Optics Society*, pages 927–928, 2006.

[62] J.M. Kahn, R. You, P. Djahani, A.G. Weisbin, Beh Kian Teik, and A. Tang. Imaging diversity receivers for high-speed infrared wireless communication. *IEEE Communications Magazine*, 36(12):88–94, 1998.

[63] Joseph M Kahn and John R Barry. Wireless Infrared Communications. *WIRELESS INFRARED COMMUNICATIONS*, 85:34, 1997.

[64] Thomas Kamalakis, Joachim W. Walewski, Georgia Ntogari, and Gerasimos Mileounis. Empirical Volterra-series modeling of commercial light-emitting diodes. *Journal of Lightwave Technology*, 29(14):2146–2155, 2011.

[65] Dilukshan Karunatilaka, Fahad Zafar, Vineetha Kalavally, and Rajendran Parthiban. LED based indoor visible light communications: State of the art. *IEEE Communications Surveys & Tutorials*, 17(3):1649–1678, 2015.

[66] A. M. Khalid, G. Cossu, R. Corsini, P. Choudhury, and E. Ciaramella. 1-Gb/s transmission over a phosphorescent white LED by using rate-adaptive discrete multitone modulation. *IEEE Photonics Journal*, 4(5):1465–1473, 2012.

[67] Mohammad-Ali Khalighi, Shihe Long, Salah Bourennane, and Zabih Ghassemlooy. PAM- and CAP-based transmission schemes for visible-light communications. *IEEE Access*, 5:27002–27013, 2017.

[68] Joonsuk Kim and C. Aldana. Efficient feedback of the channel information for Closedloop beamforming in WLAN. In *2006 IEEE 63rd Vehicular Technology Conference*, volume 5, pages 2226–2230, 2006.

[69] T. Komine and M. Nakagawa. Fundamental analysis for visible-light communication system using LED lights. *IEEE Transactions on Consumer Electronics*, 50(1):100–107, 2004.

[70] Christoph Kottke, Jonas Hilt, Kai Habel, Jelena Vučić, and Klaus-Dieter Langer. 1.25 Gbit/s visible light WDM link based on DMT modulation of a single RGB LED luminary. In *2012 38th European Conference and Exhibition on Optical Communications*, pages 1–3, 2012.

[71] Jenn-Kaie Lain and Yan-He Chen. An ANN-based adaptive predistorter for LED nonlinearity in indoor visible light communications. *Electronics*, 10(8), 2021.

[72] H. Le Minh, D. O'Brien, G. Faulkner, L. Zeng, K. Lee, D. Jung, Y. Oh, and E. T. Won. 100-Mb/s NRZ visible light communications using a postequalized white LED. *IEEE Photonics Technology Letters*, 21(15):1063–1065, 2009.

[73] Robin Le Priol, Sylvain Haese, Maryline Helard, Ahmad Jabban, and Sebastien Roy. Experimental VLC transmission employing CAP modulation with low-cost components under illumination constraints. In *2019 IEEE 90th Vehicular Technology Conference (VTC2019-Fall)*, pages 1–5, 2019.

[74] Robin Le Priol, Sylvain Haese, Maryline Hélard, Ahmad Jabban, and Sébastien Roy. Optimizing data rates for visible light communication with carrierless amplitude and phase modulation, 2022. MathWorks Technical Articles and Newsletters. `https://fr.mathworks.com/company/newsletters/articles/optimizing-data-rates-for-visible-light-communication-with-carrierless-amplitude-and-phase-modulation.html`.

[75] Changmin Lee, Mohamed Sufyan Islim, Sovan Das, Adrian Sparks, Stefan Videv, Paul Rudy, Binith Shah, Melvin Mclaurin, Harald Haas, and James Raring. 26 Gbit/s LiFi system with laser-based white light transmitter. *Journal of Lightwave Technology*, pages 1–1, 2021.

[76] Kwonhyung Lee and Hyuncheol Park. Modulations for visible light communications with dimming control. *IEEE Photonics Technology Letters*, 23(16):1136–1138, 2011.

[77] Honglei Li, Xiongbin Chen, Beiju Huang, Danying Tang, and Hongda Chen. High bandwidth visible light communications based on a post-equalization circuit. *IEEE Photonics Technology Letters*, 26(2):119–122, 2014.

[78] X. Li, N. Bamiedakis, X. Guo, J. J. D. McKendry, E. Xie, R. Ferreira, E. Gu, M. D. Dawson, R. V. Penty, and I. H. White. Wireless visible light communications em-

ploying feed-forward pre-equalization and PAM-4 modulation. *Journal of Lightwave Technology*, 34(8):2049–2055, 2016.

[79] Xiangyu Li, Qian Gao, Chen Gong, and Zhengyuan Xu. Nonlinearity mitigation for VLC with an artificial neural network based equalizer. In *2018 IEEE Globecom Workshops (GC Wkshps)*, pages 1–6, 2018.

[80] S. Long. *Indoor channel modeling and high data rate transmission for visible light communication systems*. PhD thesis, École Centrale de Marseille, Marseille, France, September 2016.

[81] I. Lu, C. Lai, C. Yeh, and J. Chen. 6.36 Gbit/s RGB LED-based WDM MIMO visible light communication system employing OFDM modulation. In *2017 Optical Fiber Communications Conference and Exhibition (OFC)*, pages 1–3, 2017.

[82] Tianyu Luan and Keyuan Qian. Research on influencing factors of LED frequency response. *AIP Conference Proceedings*, 1864(1):020008, 2017.

[83] M. Liu, Matthieu Crussiere, and Jean-Francois Helard. Improved channel estimation methods based on PN sequence for TDS-OFDM. In *2012 19th International Conference on Telecommunications (ICT)*, pages 1–5. IEEE, 2012.

[84] Moustapha Mbaye, Moussa Diallo, and Mamadou Mboup. Unimodular-upper polynomial matrix decomposition for MIMO spatial multiplexing. In *2014 IEEE 15th International Workshop on Signal Processing Advances in Wireless Communications (SPAWC)*, pages 26–29, 2014.

[85] Moustapha Mbaye, Moussa Diallo, and Mamadou Mboup. Lu-based beamforming schemes for MIMO systems. *IEEE Transactions on Vehicular Technology*, 66(3):2214–2222, 2017.

[86] Moustapha Mbaye, Moussa Diallo, and Mamadou Mboup. A robust LU polynomial matrix decomposition for spatial multiplexing. *EURASIP Journal on Advances in Signal Processing*, 2020:45, 2020.

[87] R. Mesleh, R. Mehmood, H. Elgala, and H. Haas. Indoor MIMO optical wireless communication using spatial modulation. In *2010 IEEE International Conference on Communications*, pages 1–5. IEEE, 2010.

[88] Raed Mesleh, Hany Elgala, and Harald Haas. Optical spatial modulation. *Journal of Optical Communications and Networking*, 3(3):234, 2011.

[89] R.Y. Mesleh, H. Haas, S. Sinanovic, Chang Wook Ahn, and Sangboh Yun. Spatial modulation. *IEEE Transactions on Vehicular Technology*, 57(4):2228–2241, 2008.

[90] Pu Miao, Bingcheng Zhu, Chenhao Qi, Yi Jin, and Chong Lin. A model-driven deep learning method for LED nonlinearity mitigation in OFDM-based optical communications. *IEEE Access*, 7:71436–71446, 2019.

[91] Ioannis Neokosmidis, Thomas Kamalakis, Joachim W. Walewski, Beril Inan, and Thomas Sphicopoulos. Impact of nonlinear LED transfer function on discrete multitone modulation: Analytical approach. *Journal of Lightwave Technology*, 27(22):4970–4978, 2009.

[92] Asanka Nuwanpriya, Jian Zhang, Alex Grant, Siu-Wai Ho, and Lin Luo. Single carrier frequency domain equalization based on on-off-keying for optical wireless communications. In *2013 IEEE Wireless Communications and Networking Conference (WCNC)*, pages 4272–4277, Shanghai, Shanghai, China, April 2013. IEEE.

[93] Hammed G. Olanrewaju, John Thompson, and Wasiu O. Popoola. Generalized spatial pulse position modulation for optical wireless communications. In *2016 IEEE 84th Vehicular Technology Conference (VTC-Fall)*, pages 1–5. IEEE, 2016.

[94] Parth H. Pathak, Xiaotao Feng, Pengfei Hu, and Prasant Mohapatra. Visible light communication, networking, and sensing: A survey, potential and challenges. *IEEE Communications Surveys & Tutorials*, 17(4):2047–2077, 2015.

[95] Linning Peng, Sylvain Haese, and Maryline Hélard. Optimized discrete multitone communication over polymer optical fiber. *Journal of Optical Communications and Networking*, 5(11):1313, 2013.

[96] Wasiu Popoola, Enrique Poves, and Harald Haas. Generalised space shift keying for visible light communications. In *2012 8th International Symposium on Communication Systems, Networks & Digital Signal Processing (CSNDSP)*, pages 1–4. IEEE, 2012.

[97] Wasiu O. Popoola and Harald Haas. Demonstration of the merit and limitation of generalised space shift keying for indoor visible light communications. *Journal of Lightwave Technology*, 32(10):1960–1965, 2014.

[98] Wasiu O. Popoola, Enrique Poves, and Harald Haas. Error performance of generalised space shift keying for indoor visible light communications. *IEEE Transactions on Communications*, 61(5):1968–1976, 2013.

[99] Robin Le Priol, Maryline Hélard, Sylvain Haese, and Sébastien Roy. Experimental comparison of PAM and CAP modulation for visible light communication under illumination constraints. *IEEE Photonics Journal*, 14(2):1–11, 2022.

[100] John G. Proakis and Masoud Salehi. *Digital communications*. McGraw-Hill, Boston, Mass., 5. ed edition, 2008. OCLC: 254796470.

[101] H. Qian, S. J. Yao, S. Z. Cai, and T. Zhou. Adaptive postdistortion for nonlinear LEDs in visible light communications. *IEEE Photonics Journal*, 6(4):1–8, 2014.

[102] D.V. Sarwate and M.B. Pursley. Crosscorrelation properties of pseudorandom and related sequences. *Proceedings of the IEEE*, 68(5):593–619, 1980.

[103] E. Fred Schubert. *Light-Emitting Diodes*. Cambridge University Press, 2 edition, 2006.

[104] Shihe Long, Mohammad-Ali Khalighi, Mike Wolf, Salah Bourennane, and Zabih Ghassemlooy. Channel characterization for indoor visible light communications. In *2014 3rd International Workshop in Optical Wireless Communications (IWOW)*, pages 75–79, Funchal, Madeira, Portugal, 2014. IEEE.

[105] Abrar Siddique, Tahesin Samira Delwar, and Jee-Youl Ryu. A novel optimized V-VLC receiver sensor design using μGA in automotive applications. *Sensors*, 21(23), 2021.

[106] Athanasios Stavridis and Harald Haas. Performance evaluation of space modulation techniques in VLC systems. In *2015 IEEE International Conference on Communication Workshop (ICCW)*, pages 1356–1361. IEEE, 2015.

[107] IEEE Std. 802.11.bb Task Group on Light Communications. IEEE 802.11 Light Communications Amendment. Available: https://www.ieee802.org/11/reports/tgbb_update.htm.

[108] IEEE Std. 802.15.13 WPAN Task Group. Multi-gigabit/s optical wireless communications. Available: https://www.ieee802.org/15/pub/tg13.html.

[109] IEEE Std. 802.15.7-2018 (Revision of IEEE Std. 802.15.7-2011). IEEE standard for local and metropolitan area networks–part 15.7: Short-Range Optical Wireless Communications, 2019.

[110] G. Stepniak, L. Maksymiuk, and J. Siuzdak. Experimental comparison of PAM, CAP, and DMT modulations in phosphorescent white LED transmission link. *IEEE Photonics Journal*, 7(3):1–8, 2015.

[111] Grzegorz Stepniak, Marcin Kowalczyk, and Jerzy Siuzdak. Volterra kernel estimation of white light LEDs in the time domain. *Sensors*, 18(4), 2018.

[112] Grzegorz Stepniak, Lukasz Maksymiuk, and Jerzy Siuzdak. 1.1 Gbit/s white lighting LED-based visible light link with pulse amplitude modulation and Volterra DFE equalization. *Microwave and Optical Technology Letters*, 57(7):1620–1622, 2015.

[113] Grzegorz Stepniak, Manuel Schuppert, and Christian-Alexander Bunge. Advanced Modulation Formats in Phosphorous LED VLC Links and the Impact of Blue Filtering. *Journal of Lightwave Technology*, 33(21):4413–4423, 2015.

[114] Grzegorz Stepniak, Jerzy Siuzdak, and Piotr Zwierko. Compensation of a VLC phosphorescent white LED nonlinearity by means of Volterra DFE. *IEEE Photonics Technology Letters*, 25(16):1597–1600, 2013.

[115] Jiun-Yu Sung, Chi-Wai Chow, and Chien-Hung Yeh. Is blue optical filter necessary in high speed phosphor-based white light LED visible light communications? *Opt. Express*, 22(17):20646–20651, 2014.

[116] Iman Tavakkolnia, Anil Yesilkaya, and Harald Haas. OFDM-based spatial modulation for optical wireless communications. In *2018 IEEE Globecom Workshops (GC Wkshps)*, pages 1–6. IEEE, 2018.

[117] Pham Quang Thai, Nguyen Trung Thanh, Shimamoto Shigeru, Jiang Liu, and Zhong Wende. 127.5 kbps transmission using OLED with 7 kHz 3db modulation bandwidth in visible light communication system. In *2015 International Conference on Advanced Technologies for Communications (ATC)*, pages 389–393. IEEE, 2015.

[118] Murat Uysal, Carlo Capsoni, Zabih Ghassemlooy, Anthony Boucouvalas, and Eszter Udvary, editors. *Optical Wireless Communications: An Emerging Technology*. Signals and Communication Technology. Springer International Publishing, 2016.

[119] Klaas M. vd Zwaag, José L.C. Neves, Helder R.O. Rocha, Marcelo E.V. Segatto, and Jair A.L. Silva. Adaptation to the LEDs flicker requirement in visible light communication systems through CE-OFDM signals. *Optics Communications*, 441:14–20, 2019.

[120] Stefan Videv and Harald Haas. Practical space shift keying VLC system. In *2014 IEEE Wireless Communications and Networking Conference (WCNC)*, pages 405–409. IEEE, 2014.

[121] Jelena Vucic, Christoph Kottke, Stefan Nerreter, Klaus-Dieter Langer, and Joachim W. Walewski. 513 Mbit/s visible light communications link based on DMT-modulation of a white LED. *Journal of Lightwave Technology*, page 5608481, 2010.

[122] Yiguang Wang, Li Tao, Xingxing Huang, Jianyang Shi, and Nan Chi. Enhanced performance of a high-speed WDM CAP64 VLC system employing Volterra series-based nonlinear equalizer. *IEEE Photonics Journal*, 7(3):1–7, 2015.

[123] Khald Werfli, Petr Chvojka, Zabih Ghassemlooy, Navid Bani Hassan, Stanislav Zvanovec, Andrew Burton, Paul Anthony Haigh, and Manav R. Bhatnagar. Experimental Demonstration of High-Speed 4 × 4 Imaging Multi-CAP MIMO Visible Light Communications. *Journal of Lightwave Technology*, 36(10):1944–1951, 2018.

[124] Bernard Widrow and Samuel D. Stearns. *Adaptive Signal Processing*. Prentice-Hall, Inc., 1985.

[125] Mike Wolf, Liane Grobe, Marie Ruth Rieche, Andreas Koher, and Jelena Vucic. Block transmission with linear frequency domain equalization for dispersive optical channels with direct detection. In *2010 12th International Conference on Transparent Optical Networks*, pages 1–8, Munich, Germany, 2010. IEEE.

[126] Fang-Ming Wu, Chun-Ting Lin, Chia-Chien Wei, Cheng-Wei Chen, Zhen-Yu Chen, and Hou-Tzu Huang. 3.22-Gb/s WDM visible light communication of a single RGB LED employing carrier-less amplitude and phase modulation. In *Optical Fiber Communication Conference/National Fiber Optic Engineers Conference 2013*, page OTh1G.4. OSA, 2013.

[127] Fang-Ming Wu, Chun-Ting Lin, Chia-Chien Wei, Cheng-Wei Chen, Hou-Tzu Huang, and Chun-Hung Ho. 1.1-gb/s white-LED-based visible light communication employing carrier-less amplitude and phase modulation. *IEEE Photonics Technology Letters*, 24(19):1730–1732, 2012.

[128] F. Xu, M. Khalighi, and S. Bourennane. Impact of different noise sources on the performance of PIN- and APD-based FSO receivers. In *Proceedings of the 11th International Conference on Telecommunications*, pages 211–218, 2011.

[129] Y. Wang, L. Tao, X. Huang, J. Shi, and N. Chi. 8-gb/s RGBY LED-based WDM VLC system employing high-order CAP modulation and hybrid post equalizer. *IEEE Photonics Journal*, 7(6):1–7, 2015.

[130] Chien-Hung Yeh, Chi-Wai Chow, and Liang-Yu Wei. 1250 Mbit/s OOK wireless white-light VLC transmission based on phosphor laser diode. *IEEE Photonics Journal*, 11(3):1–5, June 2019.

[131] Anil Yesilkaya, Ertugrul Basar, Farshad Miramirkhani, Erdal Panayirci, Murat Uysal, and Harald Haas. Optical MIMO-OFDM with generalized LED index modulation. *IEEE Transactions on Communications*, pages 1–1, 2017.

[132] Anil Yesilkaya, Rui Bian, Iman Tavakkolnia, and Harald Haas. OFDM-based optical spatial modulation. *IEEE Journal of Selected Topics in Signal Processing*, 13(6):1433–1444, 2019.

[133] Yichen Li, Dobroslav Tsonev, and Harald Haas. Non-DC-biased OFDM with optical spatial modulation. In *2013 IEEE 24th Annual International Symposium on Personal, Indoor, and Mobile Radio Communications (PIMRC)*, pages 486–490. IEEE, 2013.

[134] Yiguang Wang, Li Tao, Xingxing Huang, Jianyang Shi, and Nan Chi. 8-Gb/s RGBY LED-based WDM VLC system employing high-order CAP modulation and hybrid post equalizer. *IEEE Photonics Journal*, 7(6):1–7, 2015.

[135] Kai Ying, Zhenhua Yu, Robert J. Baxley, Hua Qian, Gee-Kung Chang, and G. Tong Zhou. Nonlinear distortion mitigation in visible light communications. *IEEE Wireless Communications*, 22(2):36–45, 2015.

[136] Taissir YoussefElganimi. Performance comparison between OOK, PPM and PAM modulation schemes for free space optical (FSO) communication systems: Analytical study. *International Journal of Computer Applications*, 79(11):22–27, 2013.

[137] Fahad Zafar, Masuduzzaman Bakaul, and Rajendran Parthiban. Laser-diode-based visible light communication: Toward gigabit class communication. *IEEE Communications Magazine*, 55(2):144–151, February 2017.

[138] Lubin Zeng, Dominic O'Brien, Hoa Le-Minh, Kyungwoo Lee, Daekwang Jung, and Yunjie Oh. Improvement of data rate by using equalization in an indoor visible light communication system. In *2008 4th IEEE International Conference on Circuits and Systems for Communications*, pages 678–682. IEEE, 2008.

[139] Haiqi Zhang, Aiying Yang, Lihui Feng, and Peng Guo. Gb/s real-time visible light communication system based on white LEDs using T-bridge cascaded pre-equalization circuit. *IEEE Photonics Journal*, 10(2):1–7, 2018.

[140] Long Zhang, Danial Chitnis, Hyunchae Chun, Sujan Rajbhandari, Grahame Faulkner, Dominic O'Brien, and Steve Collins. A comparison of APD- and SPAD-based receivers for visible light communications. *Journal of Lightwave Technology*, 36(12):2435–2442, 2018.

[141] Long Zhang, Hyunchae Chun, Zubair Ahmed, Grahame Faulkner, Dominic O'Brien, and Steve Collins. The future prospects for SiPM-based receivers for visible light communications. *Journal of Lightwave Technology*, 37(17):4367–4374, 2019.

[142] Xiao Zhang, Svilen Dimitrov, Sinan Sinanovic, and Harald Haas. Optimal power allocation in spatial modulation OFDM for visible light communications. In *2012 IEEE 75th Vehicular Technology Conference (VTC Spring)*, pages 1–5. IEEE, 2012.

[143] W. Zhao. *Nonlinearity Modelling and Mitigation for LED Communications*. PhD thesis, University of Wollongong, Wollongong, Australia, 2018.

[144] Yingjun Zhou, Yiran Wei, Fangchen Hu, Jian Hu, Yiheng Zhao, Jianli Zhang, Fengyi Jiang, and Nan Chi. Comparison of nonlinear equalizers for high-speed visible light communication utilizing silicon substrate phosphorescent white LED. *Opt. Express*, 28(2):2302–2316, 2020.

INSA de RENNES
Service des Formations

AVIS DU JURY SUR LA REPRODUCTION DE LA THESE SOUTENUE

Titre de la thèse:
Améliorations des Transmissions VLC (Visible Light Communication) Sous Contrainte D'Éclairage: Études Théoriques et Expérimentations

Nom Prénom de l'auteur : LE PRIOL ROBIN

Membres du jury :
- Monsieur KHALIGHI Mohammad-Ali
- Madame AUPETIT BERTHELEMOT Christelle
- Madame HELARD Maryline
- Monsieur PLOURDE Eric
- Monsieur HRANILOVIC Steve
- Monsieur LE RUYET Didier
- Monsieur ROY Sébastien
- Monsieur HAESE Sylvain

Président du jury : Didier LE RUYET

Date de la soutenance : 14 Juin 2022

Reproduction de la these soutenue

☒ Thèse pouvant être reproduite en l'état
☐ Thèse pouvant être reproduite après corrections suggérées

Fait à Rennes, le 14 Juin 2022

Signature du président de jury

D. Le Ruyet

Le Directeur,

Vincent BRUNIE

Titre : Améliorations des Transmissions VLC (Visible Light Communication) Sous Contrainte d'Éclairage: Études Théoriques et Expérimentations

Mots clés : communications en lumière visible, éclairage intérieur, non-linéarités de la LED, modulation d'amplitude et de phase sans porteuse, MIMO, décomposition de matrice polynomiale

Résumé : Les réseaux de communication en lumière visible (VLC) s'appuyant sur l'utilisation de diodes électroluminescentes (LED) bénéficient actuellement d'un intérêt grandissant, en partie grâce à leur robustesse face aux interférences électromagnétiques, leur large bande disponible non-régulée, leur faible coût, leur bonne efficacité énergétique, ainsi que leur compatibilité avec les infrastructures d'éclairage déjà existantes. Dans cette thèse, nous étudions des techniques de modulation à haute efficacité spectrale pour la couche physique des VLC pour augmenter les débits tout en considérant la qualité de l'éclairage ainsi que les coûts d'implémentation. Des études numériques et expérimentales sont réalisées sur la modulation d'impulsion d'amplitude (PAM) et sur la modulation d'amplitude et de phase sans porteuse (CAP) sous des contraintes d'éclairage et pour des grands ordres de modulation. De plus, l'impact des non-linéarités de la LED est étudié et une technique de post-distorsion est évaluée pour corriger ces effets non-linéaires. Dans ce cadre, des débits de plusieurs centaines de Mb/s sont atteints en utilisant un banc de test réalisé à partir de composants à bas coûts. Par ailleurs, un système multi-entrées multi-sorties (MIMO) imageant est également développé et l'impact du désalignement de l'imageur sur les performances est étudié. Finalement, une technique de décomposition polynomiale basée sur la méthode de factorisation classique LU est étudiée et appliquée aux systèmes MIMO VLC dans des grands espaces intérieurs.

Title : Improvements of VLC (Visible Light Communication) Transmissions Under Illumination Constraints: Theoretical Studies and Experiments

Keywords : visible light communication, indoor illumination, LED nonlinearity, carrierless amplitude and phase modulation, MIMO, polynomial matrix decomposition

Abstract : Indoor visible light communication (VLC) networks based on light-emitting diodes (LEDs) currently enjoy growing interest thanks in part to their robustness against interference, wide license-free available bandwidth, low cost, good energy efficiency and compatibility with existing lighting infrastructure. In this thesis, we investigate spectral-efficient modulation techniques for the physical layer of VLC to increase throughput while considering the quality of illumination as well as implementation costs. Numerical and experimental studies are performed employing pulse amplitude modulation (PAM) and carrierless amplitude and phase (CAP) modulation under illumination constraints and for high modulation orders. Furthermore, the impact of LED nonlinearity is investigated and a postdistortion technique is evaluated to compensate these nonlinear effects. Within this framework, transmission rates in the order of a few hundred Mb/s are achieved using a test bench made of low-cost components. In addition, an imaging multiple-input multiple-output (MIMO) system is developed and the impact on performance of imaging lens misalignment is theoretically and numerically assessed. Finally, a polynomial matrix decomposition technique based on the classical LU factorization method is studied and applied for the first time to MIMO VLC systems in large space indoor environments.